DISSERTATION

HIGHER ORDER VOLUME/SURFACE INTEGRAL EQUATION MODELING OF ANTENNAS AND SCATTERERS USING DIAKOPTICS AND METHOD OF MOMENTS

Submitted by

Elene Chobanyan

Department of Electrical and Computer Engineering

In partial fulfilment of the requirements

For the Degree of Doctor of Philosophy

Colorado State University

Fort Collins, Colorado

Spring 2015

Doctoral Committee:

Advisor: Branislav Notaros

Steven Reising
Iuliana Oprea
V. Chandrasekar
Ali Pezeshki

ABSTRACT

HIGHER ORDER VOLUME/SURFACE INTEGRAL EQUATION MODELING OF ANTENNAS AND SCATTERERS USING DIAKOPTICS AND METHOD OF MOMENTS

The principal objective of this dissertation is to develop, test, and optimize accurate, efficient, and robust computational methodology and tools for modeling of general antennas and scatterers based on solutions of electromagnetic integral equation formulations using the method of moments (MoM) and diakoptics. The approaches and implementations include the volume integral equation (VIE) method and its hybridization with the surface integral equation (SIE) method, in two ways. The first way combines the VIE method for dielectric parts and the SIE method for metallic parts of the structure. The second way performs subdivision of the entire structure into SIE domains of different constant permittivities, while modeling the inhomogeneity within each domain by the VIE method and employing different Green's functions, with describing the inhomogeneity within each domain in terms of a perturbation with respect to the background permittivity. The first approach is very suitable for analysis of composite wire-plate-dielectric radiation/scattering structures. The second approach provides a particularly efficient solution to problems involving inhomogineities embedded within high-contrast homogeneous dielectric scatterers. The efficiency of computation is enhanced by applying the diakoptic domain decomposition. In the VIE-SIE diakoptic method, the interior diakoptic subsystems containing inhomogeneous dielectric materials are analyzed completely independently applying the VIE-SIE MoM solver, and the solution to the original problem is obtained from linear relations between electric and magnetic surface-current diakoptic

coefficients on diakoptic surfaces, written in the form of matrices. The techniques implement Lagrange-type generalized curved parametric hexahedral MoM-VIE volume elements and quadrilateral MoM-SIE and diakoptic patches of arbitrary geometrical-mapping orders, and divergence-conforming hierarchical polynomial vector basis functions of arbitrary current expansion orders. The hexahedra can be filled with inhomogeneous dielectric materials with continuous spatial variations of the permittivity described by Lagrange interpolation polynomials of arbitrary material-representation orders. Numerical computation is further accelerated by MPI parallelization to enable analysis of large electromagnetic problems.

ACKNOWLEDGMENTS

To begin I would like to thank my advisor Dr. Branislav Notaroš for his guidance, help and motivation, which has made me a better researcher and this dissertation possible. I would also like to thank my colleagues Sanja Manić, Ana Manić and Nada Šekeljić for a supportive and collaborative environment, which allowed my research to be more productive and enjoyable. Many thanks to my family Alexander Chobanyan, Levon Chobanyan, Sergej Chobanyan and Marine Ter-Grigoryan, extraordinary and incredibly thoughtful people, whose help, advice and love lead me through all my academic endeavors. Also, thank you to my wonderful husband, Jorgen Rasmussen, who filled my life with the love and care, which helped me to persevere during most trying days of my PhD studies.

This work at Colorado State University was supported by the National Science Foundation under grants ECCS-1002385 and AGS-1344862.

TABLE OF CONTENTS

1 VOLUME/SURFACE INTEGRAL EQUATION FOR SCATTERING AND RADIATION PROBLEMS[1]

1.1 Introduction

The method of moments (MoM) for discretizing integral equations in electromagnetics is an extremely powerful and versatile general numerical methodology for electromagnetic-field simulation in antenna and scattering applications [1]–[5]. For antennas and scatterers composed of metallic and homogeneous linear dielectric parts, the MoM is most frequently applied in conjunction with the surface integral equation (SIE) approach [2], [6], [7], where both electric and magnetic equivalent (artificial) surface currents are introduced over boundary surfaces between homogeneous regions of the structure, and surface integral equations based on boundary conditions for both electric and magnetic field intensity vectors are solved with current densities as unknowns. On the metallic surfaces, only the surface electric current exists (this is actual current) and is treated as an unknown quantity. An alternative approach to MoM analysis of dielectric scatterers is the volume integral equation (VIE) approach [8]–[11], where, employing the volume equivalence principle, a structure containing linear dielectric materials of arbitrary inhomogeneity and complexity is represented by a distribution of volume electric (polarization and conduction) current (the real current) radiating in free space, and the resulting VIE, with the total volume current density vector, or another vector proportional to it (e.g., the total electric field vector), as unknown quantity, is discretized by the MoM. The analysis of composite dielectric and metallic radiation/scattering structures can be performed combining the VIE for

dielectric parts and the SIE for metallic parts, giving rise to a hybrid VIE-SIE or VSIE formulation, which solves simultaneously for the volume current throughout the dielectric domains and the surface current over the metallic surfaces of the composite structure [12]–[14],.

However, practically all the existing three-dimensional (3-D) MoM-VIE and MoM-VSIE simulation tools for dielectric/metallic structures are low-order or small-domain (subdomain) techniques – the structure is modeled by volume (and surface) geometrical elements that are electrically very small and the volume (and surface) electric currents within the elements are approximated by low-order (zeroth-order and first-order) basis functions. More precisely, the elements (cells and patches) are on the order of $\lambda/10$ in each dimension, λ being the wavelength in the medium. This results in a very large number of unknowns (unknown current-distribution coefficients) needed to obtain results of satisfactory accuracy, with all the associated problems and enormous requirements in computational resources. In addition, commonly used 3-D VIE elements are in the form of cubes, bricks (parallelepipeds), and tetrahedra, all with planar sides, and thus they do not provide enough flexibility and efficiency in modeling of structures with pronounced curvature.

An alternative which can greatly reduce the number of unknowns for a given problem and enhance further the accuracy and efficiency of the MoM-VIE analysis in antenna/scattering applications is the higher order or large-domain (entire-domain) computational approach [15]. According to this approach, a structure is approximated by a number of as large as possible geometrical elements, and the approximation of current (or field) components within individual elements is in the form of a single (three-fold) functional series of sufficiently high order. Only relatively recently the computational electromagnetics (CEM) community has started to extensively investigate and employ higher order surface and volume elements and higher order

basis functions in the frame of MoM, including the SIE formulation [16], [17], VIE approach[20]–[27], and VSIE hybrid[30]–[36], as well as the finite element method (FEM) [37] –[41].

For MoM-VIE modeling of general structures that may possess arbitrary curvature, it is essential to have both higher order geometrical flexibility and higher order current-approximation flexibility in the same method. In other words, if higher order basis functions for currents (or fields) are used on volume elements with flat sides, many small elements may be required for the geometrical precision of the model, and then higher order basis functions actually reduce to low-order functions (on small elements). On the other hand, geometrical flexibility of curved elements can be fully exploited only if they can be made electrically large, which implies the use of higher order current expansions within the elements as well. Finally, in order to make the modeling of realistic structures optimal, it is often convenient to have elements of different orders and sizes combined together in the same model. If all of these requirements are to be satisfied, implementation of hierarchical-type higher order polynomial basis functions for the approximation of the volume electric current within curved elements seems to be the right choice.

This thesis proposes a novel higher order and large-domain Galerkin-type MoM-VIE technique for 3-D analysis of radiation/scattering structures based on higher order geometrical modeling and higher order current modeling, which we refer to as a double-higher-order VIE method. The volume elements proposed for the approximation of geometry are Lagrange-type interpolation generalized hexahedra of arbitrary geometrical-mapping orders. The basis functions proposed for the approximation of currents within the elements are hierarchical divergence-conforming 3-D polynomial vector basis functions of arbitrary expansion orders.

The proposed technique represents a generalization of the MoM-VIE technique [19], where trilinear hexahedra (volume elements of the first geometrical order) are used with higher order polynomial current expansions. It also represents a VIE version of the double-higher-order SIE method [17], on one side, and a MoM version of the double-higher-order FEM [40], on the other side. In fact, this is a double-higher-order VIE-SIE or VSIE method, as it includes the corresponding SIE discretization of metallic surfaces, and in that sense may be considered a generalization of the MoM-VSIE technique [30], which uses volume and surface elements of the first geometrical order in conjunction with polynomial large-domain volume and surface current approximations.

The new method enables excellent curvature modeling and excellent current-distribution modeling, which, in turn, enable using large curved VIE hexahedra that are on the order of λ in each dimension as building blocks for modeling of the dielectric object (i.e., the volume elements can be by an order of magnitude larger in each direction than traditional low-order elements). In specific, the model can include as large as about $2\lambda \times 2\lambda \times 2\lambda$ VIE generalized hexahedra (which is 8,000 times larger in volume than conventional low-order volume modeling discretization limit of $\lambda/10 \times \lambda/10 \times \lambda/10$) with curvature modeling using high (e.g., fourth) geometrical-mapping orders and *p*-refined current distributions of high (e.g., sixth) orders of basis functions. Element orders in the model, however, can also be low, so that the lower order modeling approach is actually included in the higher order modeling. The geometrical orders and current-approximation orders of the VIE elements are entirely independent from each other, and the two sets of parameters of the double-higher-order model can be combined independently for the best overall performance of the method. Additionally, because the implemented basis functions are hierarchical, a whole spectrum of element sizes (e.g., from a very small fraction of

λ to 2λ), geometrical orders (e.g., from 1 to 4), and current-approximation orders (e.g., from 1 to 6) can be used at the same time in a single simulation model of a complex structure, making this method essentially a combined, low-to-high, order method. Finally, each individual element can have drastically different edge lengths, with or without curvature, enabling a whole range of generalized-hexahedral element shapes (e.g., brick-like, slab-like, and rod-like planar hexahedra, as well as spherically-shaped, cylindrically-shaped, and elliptically-shaped curved hexahedra, and also other "irregular" and/or curved hexahedral shapes) to be used in a simulation model as well.

The results obtained by the double-higher-order VIE (VSIE) technique are validated against the analytical solutions in the form of Mie's series and the numerical results obtained by the double-higher-order SIE and FEM-MoM (FEM-SIE) techniques [17] and [40], respectively, as well as the solutions using one of the industry's leading commercial software tools for full wave electromagnetic analysis – WIPL-D, which is a higher order SIE code [2]. Numerical examples show that the proposed double-higher-order VIE and VSIE modeling does not only provide an accurate solution and useful alternative to other, more frequently used, types of CEM techniques but in many cases provides either on par or a more efficient solution. Most importantly, note that all numerical comparisons and evaluations in the thesis are performed with respect to highly efficient and accurate techniques implementing similar types of higher order numerical discretization applied to different equations; the advantages of the proposed VIE/VSIE modeling are much more pronounced if compared to conventional approaches using low-order and small-domain volume and surface discretizations.

1.2 Two-Potential Volume Integral Equation Formulation for the Equivalent Displacement Vector

Consider an electromagnetic structure consisting of arbitrarily shaped dielectric and metallic parts, situated in free space. Let the relative permittivity, ε_r, and conductivity, σ, of the dielectric material be known functions of position, while the permeability at all points is μ_0. In addition, let the structure be excited by a time-harmonic electromagnetic field of complex electric field intensity vector $\mathbf{E}_i$ and angular frequency ω. This field may be a combination of incident plane waves (for a scattering structure) or the impressed field of one or more lumped generators (for an antenna structure). It induces volume electric (polarization and conduction) current, of density **J**, to flow throughout the volume of the structure. This current and the associated charge are, in turn, the sources of the scattered electric field, of intensity vector $\mathbf{E}_s$. From the constitutive equation for the current (generalized local Ohm's law), **J** is related to the total (incident/impressed plus scattered) electric field intensity at any point in the material as [33]

$$\mathbf{J} = \mathrm{j}\omega(\varepsilon_e - \varepsilon_0)(\mathbf{E}_i + \mathbf{E}_s), \quad \varepsilon_e = \varepsilon - \mathrm{j}\frac{\sigma}{\omega}, \tag{1}$$

with ε_e being the equivalent complex permittivity of the material at that point. The scattered field can be computed as if the sources were radiating in free space (volume equivalence principle), using magnetic vector and electric scalar Lorenz potentials,

$$\mathbf{E}_s = -\mathrm{j}\omega\mathbf{A} - \nabla\Phi, \tag{2}$$

$$\mathbf{A} = \mu_0 \int_V \mathbf{J} g \, \mathrm{d}V, \tag{3}$$

$$\Phi = \frac{\mathrm{j}}{\omega\varepsilon_0}\left[\int_V \nabla\cdot\mathbf{J}g\mathrm{d}V + \int_{S_\mathrm{d}} \mathbf{n}\cdot(\mathbf{J}_1-\mathbf{J}_2)g\mathrm{d}S\right]. \qquad (4)$$

Here, V is the domain with volume current and charge, S_d are surfaces of discontinuity in ε_e (where surface charge may accumulate), with the unit normal vector, **n**, directed from medium 2 into medium 1, and g is the free-space Green's function,

$$g = \frac{e^{-\mathrm{j}\beta_0 R}}{4\pi R}\ , \qquad \beta_0 = \omega\sqrt{\varepsilon_0\mu_0}\ , \qquad (5)$$

β_0 being the free-space phase coefficient (wave number) and R the distance of the field point from the source point. Having in mind the integral expression for the field $\mathbf{E}_\mathrm{s}$ in (2)-(5), (1) represents a volume integral equation, with **J** as unknown quantity.

However, if divergence-conforming bases are used in the VIE model, **J** in (1) is expressed in terms of the equivalent electric displacement vector, $\mathbf{D} = \varepsilon_\mathrm{e}\mathbf{E}$, whose normal component is continuous ($\mathbf{n}\cdot\mathbf{D}_1 = \mathbf{n}\cdot\mathbf{D}_2$) across the surfaces S_d. The relationship between the two vectors is

$$\mathbf{J} = \mathrm{j}\omega C\mathbf{D}, \qquad C = \frac{\varepsilon_\mathrm{e}-\varepsilon_0}{\varepsilon_\mathrm{e}}, \qquad (6)$$

where C stands for the electric contrast of the dielectric with respect to free space (background medium). With this, (1) and (2) give the following two-potential VIE with **D** as unknown:

$$\frac{\mathbf{D}}{\varepsilon_\mathrm{e}} + \mathrm{j}\omega\mathbf{A} + \nabla\Phi = \mathbf{E}_\mathrm{i}, \qquad (7)$$

which, of course, includes the potential expressions in (3)-(5). Note that the unknown here is, in fact, the equivalent displacement current density, $\mathbf{J}_\mathrm{d} = \mathrm{j}\omega\mathbf{D}$, in place of the equivalent conduction current density, **J**, in (1).

On metallic surfaces – that may have distributed loadings, e.g., surfaces with resistive or dielectric thin layers (coatings), conductors with skin effect taken into account, etc. – the volume current density **J** degenerates into the surface current density, $\mathbf{J}_s$, and the VIE (7) into a SIE given by [17]

$$Z_S \mathbf{J}_S + j\omega \mathbf{A}_{tang} + (\nabla \Phi)_{tang} = (\mathbf{E}_i)_{tang}, \qquad (8)$$

where Z_S is the appropriate surface impedance. For bare surfaces made of a perfect electric conductor (PEC), $Z_S = 0$, and the tangential component of the total electric field on the surface is zero. In analysis of structures composed of both dielectric and metallic parts, (7) and (8) constitute a hybrid VIE-SIE or VSIE system of integral equations, which are coupled together because potentials **A** and Φ at any point of the structure are functions of both **D** and $\mathbf{J}_S$. We discretize and solve the VSIE system simultaneously for **D** and $\mathbf{J}_S$ using the method of moments.

1.3 Higher Order 3-D Geometrical Modeling and Higher Order Basis Functions for Volume Current Modeling

As basic building blocks for geometrical modeling in 3-D VIE computations, we propose Lagrange-type generalized curved parametric hexahedral volume elements of arbitrary geometrical orders K_u, K_v, and K_w (K_u, K_v, $K_w \geq 1$), determined by $M = (K_u + 1)(K_v + 1)(K_w + 1)$ points (interpolation nodes) arbitrarily positioned in space and analytically described as [40]

$$\mathbf{r}(u,v,w) = \sum_{i=0}^{K_u} \sum_{j=0}^{K_v} \sum_{k=0}^{K_w} \mathbf{r}'_{ijk} L_i^{K_u}(u) L_j^{K_v}(v) L_k^{K_w}(w) = \sum_{i=0}^{K_u} \sum_{j=0}^{K_v} \sum_{k=0}^{K_w} \mathbf{r}_{ijk} u^i v^j w^k \quad ,$$

$$L_i^{K_u}(u) = \prod_{\substack{l=0 \\ l \neq i}}^{K_u} \frac{u - u_l}{u_i - u_l}, \qquad -1 \le u, v, w \le 1, \tag{9}$$

where $\mathbf{r}'_{ijk} = \mathbf{r}(u_i, v_j, w_k)$ are position vectors of interpolation nodes, $L_i^{K_u}$ represent Lagrange interpolation polynomials in the u coordinate, with the nodes defined as $u_l = (2l - K_u)/K_u$, $l = 0,1,...,K_u$, and similarly for $L_j^{K_v}(v)$ and $L_k^{K_w}(w)$, and $\mathbf{r}_{ijk}$ are constant vector coefficients related to $\mathbf{r}'_{ijk}$. Note that the orders K_u, K_v, and K_w can be adopted anisotropically (i.e., they do not need to be the same) within an element. Equation (9) defines a mapping from a cubical parent domain to the generalized hexahedron, as illustrated in Fig. 1.

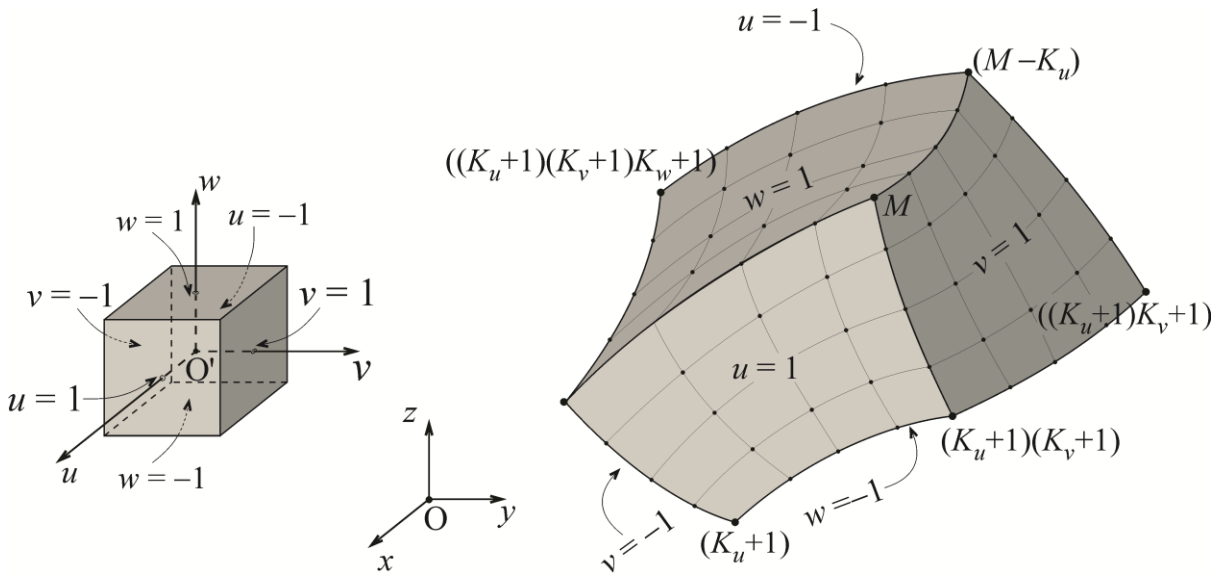

Fig. 1. Generalized curved parametric hexahedral VIE element of geometrical orders K_u, K_v, and K_w ($K_u, K_v, K_w \ge 1$), determined by $M = (K_u + 1)(K_v + 1)(K_w + 1)$ interpolation nodes arbitrarily positioned in space; cubical parent domain is also shown.

Geometrically higher order elements obviously allow better flexibility and accuracy in modeling of complex curved structures. As a simple example, Fig. 2(a) and Fig. 2(b) show a sphere modeled by 1000 trilinear hexahedra ($K_u = K_v = K_w = 1$) and a single triquadratic hexahedron ($K_u = K_v = K_w = 2$), respectively. In this paper, we use the equidistant distribution of interpolation nodes along each coordinate in the 3-D parametric space, while the use of specific non-equidistant node distributions, which would provide additional modeling flexibility and accuracy in some VIE applications, is possible as well. In addition, any other choice of higher order volume expansions for geometrical modeling that can be represented as a triple sum of 3-D power functions $u^i v^j w^k$ (e.g., parametric hexahedra using spline functions for describing the geometry) can also readily be implemented in our VIE method.

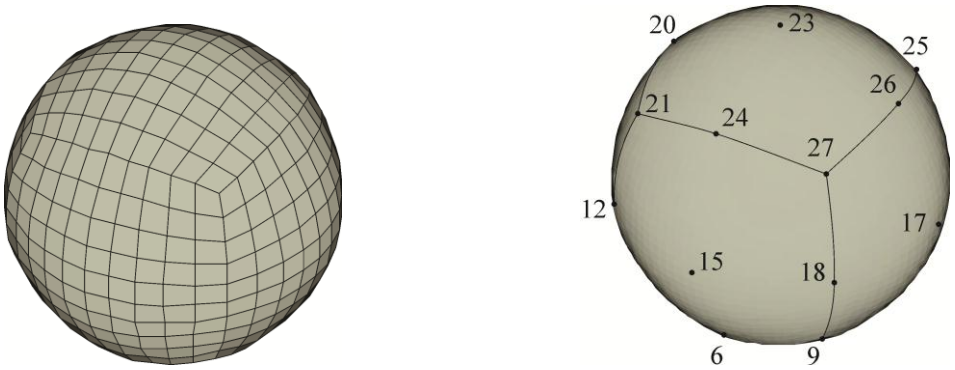

(a) (b)

Fig. 2. A sphere modeled by (a) 1000 trilinear hexahedra [$K_u = K_v = K_w = 1$ in (9)] and (b) a single triquadratic hexahedron [$K_u = K_v = K_w = 2$ in (9)].

We represent the displacement vector inside every generalized hexahedron (Fig. 1) in the model as [33]

$$\mathbf{D} = \sum_{p=0}^{N_u} \sum_{s=0}^{N_v-1} \sum_{t=0}^{N_w-1} \alpha_{upst}\,\mathbf{f}_{upst} + \sum_{p=0}^{N_u-1} \sum_{s=0}^{N_v} \sum_{t=0}^{N_w-1} \alpha_{vpst}\,\mathbf{f}_{vpst} + \sum_{p=0}^{N_u-1} \sum_{s=0}^{N_v-1} \sum_{t=0}^{N_w} \alpha_{wpst}\,\mathbf{f}_{wpst}, \tag{10}$$

where **f** are divergence-conforming hierarchical-type vector basis functions defined by

$$\mathbf{f}_{upst} = \frac{Q_p(u)\,v^s w^t}{\mathfrak{I}}\,\mathbf{a}_u$$
$$\mathbf{f}_{vpst} = \frac{u^p Q_s(v) w^t}{\mathfrak{I}}\,\mathbf{a}_v, \quad Q_p(u) = \begin{cases} 1-u, & p=0 \\ u+1, & p=1 \\ u^p - 1, & p \geq 2, \text{even} \\ u^p - u, & p \geq 3, \text{odd} \end{cases} \quad -1 \leq u, v, w \leq 1, \tag{11}$$
$$\mathbf{f}_{wpst} = \frac{u^p v^s Q_t(w)}{\mathfrak{I}}\,\mathbf{a}_w$$

N_u, N_v, and N_w are the adopted orders of the polynomial current approximation in the *u*-, *v*-, and *w*-direction, respectively, which are entirely independent from the element geometrical orders (K_u, K_v, and K_w), $\{\alpha\}$ are unknown current-distribution coefficients, and $\mathfrak{I}$ is the Jacobian of the covariant transformation, found from unitary vectors $\mathbf{a}_u$, $\mathbf{a}_v$ and $\mathbf{a}_w$ along the parametric coordinates,

$$\mathfrak{I} = (\mathbf{a}_u \times \mathbf{a}_v) \cdot \mathbf{a}_w, \quad \mathbf{a}_u = \frac{\partial \mathbf{r}}{\partial u}, \quad \mathbf{a}_v = \frac{\partial \mathbf{r}}{\partial v}, \quad \mathbf{a}_w = \frac{\partial \mathbf{r}}{\partial w}, \tag{12}$$

with **r** given in (9). Basis functions defined in (11) are hierarchical functions (each lower-order set of functions is a subset of all higher-order sets).

Note that the lowest order of approximation ($N_u = N_v = N_w = 1$) in (10)-(12) yields the 3-D rooftop functions on generalized hexahedral cells (which, for such basis functions, then must be very small). For any s and t ($0 \leq s \leq N_v - 1$, $0 \leq t \leq N_w - 1$), the basis functions $(1-u)v^s w^t$ (for $p = 0$) and $(u+1)v^s w^t$ (for $p = 1$) serve for adjusting the continuity boundary condition for the normal component of the vector **D** over sides $u = -1$ and $u = 1$, respectively, of the element

(divergence conformity), while the remaining basis functions (for $2 \le p \le N_u$) are zero at the hexahedron sides and serve for improving the current approximation throughout the volume. From (10)-(12), this vector component for the side $u = -1$, for instance, is

$$(D_u)_{\text{norm}} = D_u \sin\theta_{u(v,w)} = D_u(-1,v,w)\frac{(\mathbf{a}_v \times \mathbf{a}_w)\cdot \mathbf{a}_u}{|\mathbf{a}_v \times \mathbf{a}_w \| \mathbf{a}_u|}$$

$$= \frac{2}{|\mathbf{a}_v(-1,v,w)\times \mathbf{a}_w(-1,v,w)|}\sum_{s=0}^{N_v-1}\sum_{t=0}^{N_w-1}\alpha_{u0st}v^s w^t, \qquad (13)$$

where D_u denotes the u-component of **D** at the side (the v- and w-components of **D** are tangential to the side), and $\theta_u(v,w)$ the angle between the u parametric line and vw parametric surface at the same point. Since the respective unitary vectors tangential to the side, $\mathbf{a}_v(-1,v,w)$ and $\mathbf{a}_w(-1,v,w)$, are the same for the two adjacent elements sharing the side, the continuity condition between the elements, for $-1 \le v,w \le 1$, can readily (automatically) be enforced, regardless of the adopted geometrical orders, current-expansion orders, or local orientations of the elements. The only requirement that needs to be satisfied is the geometrical compatibility of the joint face. Shown in Fig. 3 is an example of an element ($e1$) of the first geometrical order in all directions ($K_u^{e_1} = K_v^{e_1} = K_w^{e_1} = 1,\ M^{e_1} = 8$) and an element ($e2$) of the second geometrical order in all directions ($K_u^{e_1} = K_v^{e_1} = K_w^{e_1} = 2,\ M^{e_2} = 27$) that are adjacent in the mesh and share a common face. Moreover, the two elements have different current-approximation orders in all respective dimensions ($N_u^{e_1} = 1,\ N_v^{e_1} = 2,\ N_w^{e_1} = 2$ and $N_u^{e_2} = 7,\ N_v^{e_2} = 5,\ N_w^{e_2} = 3$). In our assembly procedure, the geometrical interpolation nodes associated with the two elements that govern the geometry of the common face are ordered in a way that ensures a symmetrical or anti-symmetrical variation of the corresponding parametric coordinates, i.e.,

$\{u, v, \text{or } w\}^{e_1} = \pm\{u, v, \text{or } w\}^{e_2}$ (for the example in Fig. 3, $u^{e_1} = -v^{e_2}$ and $w^{e_1} = -w^{e_2}$). The continuity of the normal displacement vector component across the common face is imposed by equating the corresponding normal-vector coefficients, α_{u0st} in (13), associated with *e*1 and *e*2, so that these coefficients are common for the two elements, with additional corrections (sign change) due to possibly different element orientations. The procedure has to be repeated for all faces shared by pairs of elements in the mesh. For elements with different geometrical orders, the same (or almost the same) parametric presentations on both sides of the common face are ensured by placing the interpolation nodes of the element with a higher order at positions that match the parameter values already determined by the interpolation nodes of the element with a lower order. For elements with different current-expansion orders, the normal-vector coefficients are matched only up to the lesser of the corresponding orders and are set to zero for the remaining normal-vector basis functions.

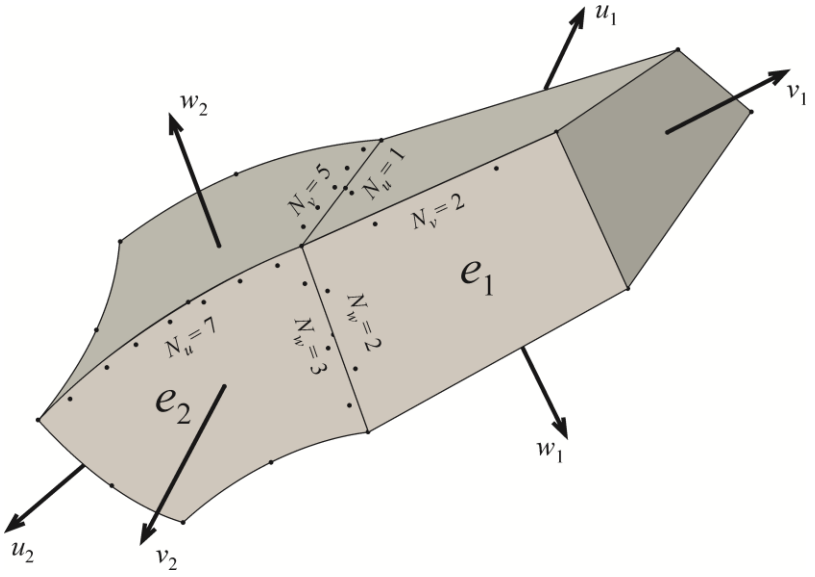

Fig. 3. A connection of two generalized hexahedral elements with different geometrical orders, current-approximation orders, and orientations.

This order reduction pertains to the common face only and does not influence the expansions throughout the rest of the volumes of the higher order elements. In VIE modeling, the use of bases automatically (for any numerical solution) satisfying the continuity of the normal component of **D** at joints of elements in the model actually ensures that theoretically nonexistent surface charges at a boundary between elements across which the properties of the dielectric are continuous functions cannot be obtained as a consequence of inaccurate numerical solution of a problem. However, since the vector **D** in air is not modeled, the boundary condition for $\mathbf{D}_{\text{norm}}$ on the interface dielectric/air is not enforced automatically but numerically, taking into account the surface charge on the interface.

Note also that the sum limits in (10) that correspond to the variations of a displacement vector component in the directions across that component are by one smaller than the order corresponding to the variation in the other parametric coordinate. This mixed-order arrangement, which ensures equal approximation orders for volume charge densities corresponding to the *u*-, *v*-, and *w*-directed current basis functions, has been found to be a preferable choice for modeling of volume currents in all applications. It enables considerable reductions in the overall number of unknowns, at no expense in terms of the accuracy of current and charge modeling throughout the elements. Note finally that similar higher order basis functions in the curl-conforming form are used in the FEM analysis [40], as well as that the 2-D (surface) version of the bases is employed in the SIE solution [17].

Finally, what is extremely important, in our VSIE technique for analysis of composite metallic and dielectric radiation/scattering structures, generalized curvilinear quadrilateral elements with 2-D higher order basis functions for SIE modeling of the surface current density $\mathbf{J}_s$ over metallic surfaces are formally treated as degenerate generalized hexahedral elements, in

Fig. 1, having the w-dimension suppressed, with the displacement vector **D**, in (10), or the displacement current density, having only *u*- and *v*-components, with the *w*-component suppressed. In addition, thin metallic wires are formally treated as double-degenerate hexahedra with only the *u*-component of the vector **D** standing for the line current intensity, *I*, along the generatrices of wires (the reduced-kernel approximation for wires) [23]. This approach is formally implemented in all interactions of volume and surface elements (and wires) and the associated testing and basis functions, to dramatically reduce the number of possible combinations in treatments of elements of different nature in topological analysis of the structure in preprocessing, filling the MoM matrix through multiple levels of integration and packing the MoM generalized impedances and voltages, and field computations in postprocessing.

1.4 Generalized Galerkin Impedances and Potential Integrals for Double-Higher-Order Hexahedral VIE Elements

In order to determine the unknown coefficients $\{\alpha\}$ in (10), the VSIE system in (7) and (8) is tested by means of the Galerkin method, i.e., using the same functions used for current expansion. The VIE-VIE type of generalized Galerkin impedances (the system matrix elements) corresponding to the volume-current testing and basis functions $\mathbf{f}_m$ and $\mathbf{f}_n$ defined on the *m*th and *n*th generalized hexahedral volume elements (V_m and V_n), respectively, in the model are given by [21], [33]

$$Z_{mn}^{\mathrm{vv}} = \int_{V_m} \frac{1}{\varepsilon_{en}} \mathbf{f}_m \cdot \mathbf{f}_n \mathrm{d}V_m + \mathrm{j}\omega \int_{V_m} \mathbf{f}_m \cdot \mathbf{A}_n \mathrm{d}V_m - \int_{V_m} \nabla \cdot \mathbf{f}_m \Phi_n \mathrm{d}V_m + \int_{S_m} \Phi_n \mathbf{f}_m \cdot \mathrm{d}\mathbf{S}_m, \quad (14)$$

where $\mathbf{A}_n$ and Φ_n are potentials due to the basis function $\mathbf{f}_n$ and the last two integral terms are obtained expanding $\nabla\cdot(\mathbf{f}_m\Phi_n)$ and applying the divergence theorem, with Sm being the surface of the mth element, oriented outward. Similar expressions hold for VIE-SIE, SIE-VIE, and SIE-SIE generalized Galerkin impedances. To illustrate the procedure for computing these impedances, we consider, without the loss of generality, only the *u*-components of basis and testing functions. Furthermore, we consider the functions in the following simplified form:

$$\mathbf{f}=\mathbf{f}_{upst}=\frac{u^p v^s w^t}{\mathfrak{I}}\frac{\partial\mathbf{r}}{\partial u}\qquad [Q_p(u)=u^p]. \tag{15}$$

The generalized Galerkin impedances corresponding to the complete, divergence-conforming, basis functions in (11) can be obtained as a linear combination of those corresponding to the simplified, three-dimensional power functions in (15).

Upon substituting (15) and (9), the second integral term in (14) corresponding to the testing function defined by indices p_m, s_m, and t_m on the *m*th hexahedron and the basis function defined by indices p_n, s_n, and t_n on the *n*th hexahedron in the model becomes

$$\begin{aligned}
&\mathrm{j}\omega\int_{V_m}\mathbf{f}_m\cdot\mathbf{A}_n\mathrm{d}V_m=-\omega^2\mu_0 C_n\int_{-1}^{1}\int_{-1}^{1}\int_{-1}^{1}\int_{-1}^{1}\int_{-1}^{1}\int_{-1}^{1}\mathbf{f}_m(p_m,s_m,t_m)\cdot\mathbf{f}_n(p_n,s_n,t_n)\\
&\times g(R)\mathfrak{I}_n\mathfrak{I}_m\mathrm{d}u_n\mathrm{d}v_n\mathrm{d}w_n\mathrm{d}u_m\mathrm{d}v_m\mathrm{d}w_m\\
&\quad=-\omega^2\mu_0 C_n\sum_{i_m=1}^{K_u^{(m)}}\sum_{j_m=0}^{K_v^{(m)}}\sum_{k_m=0}^{K_w^{(m)}}\sum_{i_n=1}^{K_u^{(n)}}\sum_{j_n=0}^{K_v^{(n)}}\sum_{k_n=0}^{K_w^{(n)}} i_m i_n(\mathbf{r}^{(m)}_{i_m j_m k_m}\cdot\mathbf{r}^{(n)}_{i_n j_n k_n})\\
&\times\int_{-1}^{1}\int_{-1}^{1}\int_{-1}^{1}\int_{-1}^{1}\int_{-1}^{1}\int_{-1}^{1} u_m^{p_m+i_m-1}v_m^{s_m+j_m}w_m^{t_m+k_m}u_n^{p_n+i_n-1}v_n^{s_n+j_n}w_n^{t_n+k_n}g(R)\times\mathrm{d}u_n\mathrm{d}v_n\mathrm{d}w_n\mathrm{d}u_m\mathrm{d}v_m\mathrm{d}w_m,
\end{aligned}$$

$$\begin{aligned}
&p_m=0,1,\ldots,N_u^{(m)},\quad s_m=0,1,\ldots,N_v^{(m)},\quad t_m=0,1,\ldots,N_w^{(m)},\\
&p_n=0,1,\ldots,N_u^{(n)},\quad s_n=0,1,\ldots,N_v^{(n)},\quad t_n=0,1,\ldots,N_w^{(n)},
\end{aligned} \tag{16}$$

where $K_u^{(m)}$, $K_v^{(m)}$, and $K_w^{(m)}$ are the geometrical orders and $N_u^{(m)}$, $N_v^{(m)}$, and $N_w^{(m)}$ the current approximation orders along the *u*-, *v*-, and *w*-coordinate, respectively, and $\mathbf{r}_{ijk}^{(m)}$ are the geometrical vector coefficients in the polynomial expansion of the mth hexahedron, while $K_u^{(n)}$, $K_v^{(n)}$, $K_w^{(n)}$, $N_u^{(n)}$, $N_v^{(n)}$, $N_w^{(n)}$, and $\mathbf{r}_{ijk}^{(n)}$ are the corresponding parameters for the nth hexahedron, which is assumed, for simplicity, to be filled with a homogeneous dielectric of contrast C_n. The source-to-field distance R is computed as

$$R = |\,\mathbf{r}_m(u_m, v_m, w_m) - \mathbf{r}_n(u_n, v_n, w_n)\,|. \tag{17}$$

Similarly, the third integral term in (14) is transformed to

$$-\int_{V_m} \nabla\cdot\mathbf{f}_m \Phi_n \mathrm{d}V_m = \frac{C_n}{\varepsilon_0} \int_{-1}^{1}\int_{-1}^{1}\int_{-1}^{1}\int_{-1}^{1}\int_{-1}^{1}\int_{-1}^{1} p_m p_n u_m^{p_m-1} v_m^{s_m} w_m^{t_m} u_n^{p_n-1} v_n^{s_n} w_n^{t_n} g(R)\mathrm{d}u_n\mathrm{d}v_n\mathrm{d}w_n\mathrm{d}u_m\mathrm{d}v_m\mathrm{d}w_m$$
$$-\frac{C_n}{\varepsilon_0} \int_{-1}^{1}\int_{-1}^{1}\int_{-1}^{1}\int_{-1}^{1}\int_{-1}^{1} p_m u_m^{p_m-1} v_m^{s_m} w_m^{t_m} u_n^{p_n} v_n^{s_n} w_n^{t_n} g(R)\mathrm{d}v_n\mathrm{d}w_n\mathrm{d}u_m\mathrm{d}v_m\mathrm{d}w_m\big|_{u_n=1}$$

$$+\frac{C_n}{\varepsilon_0} \int_{-1}^{1}\int_{-1}^{1}\int_{-1}^{1}\int_{-1}^{1}\int_{-1}^{1} p_m u_m^{p_m-1} v_m^{s_m} w_m^{t_m} u_n^{p_n} v_n^{s_n} w_n^{t_n} g(R)\mathrm{d}v_n\mathrm{d}w_n\mathrm{d}u_m\mathrm{d}v_m\mathrm{d}w_m\big|_{u_n=-1}, \tag{18}$$

where, according to (4), the first integral term in this newly developed expression corresponds to the portion of the potential Φ_n due to the volume charges inside the nth hexahedron, while the second and third terms are associated with the contributions to Φ_n due to the surface charges on the sides of this hexahedron defined by $u_n = 1$ and $u_n = -1$, respectively. Moreover, in packing the generalized Galerkin impedances for divergence-conforming basis functions in (11), the latter two terms are taken into account (and are actually computed in the first place) only for basis functions $(1-u_n)v_n^{s_n} w_n^{t_n}$ (for $p_n = 0$) and $(u_n+1)v_n^{s_n} w_n^{t_n}$ (for $p_n = 1$), respectively, and only if the dielectric properties vary across the respective side of the hexahedron (e.g., for sides

belonging to dielectric-air interfaces in the model). Analogous final expressions are obtained for the remaining two terms of the VIE-VIE generalized Galerkin impedance. Of crucial importance is that all these impedance terms, as well as VIE-SIE, SIE-VIE, and SIE-SIE ones, for basis/testing functions in (15), as well as for those in (11), can be represented as linear combinations of 3-D/3-D basic Galerkin potential integrals with only simple power functions and Green's function as integrands,

$$S(h_m, l_m, q_m, h_n, l_n, q_n) = \int_{-1}^{1}\int_{-1}^{1}\int_{-1}^{1} u_m^{h_m} v_m^{l_m} w_m^{q_m} P(h_n, l_n, q_n)\mathrm{d}u_m \mathrm{d}v_m \mathrm{d}w_m, \tag{19}$$

where P are the 3-D basic potential integrals, evaluated as

$$P(h_n, l_n, q_n) = \int_{-1}^{1}\int_{-1}^{1}\int_{-1}^{1} u_n^{h_n} v_n^{l_n} w_n^{q_n} g(R)\mathrm{d}u_n \mathrm{d}v_n \mathrm{d}w_n, \tag{20}$$

and the corresponding 3-D/2-D, 2-D/3-D, and 2-D/2-D Galerkin integrals. This is extremely important because Galerkin integrals with only simple power functions and Green's function as integrands enable rapid and accurate recursive and nonredundant procedures for evaluation of the generalized MoM impedances. Equally important is the fact that there is no need for computing the corresponding field integrals, which is not the case in SIE analysis of dielectric and composite metallic/dielectric structures, where the computation of hyper-singular field integrals is needed to find the electric and magnetic fields in coupled electric/magnetic field integral equations (EFIE/MFIE) with electric and magnetic surface currents as unknowns [17].

In specific, efficient algorithms for recursive construction of the generalized Galerkin impedances and the VSIE system matrix are developed in order to avoid redundant operations related to the indices i, j, and k for geometrical representations and p, s, and t for current

expansions within the impedances, as well as the summation indices in the Gauss-Legendre integration formulas used for numerical integration, for any pair, m and n, of hexahedral elements in the model. In addition, since the coordinates u, v and w, as well as the corresponding indices, in the integrals S in (19) and (20), and analogously for other integrals in the technique, are cyclic, the same sequence of the S integrals (for all the required values of the subscripts h_m, l_m, q_m, h_n, l_n, and q_n) for a given pair of hexahedra can be used also for the evaluation of the generalized impedances relating to the v- and w-components of the vector **D** in the two hexahedra (note that there are nine combinations for the impedances corresponding to the three components of the testing and basis vector functions in the two elements). In addition, the same sequence of the S integrals can be used both in the impedances in (16) and in the 3-D/3-D part of the impedances in (18). So, for any hexahedron pair in the model, first and only once the entire sequence of the basic Galerkin integrals S is evaluated, and these integrals are then introduced (packed) into all impedances containing them. In the next level of packing, the impedances for basis/testing functions in (15) are recursively and nonredundantly combined into the final Galerkin impedances for functions in (11).

A rapid and accurate combined numerical/analytical method is developed for the integration over curved higher order generalized hexahedral elements, for the P integrals in (20). When the distance R in (17) is relatively small or zero, the procedure of extracting the singularity is performed, which consists of analytical integration of a principal singular part of the integrand over a (generally not rectangular) parallelepiped whose parametric description is close to that of the generalized hexahedron in the vicinity of the singular point, and numerical integration of the rest using Gauss-Legendre quadrature formulas. The sides of the parallelepiped that corresponds to the generalized hexahedron specified in (9) are obtained by translating the straight segments

A_1A_2, B_1B_2, and C_1C_2 shown in Fig. 4, where these segments, in turn, are obtained differentiating the curves defined by $\mathbf{r}(u, v_0, w_0)$, $\mathbf{r}(u_0, v, w_0)$, and $\mathbf{r}(u_0, v_0, w)$ at the point (u_0, v_0, w_0). In other words, the parallelepiped is defined by the unitary vectors $\mathbf{a}_u$, $\mathbf{a}_v$, and $\mathbf{a}_w$ of the generalized hexahedron, (12), at the singular point, and hence its parametric equation:

$$\mathbf{r}_\mathrm{p}(u,v,w) = \mathbf{r}_\mathrm{c} + \mathbf{a}_{u0}(u-u_0) + \mathbf{a}_{v0}(v-v_0) + \mathbf{a}_{w0}(w-w_0) \qquad -1 \le u,v,w \le 1 \tag{21}$$

where u_0, v_0, and w_0 are the coordinates of the singular point and $\mathbf{r}_\mathrm{c} = \mathbf{r}(u_0, v_0, w_0)$, $\mathbf{a}_{u0} = \mathbf{a}_u(u_0, v_0, w_0)$, $\mathbf{a}_{v0} = \mathbf{a}_v(u_0, v_0, w_0)$, and $\mathbf{a}_{w0} = \mathbf{a}_w(u_0, v_0, w_0)$. For u close to u_0, v close to v_0, and w close to w_0, the point $M(u,v,w)$ of the curved hexahedron coincides with or is very close to the point $M_\mathrm{p}(u,v,w)$ of the parallelepiped. Therefore, in extracting the singularity in the P integrals, we subtract and add a term of the form $1/R_p$ (instead of $1/R$), where $R_\mathrm{p} = \mathbf{r}_\mathrm{c} - \mathbf{r}_\mathrm{p}(u,v,w)$ is the source-to-field distance for integration throughout the volume of the parallelepiped [22],

$$P(h,l,q) = \int_{-1}^{1}\int_{-1}^{1}\int_{-1}^{1} \left(u^h v^l w^q g(R) - u_0^h v_0^l w_0^q \cos(\beta_0 d) \frac{1}{4\pi R_\mathrm{p}} \right) \mathrm{d}u\mathrm{d}v\mathrm{d}w + \frac{u_0^h v_0^l w_0^q \cos(\beta_0 d)}{4\pi} \int_{-1}^{1}\int_{-1}^{1}\int_{-1}^{1} \frac{1}{R_\mathrm{p}} \mathrm{d}u\mathrm{d}v\mathrm{d}w \tag{22}$$

with d being determined as $d = R_\mathrm{min}$ [of course, for the observation (field) point inside the generalized hexahedron or on its surface, $d = 0$]. In (22), the first integral is well behaved in the vicinity of the point (u_0, v_0, w_0) and can be rather accurately integrated numerically, over the domain $-1 \le u,v,w \le 1$, which represents the domain of both the curved hexahedron and the parallelepiped. However, to further enhance the accuracy of the numerical integration, we subdivide this domain into a number of integration subdomains by means of coordinate surfaces

$u = u_0$, $v = v_0$, and $w = w_0$, respectively. Note that this technique remains practically the same when P is a near-singular integral, namely, when the observation point is outside the generalized hexahedron but very close to its surface, while Duffy and singularity annihilation techniques generally appear not to work well for near-singular integrals.

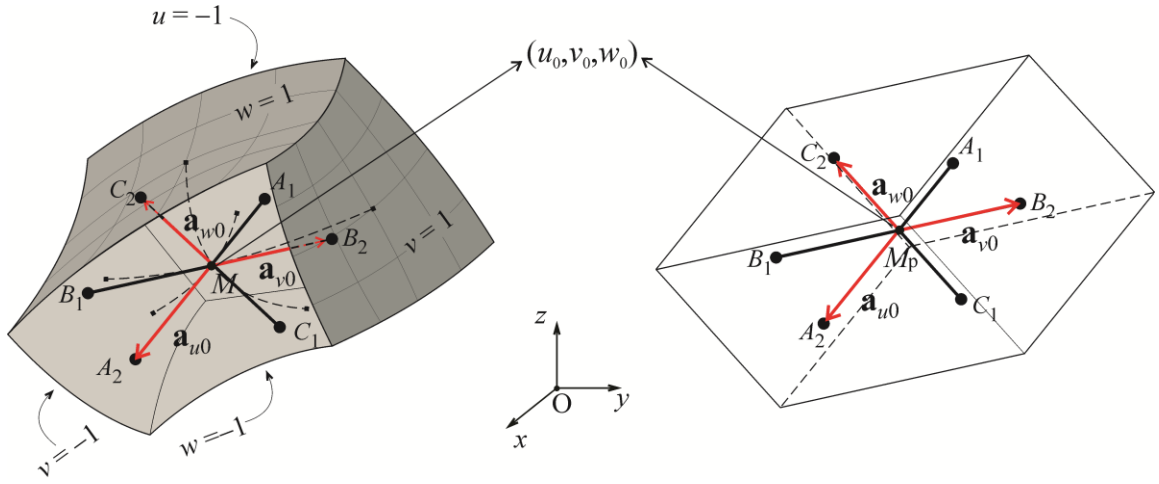

Fig. 4. Finding the parallelepiped whose parametric description is close to that of a curved higher order generalized hexahedral VIE element in the vicinity of the singular point (u_0,v_0,w_0) (note that the case presented here is for $u_0 = v_0 = w_0 = 0$) – for the singularity extraction procedure in (22) to solve the 3-D basic potential integrals over curved hexahedra.

1.5 Numerical Results and Discussion

1.5.1 Structure with Flat Surfaces and Sharp Edges

As an example of structures with flat surfaces and sharp edges and corners, consider a lossless homogenous cubical dielectric scatterer of side length a, shown in the inset of Fig. 5. Relative permittivity of the dielectric is $\varepsilon_r = 4$. Fig. 5 presents the monostatic radar cross section (RCS) of the cube, normalized to λ_0^2, as a function of a/λ_0, λ_0 being the free-space wavelength. In the higher order VIE approach, the scatterer is modeled by a single trilinear

hexahedral element ($K_u = K_v = K_w = 1$) – literally an entire-domain CEM model, which in this case reduces to a brick, with orders $N_u = N_v = N_w = 6$ for the polynomial approximation of the displacement vector in the element and only $N_{\text{unkn}}^{\text{VIE}} = 756$ unknowns (without the use of symmetry).

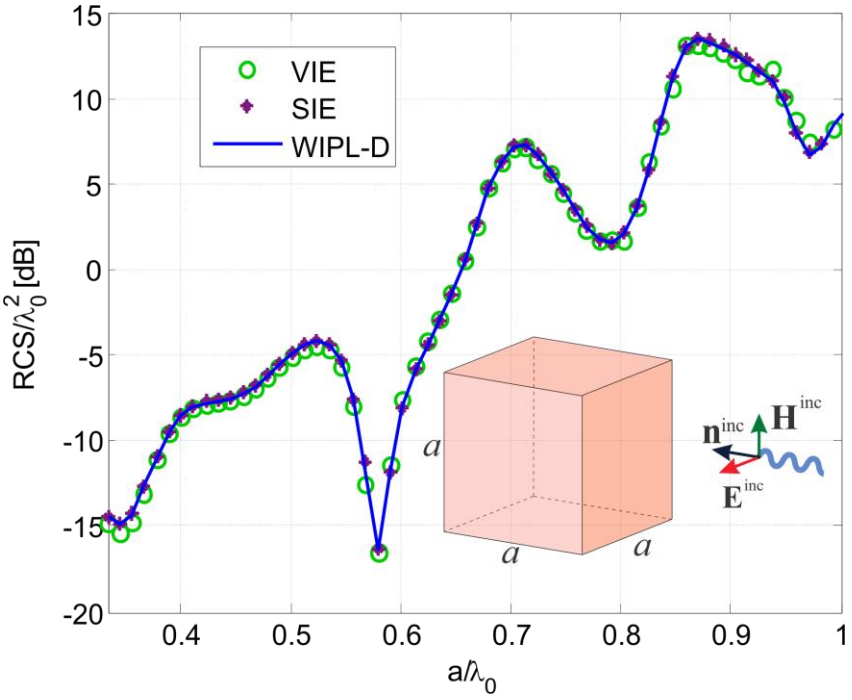

Fig. 5. Normalized monostatic radar cross section (RCS) of a dielectric ($\varepsilon_r = 4$) cube (λ_0 is the free-space wavelength): comparison of the higher order single-element (entire-domain) VIE solution with results obtained by the higher order SIE technique [17] and WIPL-D, respectively.

The VIE solution is compared to the results obtained by the higher order SIE technique [17], with the cube surface modeled by means of six bilinear quadrilateral elements ($K_u = K_v = 1$) in conjunction with the polynomial expansions for electric and magnetic surface currents of orders $N_u = N_v = 6$ in all of the elements, which results in a total of $N_{\text{unkn}}^{\text{SIE}} = 864$ unknowns, as well as with a fully *hp*-refined solution using WIPL-D, which also is a higher order SIE code.

We observe an excellent agreement between the three sets of numerical results in the whole range of frequencies considered, with the size of the higher order VIE and SIE elements at the highest frequency of the range being $e = 2\lambda_d$, where $\lambda_d = \lambda_0 / \sqrt{\varepsilon_r}$ is the wavelength in the dielectric, and with the VIE solution requiring fewer unknowns than both higher order SIE solutions.

1.5.2 Spherical Homogeneous Dielectric Scatterer

As the first example of curved dielectric structures, consider a lossless homogeneous spherical dielectric scatterer of radius *a*, shown in the top inset of Fig. 6. Relative permittivity of the dielectric is $\varepsilon_r = 4$. Fig. 6 presents the monostatic radar cross section (RCS) of the scatterer, normalized to λ_0^2, as a function of a/λ_0, λ_0 being the free-space wavelength. The numerical results obtained by three higher order VIE solutions, with the sphere modeled using (A) one curved hexahedron with geometrical orders $K_u = K_v = K_w = 2$ [Fig. 2(b)], orders $N_u = N_v = N_w = 4$ for the polynomial approximation of the displacement vector in the element, and only $N_{\text{unkn}}^{\text{VIE}} = 240$ unknowns (without the use of symmetry), (B) one hexahedron with $K_u = K_v = K_w = 4$ and $N_u = N_v = N_w = 4$, and (C) seven large elements, with the central element in the form of a cube ($K_u = K_v = K_w = 1$) and six cushion-like curved hexahedral elements ($K_u = K_v = K_w = 2$) attached to the cube sides (the mesh is shown in the lower right inset of Fig. 6) and $N_u = N_v = N_w = 6$ in all of the elements ($N_{\text{unkn}}^{\text{VIE}} = 5{,}004$), are compared with the analytical solution in the form of Mie's series. Note that the single-element models A and B (lower left inset of Fig. 6) are literally entire-domain curved CEM models.

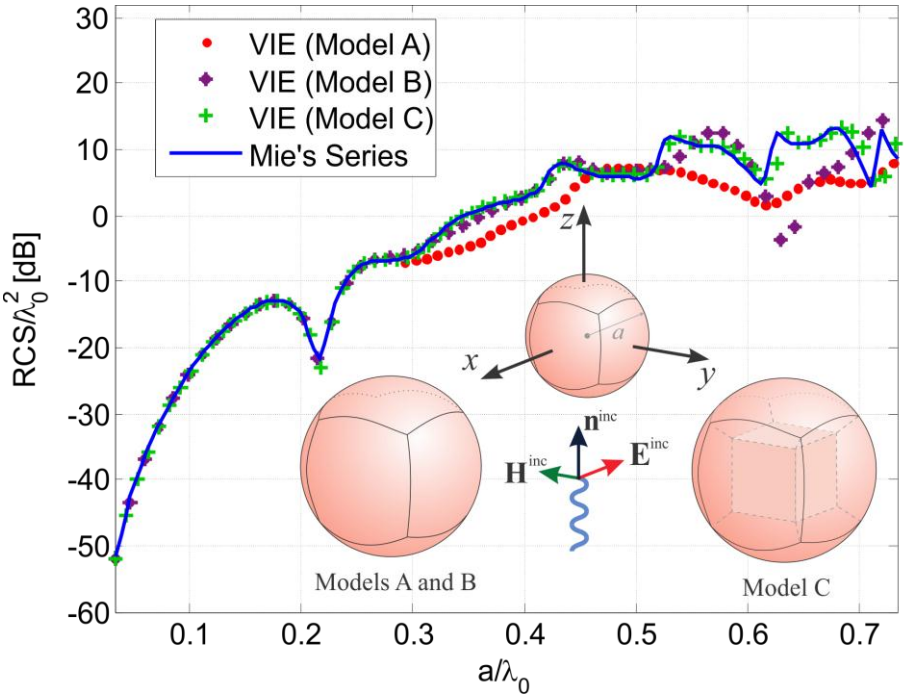

Fig. 6. Normalized monostatic radar cross section of a dielectric ($\varepsilon_r = 4$) sphere: comparison of numerical solutions obtained by three double-higher-order VIE models (A, B, and C) with the analytical solution in the form of Mie's series.

Note also that the model B is aimed to illustrate the solution behavior when the geometrical approximation is improved, while the principal purpose of the solution C is to evaluate an *hp*-refinement of the model, with both the number of elements increased (*h*-refinement) and the current approximation in the elements enhanced (*p*-refinement). We observe, in Fig. 6, that, as compared to the exact solution (Mie's series), models A and B perform well up to the frequency at which $a/\lambda_d = 0.6$ and 1.02, respectively, where $\lambda_d = \lambda_0 / \sqrt{\varepsilon_r}$ is the wavelength in the dielectric, which demonstrates a dramatic improvement of results when using geometrical modeling of the 4th order instead of the 2nd order geometrical modeling. In the latter case, when $a/\lambda_d = 1.02$, the central dimension of the single hexahedral element used to model the sphere is about $e = 2a = 2.04\lambda_d$ (sphere diameter), which indicates that the proposed double-higher-order

VIE technique allows using curved elements that are as large as $e \approx 2\lambda_d$ across. We also observe a very significant improvement of results employing the *hp*-refined model C, which gives a good agreement with Mie's series solution up to the frequency at which $a/\lambda_d = 1.38$. The largest dimension of the hexahedra in this model is approximately $e = 1.6a = 2.21\lambda_d$ for cushion-like hexahedra, while the size of the cubical element in the middle amounts to $e = 1.15\lambda_d$. In addition, note that among the three models of the sphere, models A and B have geometrical degeneracy around the corners of the hexahedral elements, which reflects on the current expansion through the Jacobian and influences the accuracy of the solution. Note also that computation of the Jacobian is actually not needed except in the first integral term in (12), since the Jacobians cancel out in final expressions for all other integral terms, as can be seen in (16) and (18).

Table I. RCS Solution Error and MoM Matrix Condition Number for a Single-Element Sphere Model vs. Element Geometrical Orders.

$K_u = K_v = K_w$	Error	Condition number
2	28%	7903.98
3	11%	8571.01
4	0.3%	3909.71

As an additional evaluation of convergence properties of the double higher-order VIE analysis, Table I gives the percentage error of RCS computation relative to the Mie's series solution, $\text{error} = \left|(\text{RCS}^{\text{Mie}} - \text{RCS}^{\text{VIE}})/\text{RCS}^{\text{Mie}}\right| \cdot 100\%$ and condition number of the MoM matrix for the sphere of diameter $d = 1.24\lambda_d$ modeled by a single curved hexahedron whose geometrical orders are varied from $K_u = K_v = K_w = 2$ to $K_u = K_v = K_w = 4$, while keeping

the current approximation orders constant, $N_u = N_v = N_w = 4$. Table II shows the error and condition number for constant geometrical orders, $K_u = K_v = K_w = 2$, and current expansion orders varied from $N_u = N_v = N_w = 4$ to $N_u = N_v = N_w = 6$. We observe in Tables I and II an excellent convergence of the VIE method with increasing both geometrical and current-approximation orders.

Table II. RCS Solution Error and MoM Matrix Condition Number for a Single-Element Sphere Model vs. Element Geometrical Orders.

$N_u = N_v = N_w$	Error	Condition number
4	28%	7903.98
5	4.7%	689578.19
6	4.1%	56342600.00

Also, as expected, the condition number is almost unaffected by the geometrical orders, while it rapidly increases with increasing the orders of basis functions. However, the orthogonality and conditioning properties of the simplest hierarchical divergence-conforming polynomial vector basis functions, in (11), can be improved as in [44],[45], for instance, and this is needed when iterative solvers are used.

1.5.3 Composite Metallic/Dielectric Sphere

As an example of composite metallic/dielectric structures, that also possess curvature, consider a dielectrically coated PEC sphere excited by a plane wave, of frequency *f* = 1 GHz, as shown in the inset of Fig. 7. The radii of the PEC sphere and the coated sphere are a = 5 cm and b = 10 cm, respectively, and the relative permittivity of the dielectric of the coating is $\varepsilon_r = 4$.

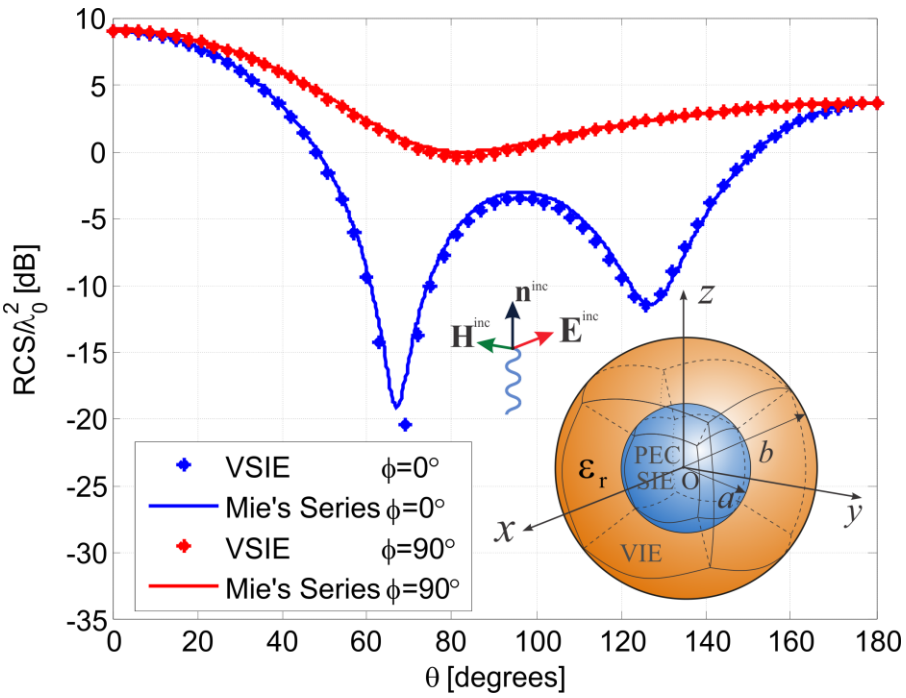

Fig. 7. Normalized bistatic radar cross section in two characteristic planes of a dielectrically coated PEC sphere ($\varepsilon_r = 4, 2a = b = 10$ cm, $f = 1$ GHz): comparison of the double-higher-order VSIE results with the exact Mie's series solution; figure inset shows a higher order VSIE mesh of the scatterer using six large cushion-like conformal hexahedral VIE elements and six curved quadrilateral SIE patches.

The coating is modeled using only six large cushion-like conformal hexahedral VIE elements with $K_u = K_v = K_w = 2$ and $N_u = N_v = N_w = 6$, and the PEC surface is modeled by six curved quadrilateral SIE patches with $K_u = K_v = 2$ and $N_u = N_v = 6$, as depicted in the figure inset, resulting in a total of $N_{\text{unkn}}^{\text{VSIE}} = 4{,}824$ unknowns. The size of the volume and surface elements in the model ranges between $0.53\lambda_d \le e \le 1.06\lambda_d$. Fig. 7 shows the computed bistatic RCS of the scatterer in two characteristic planes, where an excellent agreement of the double-higher-order VSIE results with the exact solution in the form of Mie's series is observed (the

average absolute RCS errors, over all θ angles, are 0.45 dB and 0.13 dB in planes $\varphi = 0°$ and $\varphi = 90°$, respectively).

1.5.4 Wire Antenna Coupled to an Inhomogeneous Dielectric Body

As an antenna example, consider an eight-turn helical dipole antenna near an inhomogeneous dielectric sphere composed of three concentric dielectric layers, as shown in the inset of Fig. 8 [46]. The sphere is modeled by 8 cubical ($K_u = K_v = K_w = 1$) and 72 curvilinear triquadratic ($K_u = K_v = K_w = 2$) hexahedral VIE elements, as indicated in Fig. 8, with the orders N_u, N_v, and N_w varied from 2 to 3 for different elements and in different directions, and the helical antenna is modeled by 72 straight ($K_u = 1$) SIE wire segments [46] with $N_u = 2$ for each of the segments, which results in a total of $N_{\text{unkn}}^{\text{VSIE}} = 6{,}995$ unknowns. Shown in Fig. 8 is the simulated radiation (gain) pattern of the antenna in the $\varphi = 0°$ plane, as well as the simulation results for the antenna impedance, at $f = 900\,\text{MHz}$, obtained by the proposed higher order VSIE technique and by the higher order FEM-MoM technique ($N_{\text{unkn}}^{\text{FEM-MoM}} = 7{,}447$)[46], respectively, and an excellent agreement of the two sets of results is observed, for both the far field (the average absolute

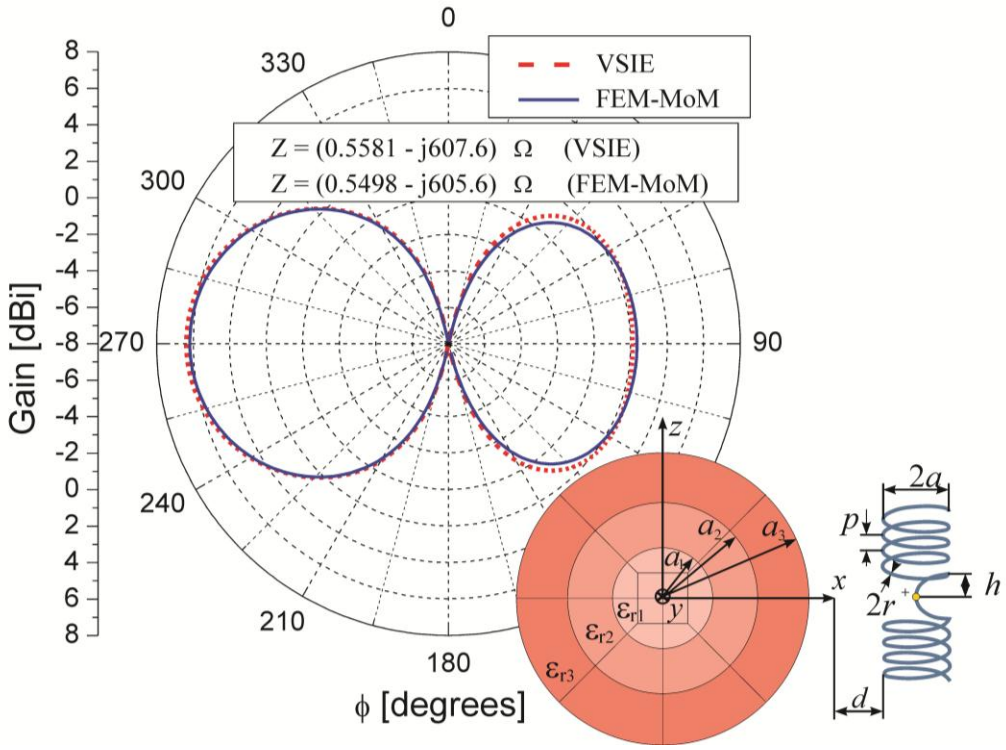

Fig. 8. Analysis of an eight-turn helical dipole antenna ($2a = 5\,\text{mm}$, $p = 1.25\,\text{mm}$, $h = 1.77\,\text{mm}$, $2r = 0.2\,\text{mm}$, $d = 5\,\text{mm}$) near an inhomogeneous, three-layer, dielectric sphere ($a_1 = 4\,\text{cm}$, $a_2 = 7\,\text{cm}$, $a_3 = 10\,\text{cm}$, $\varepsilon_{r1} = 2$, $\varepsilon_{r2} = 4$, $\varepsilon_{r3} = 6$) [36], modeled by 8 cubical and 72 curvilinear hexahedral VIE elements (figure inset shows a cross section of the VIE model): comparison of results for the radiation (gain) pattern of the antenna in the $\varphi = 0°$ plane and for the antenna input impedance obtained by the double-higher-order VSIE method with reference FEM-MoM results [46].

gain difference in the entire $\varphi = 0°$ plane is 0.28 dB) and the impedance of the antenna, with the VSIE and FEM-MoM solutions implementing identical volumetric geometrical models of the layered sphere but, of course, discretizing very different equations throughout its volume.

1.5.5 Finite Array of Dielectric Scatterers (PBG Waveguide)

As the next example, consider an infrared (IR) photonic band gap (PBG) waveguide realized, as a combination of PBG waveguide concepts proposed in [47] and [48], as a pattern of 72 circular dielectric (GaAs) rods, with $\varepsilon_r = 11.4$, in an air background shown in Fig. 9(a). The height of each cylinder is h = 1.11 μm, diameter is $2a$ = 288 nm, and the distance between the axis of adjacent cylinders is d = 750 nm. The array of rods is situated between two PEC plates of size 4.8×8.5 μm, perpendicular to the cylinder axes. The distance between the plates is D = 1.6 μm, and they are positioned symmetrically in all directions with respect to the PBG array. The structure is excited by a l = 674 nm long wire dipole at its edge [Fig. 9(a)], with the dipole being parallel to the axes of cylinders. In the double-higher-order VSIE model, each cylinder is modeled by a single curved hexahedral volume element with $K_u = K_v = K_w = 2$ and $N_u = N_v = N_w = 3$, as depicted in Fig. 9(b), which yields a total count of $N_{\text{unkn}}^{\text{VSIE}} = 7{,}965$ unknowns (with no use of symmetry), including the SIE unknowns for modeling the wire dipole and the PEC plates. The near-field distributions calculated in the plane cutting across the dielectric rods at 2/3 of their height, perpendicularly to their axes [this plane is sketched in Fig. 10(a)], at frequencies f_1 = 120 THz, f_2 = 175 THz, and f_3 = 220 THz, respectively, are shown in Fig. 10, where PBG effects are clearly observed.

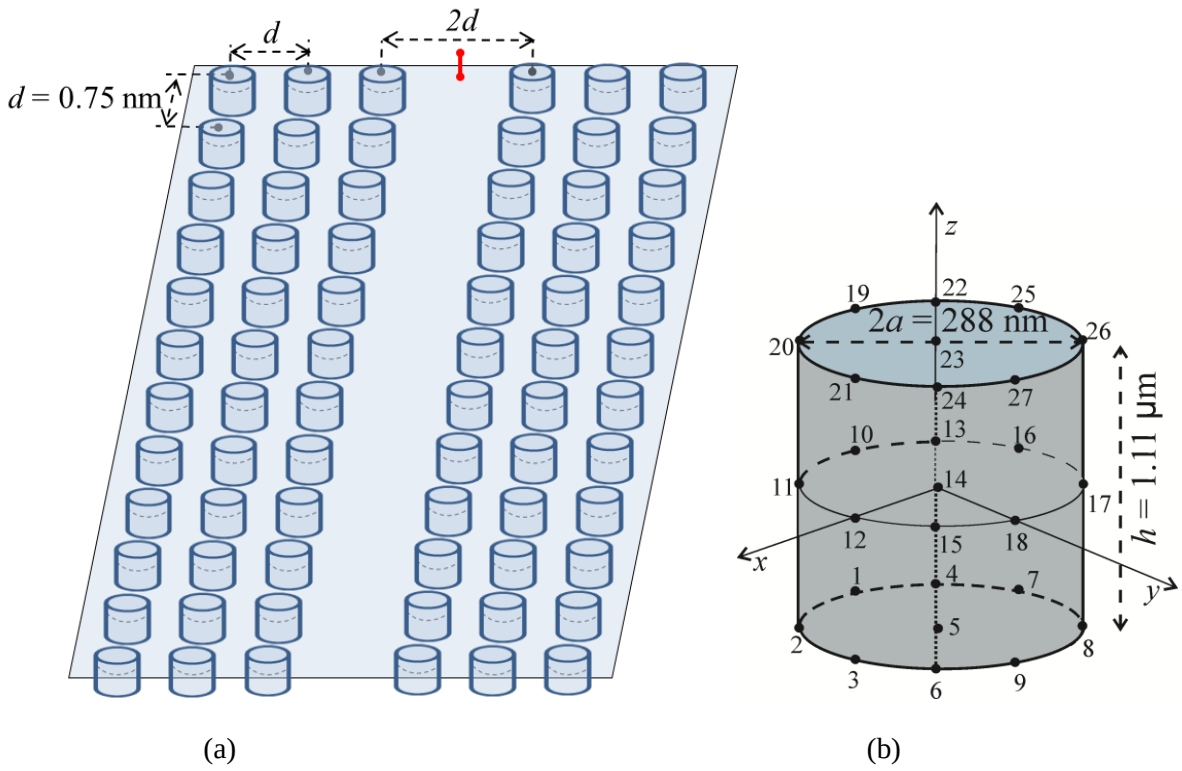

(a) (b)

Fig. 9. (a) IR PBG waveguide realized as a pattern of circular dielectric ($\varepsilon_r = 11.4$) rods between two PEC plates (plates not shown) in an air background (the structure is excited by a wire dipole at its edge) and (b) modeling of each cylinder by a single curved hexahedral VIE element of the second geometrical orders.

Field plots in Fig. 10(a) and (b) show no propagation through the structure at the frequency f_1 (stop band of the waveguide within the stop band of the PBG lattice), Fig. 10(c) and (d) depict waveguide propagation at the frequency f_2 (waveguide pass band within the PBG stop band), while the plots in Fig. 10(e) and (f) demonstrate unobstructed propagation through the PBG structure at the frequency f_3 (inside the pass band of the PBG lattice).

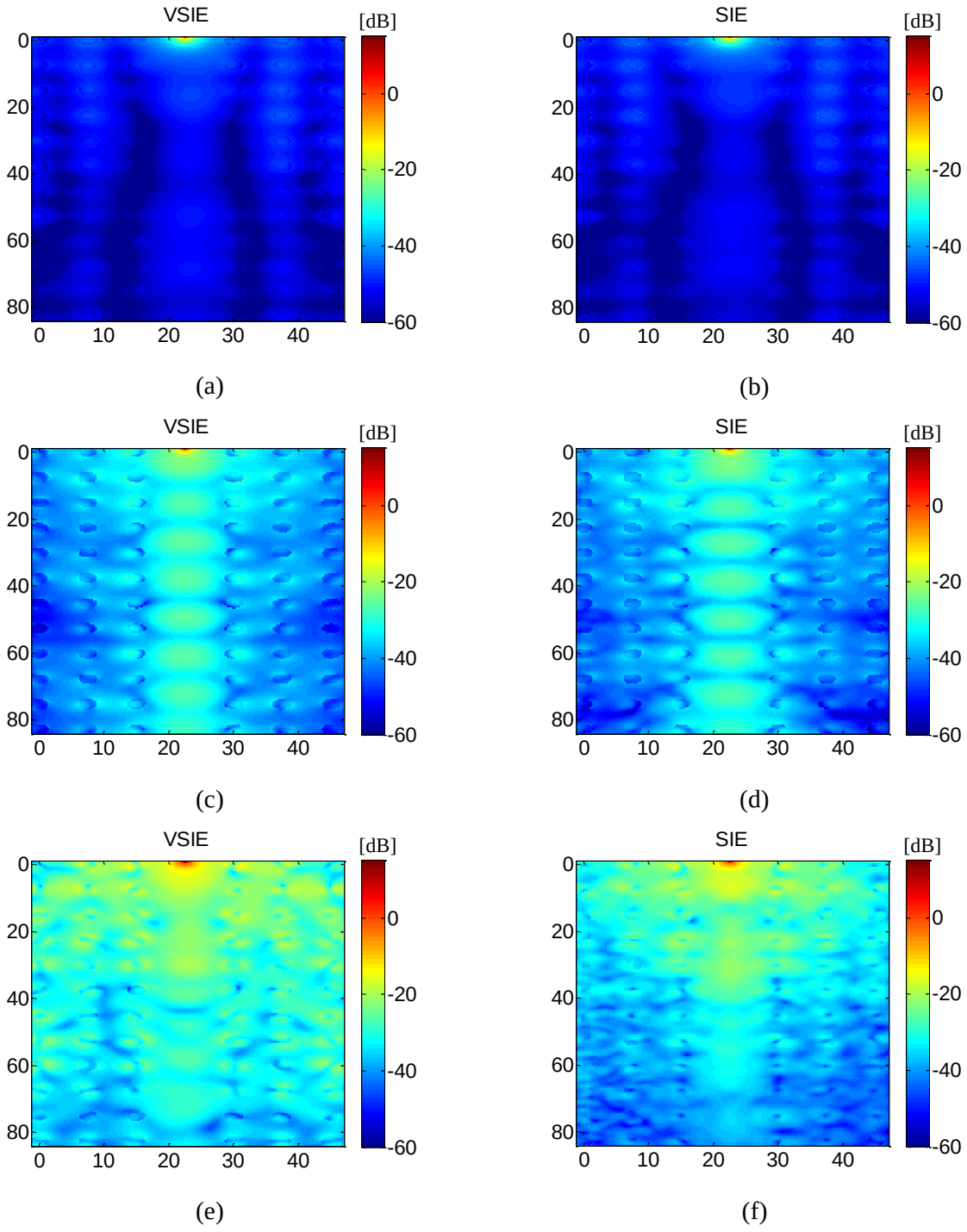

Fig. 10. Magnitude of the near electric field of the PBG structure in Fig. 10(a) computed, in the plane indicated in Fig. 10(a), at frequencies (a)-(b) $f_1 = 120$ THz, (c)-(d) $f_2 = 175$ THz, and (e)-(f) $f_3 = 220$ THz, by (a), (c), (e) the double-higher-order VSIE technique [based on the model of cylinders shown in Fig. 10(b)] and by (b), (d), (f) the double-higher-order SIE technique [17].

Moreover, at all frequencies, the double-higher-order VSIE solutions [Fig. 10(a), (c), and (e)] are compared to the results [in Fig. 10(b), (d), and (f)] obtained by the double-higher-order SIE technique [17], with the surface of each cylinder modeled by six curved quadrilateral patches with $K_u = K_v = 2$ and $N_u = N_v = 3$ ($N_{\text{unkn}}^{\text{SIE}} = 15{,}741$). A good agreement of the two sets of numerical results is observed.

1.5.6 Human Bone Model

As an example of curved, geometrically complex dielectric objects, consider a human bone model, shown in Fig. 11(a), illuminated by a plane wave at a frequency f = 2.5 GHz. This is also an example of bodies with high electric contrast and losses, namely, the bone permittivity and conductivity are $\varepsilon_r = 11.38$ and $\sigma = 0.39$ S/m [49]. The electrical dimensions of the bone are $5.4518\lambda_d \times 11.5947\lambda_d \times 4.3303\lambda_d$. The results obtained by a

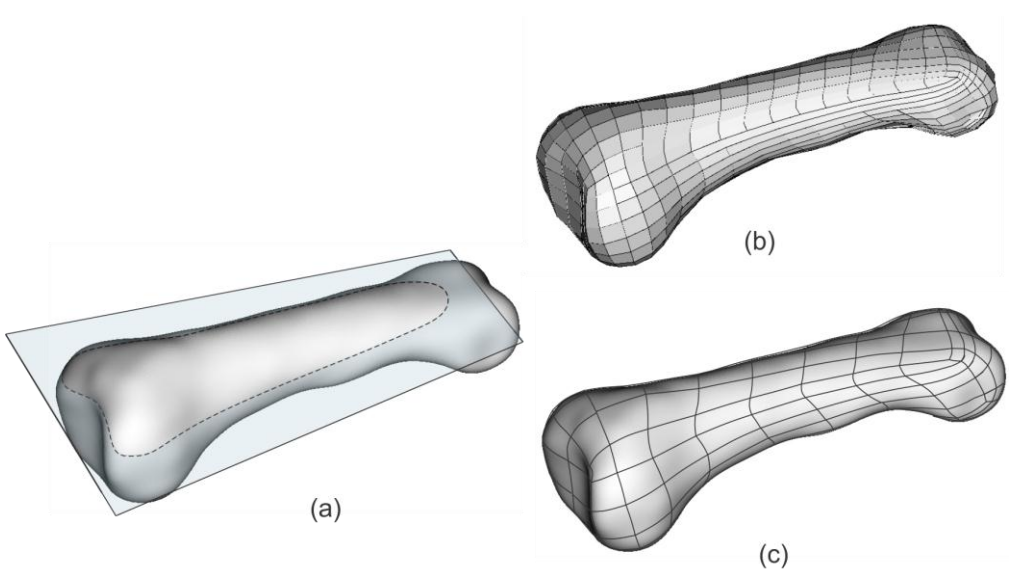

Fig. 11. VIE modeling of a human bone ($\varepsilon_r = 11.38$, σ = 0.39): (a) bone geometry, (b) trilinear VIE model, and (c) triquadratic curved VIE model.

trilinear ($K_u = K_v = K_w = 1$) 1,024-element VIE model, shown in Fig. 11(b), with $N_u = N_v = N_w = 2$, and a triquadratic ($K_u = K_v = K_w = 2$) curved 128-element VIE model, shown in Fig. 11(c), with $N_u = N_v = N_w = 3$, are compared with a fully *hp*-refined WIPL-D reference solution.

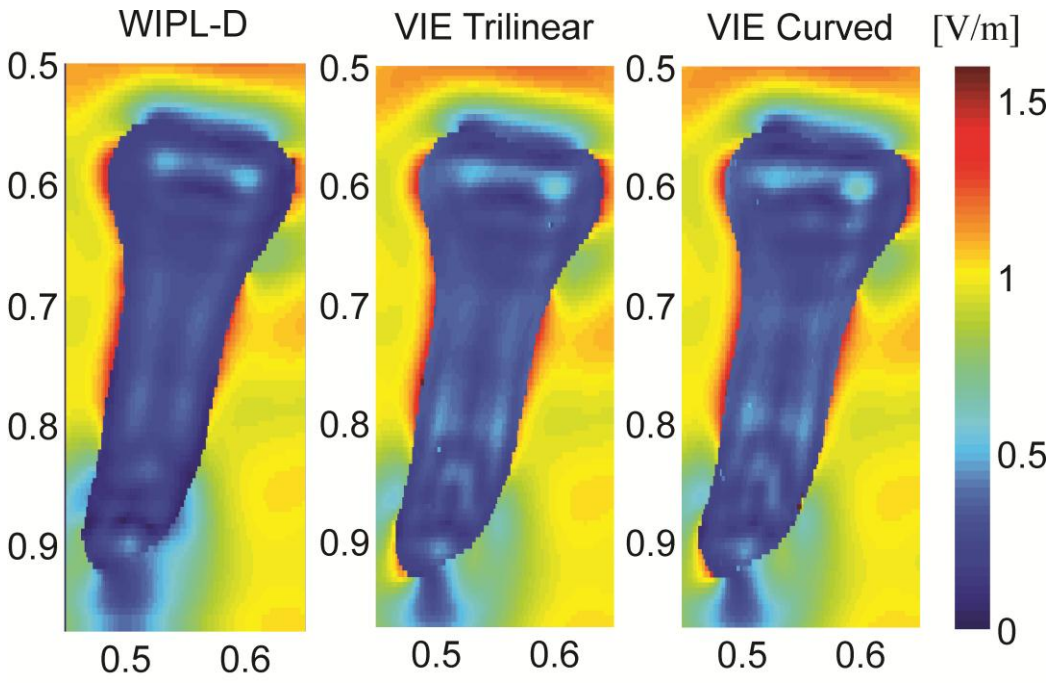

Fig. 12. Magnitude of the electric field in the plane indicated in Fig. 11(a) near or inside a bone model excited by a plane wave with a normal incidence to the plane at f = 2.5 GHz: comparison of VIE results obtained using models in Fig. 11(b) and (c) and a fully *hp*-refined WIPL-D reference solution.

Note that the average dimensions of elements in the trilinear and triquadratic models are $e = 0.73\lambda_d$ and $e = 1.45\lambda_d$, respectively. Fig. 12 shows the near (internal or external) total electric field computed in the plane indicated in Fig. 11(a). We observe a good agreement between the two higher order VIE solutions and the reference solution, with a large saving in the

number of unknowns, $N_{\text{unkn}}^{\text{VIE}} = 11{,}088$ instead of $N_{\text{unkn}}^{\text{VIE}} = 25{,}856$, in favor of the model with curved VIE elements.

1.5.7 Satellite Dish Antenna with a Dielectric Radome

As the final example, consider a satellite antenna with a parabolic dish reflector, excited by a cylindrical waveguide section of diameter $h = 0.08$ m and length $l = 0.1$ m, and covered by a hemispherical dielectric radome depicted in the inset of Fig. 13. The reflector dish opening and the radome surface diameters are $d = 0.8$ m and $D = 0.82$ m respectively. The radome is 6 mm thick and its permittivity is $\varepsilon_r = 2.5$. The operating frequency is $f = 3$ GHz, and $D = 8.2\,\lambda_0 = 13.0\lambda_d$. The VSIE model consists of 170 elements, namely, 48 hexahedral VIE elements with $K_u = K_v = K_w = 2$, $N_u = 1$, and $N_v = N_w = 4$, 120 quadrilateral SIE patches with $K_u = K_v = 1$ and $N_u = N_v = 4$, and two SIE wire segments with $K_u = 1$ and $N_u = 3$, and resulting in a total of $N_{\text{unkn}}^{\text{VSIE}} = 6{,}933$ unknowns. More specifically, the VIE radome model is a layer of 48 thin volumetric blocks, with maximal dimensions amounting to $e = 2.34\lambda_d$ and different current approximation orders in radial direction ($N_u = 1$) and directions tangential to the radome surface ($N_v = N_w = 4$). The radiation (gain) pattern of the antenna in the $\varphi = 0°$ plane computed by the VSIE is compared in Fig. 13 with the pure SIE solution by WIPL-D, which requires $N_{\text{unkn}}^{\text{SIE}} = 23{,}908$ unknowns, and we observe an excellent agreement of the two sets of results.

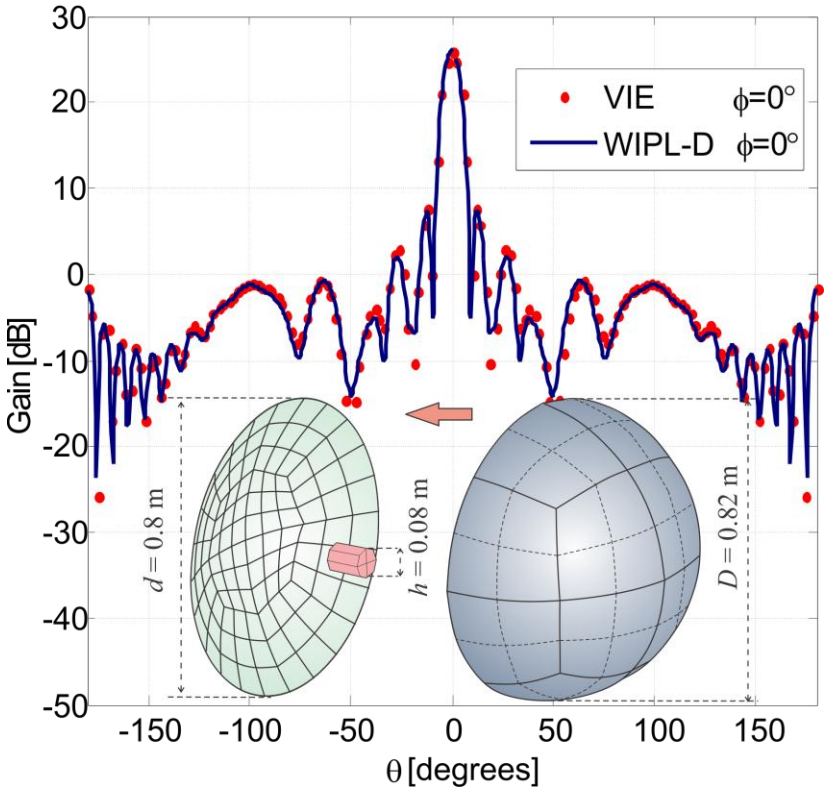

Fig. 13. Analysis of a parabolic satellite dish antenna excited by a cylindrical waveguide section (f = 3 GHz) and covered by a hemispherical dielectric ($\varepsilon_r = 2.5$) radome (6-mm thick): comparison of results for the radiation pattern (gain) of the antenna in the $\varphi = 0°$ plane obtained by the double-higher-order VSIE method (model with 48 curved hexahedral VIE elements, 120 curved quadrilateral SIE patches, and two SIE wire segments) with reference WIPL-D pure-SIE results.

1.6 Summary

In this section of the thesis was proposed a double-higher-order large-domain Galerkin-type method of moments for modeling of composite wire-plate-dielectric radiation/scattering structures. The method is based on the volume integral equation approach for dielectric parts and the surface integral equation approach for metallic parts of the composite structure. It employs Lagrange-type interpolation generalized hexahedra and quadrilaterals of arbitrary geometrical-

mapping orders for the approximation of geometry and hierarchical divergence-conforming polynomial vector basis functions of arbitrary expansion orders for the approximation of currents within the elements. The results obtained by the double-higher-order VSIE method have been validated against the analytical solutions and the numerical results obtained by the double-higher-order SIE and FEM-MoM techniques, as well as the WIPL-D results. Numerical examples have demonstrated that the double-higher-order VIE and VSIE modeling provides a useful alternative to other, more frequently used, types of CEM techniques and either on par or a more efficient solution in many cases, even when compared to techniques implementing similar types of higher order numerical discretization. It has also been demonstrated that both components of the double-higher-order VIE/SIE modeling, i.e., higher order geometrical modeling and higher order current modeling, are essential for accurate and efficient MoM-VSIE computations.

2 IMPLEMENTATION OF LAGRANGE-TYPE MODELING OF CONTINUOUS PRMITTIVITY VARIATION

2.1 Introduction

One of the most popular techniques in the frequency domain for modeling scattering from highly inhomogeneous dielectric objects is the finite element method (FEM), hybridized with the method of moments/surface integral equation (MoM-SIE) [46]. In this approach the FEM domain is terminated by the surface to which the surface equivalence principle is applied: the closed region is solved by FEM, while the open region is simulated by MoM-SIE [17]. Both volume and surface geometrical discretization elements contribute to the total number of unknowns.

An alternative to this approach is the method of moments/volume integral equation (MoM-VIE) technique that was discussed in section 1. The VIE approach has the same capabilities for the modeling of inhomogeneous and anisotropic dielectric materials as FEM, but with certain advantages. VIE does not require additional unknowns, resulting from surface discretization. Moreover, it does not suffer from numerical resonance problems occurring due to the surface equivalence principle.

In this section of the thesis we enhance the versatility of the method by implementing Lagrange-type modeling of the continuously varying dielectric parameters. Not only does this method allow for usage of a piecewise-constant approximation of the changing dielectric properties within the object (properties within each element are constant), but also variation of them within each of the discretization elements (continuously inhomogeneous geometrical elements). This enables direct representation of the continuously inhomogeneous materials and

demonstrates efficiency in comparison with a piecewise-homogeneous version of the method. To our knowledge, this is the first implementation of a volume integral equation with double-higher-order inhomogeneous discretization elements.

As one of the examples of a real world application, where modeling of the Lagrange-type continuously inhomogeneous permittivity is required, we compute the scattering from the melting hailstone. Most simulation approaches of this type of hydrometeors simplify the hail model into a homogeneous water-ice mixture of a canonical shape [67][68]. However, various simulations and measurements [69] show that this approach has certain limitations and precise modeling is required. A full-wave analysis of the electromagnetic scattering from the hailstones has conventionally been performed using the T-matrix [65] and discrete dipole approximation (DDA) [66] methods. However, to the best of our knowledge, practically all working T-matrix tools are only able to calculate scattering properties of rotationally symmetric particles and, more precisely, exclusively those with smooth surfaces. Moreover, the T-matrix method is restricted to the modeling of piecewise-homogeneous bodies, while the DDA method can be applied to arbitrarily shaped and highly inhomogeneous particles. However, the numerical accuracy of the method is relatively low, and improves slowly with an increase in the number of “dipoles”, which makes the DDA computation very burdensome. The DDA can be thought of as the most rudimentary version of the method of moments in the volume integral equation formulation. Therefore, higher-order continuously-inhomogeneous VIE formulation overcomes the limitations of both methods and provides an excellent tool for atmospheric particle modeling. The second practical example, demonstrates the efficiency of the method via scattering from the classical continuously inhomogeneous structure – Luneburg lens. The advantages and the efficiency of

higher order modeling are demonstrated by comparison with the commercial EM software HFSS.

2.2 Implementation Details

To implement continuous variations of medium parameters into MoM-VIE, we utilize the already developed Lagrange interpolating scheme for defining element spatial coordinates in (9), which can be conveniently reused to govern the change of the equivalent complex permittivity ε_e within the element in [40], as follows:

$$\varepsilon_e(u,v,w) = \sum_{i=0}^{K_u}\sum_{j=0}^{K_v}\sum_{k=0}^{K_w} \varepsilon_{e,ijk} L_i^{K_u}(u) L_j^{K_v}(v) L_k^{K_w}(w), \quad -1 \le u,v,w \le 1, \tag{23}$$

where $\varepsilon_{e,ijk} = \varepsilon_e(u_i, v_j, w_k)$ are the permittivity values at the points defined by $(K_u+1)(K_v+1)(K_w+1)$ position vectors of spatial interpolation nodes $\mathbf{r}_{ijk}$. In the case of $K_u = K_v = K_w = 1$, ε_e is a trilinear function throughout the element volume, governed by the given fixed values at 8 points – hexahedron vertices. For $K_u = K_v = K_w = 2$, the values for ε_e are defined at 27 interpolation nodes, and the corresponding profiles are triquadratic functions etc. This technique allows simple definitions of inhomogeneity profiles, as it utilizes the nodes already defined by the generalized hexahedral mesh.

The matrix element corresponding to the volume testing $\mathbf{f}_m$ and basis $\mathbf{f}_n$ functions defined on the *m*th and *n*th generalized hexahedral volume elements (V_m and V_n), respectively, in the model are given by (14), which yields

$$Z_{mn} = \int_{V_m} \frac{1}{\varepsilon_{en}} \mathbf{f}_m \cdot \mathbf{f}_n \mathrm{d}V_m - \omega^2 \mu_0 \int_{V_m} \mathbf{f}_m \int_{V_n} \mathbf{f}_n C_n g \mathrm{d}V_n \mathrm{d}V_m$$
$$- \frac{1}{\varepsilon_0} \left[\int_{V_m} \mathbf{f}_m \int_{V_n} \nabla' \cdot (C_n \mathbf{f}_n) \cdot \nabla g \mathrm{d}V_n \mathrm{d}V_m + \int_{V_m} \mathbf{f}_m \int_{S_n} \mathbf{n} \cdot (C_n \mathbf{f}_n) \nabla g \mathrm{d}\mathbf{S}_n \mathrm{d}V_m \right] =$$
$$\int_{V_m} \frac{1}{\varepsilon_{en}} \mathbf{f}_m \cdot \mathbf{f}_n \mathrm{d}V_m - \omega^2 \mu_0 \int_{V_m} \mathbf{f}_m \int_{V_n} \mathbf{f}_n C_n g \mathrm{d}V_n \mathrm{d}V_m + \frac{1}{\varepsilon_0} \int_{V_m} \nabla \cdot \mathbf{f}_m \int_{V_n} C_n \nabla \cdot \mathbf{f}_n g \mathrm{d}V_n \mathrm{d}V_m$$
$$+ \frac{1}{\varepsilon_0} \int_{V_m} \nabla \cdot \mathbf{f}_m \int_{V_n} \mathbf{f}_n \cdot \nabla C_n g \mathrm{d}V_n \mathrm{d}V_m + \frac{1}{\varepsilon_0} \int_{V_m} \nabla \cdot \mathbf{f}_m \int_{S_n} C_n \mathbf{f}_n \cdot \mathbf{n} g \mathrm{d}V_n \mathrm{d}V_m \quad , \qquad (24)$$
$$- \frac{1}{\varepsilon_0} \int_{S_m} \mathbf{f}_m \cdot \mathbf{n} \int_{V_n} C_n \nabla \cdot \mathbf{f}_n g \mathrm{d}V_n \mathrm{d}S_m - \frac{1}{\varepsilon_0} \int_{S_m} \mathbf{f}_m \cdot \mathbf{n} \int_{V_n} \mathbf{f}_n \cdot \nabla C_n g \mathrm{d}V_n \mathrm{d}S_m$$
$$- \frac{1}{\varepsilon_0} \int_{S_m} \mathbf{f}_m \cdot \mathbf{n} \int_{S_n} C_n \mathbf{f}_n \cdot \mathbf{n} \mathrm{d}S_n \mathrm{d}S_m$$

In case permittivity is a constant, all terms including ∇C_n are vanishing. However, for continuously inhomogeneous elements, ∇C_n is represented as

$$\nabla C_n = \frac{\partial C_n}{\partial u} \hat{\mathbf{u}} + \frac{\partial C_n}{\partial u} \hat{\mathbf{v}} + \frac{\partial C_n}{\partial u} \hat{\mathbf{w}} \qquad \frac{\partial C_n}{\partial u} = \frac{\partial}{\partial u} \left(\frac{\varepsilon_\mathrm{e} - \varepsilon_0}{\varepsilon_\mathrm{e}} \right) = \frac{\varepsilon'_\mathrm{e} \varepsilon_0}{\varepsilon_\mathrm{e}^2}, \qquad (25)$$

where $\hat{\mathbf{u}}$, $\hat{\mathbf{v}}$ and $\hat{\mathbf{w}}$ are unit vectors directed as element unitary vectors $\frac{\partial \mathbf{r}}{\partial u}$, $\frac{\partial \mathbf{r}}{\partial v}$ and $\frac{\partial \mathbf{r}}{\partial w}$ respectively. Taking into account the fact that permittivity within each element is represented as in (23), the calculation of partial derivatives in (25) is a matter of simple analytical differentiation of the Lagrange polynomials.

2.3 Numerical Results and Discussion

2.3.1 Continuously Inhomogeneous Structure with Flat Surfaces and Sharp Edges

As a first example of VIE analysis of a continuously inhomogeneous structure with sharp edges, consider a lossless cubical dielectric ($\mu_\mathrm{r} = 1$) scatterer, of size *a*, and a linear radial

variation of relative permittivity ($\varepsilon_r = \varepsilon_r'$) from $\varepsilon_r = 1$, at the surface, to $\varepsilon_r = 6$, at the center of the cube, as depicted in the inset of the Fig. 14. The scatterer is situated in free space and illuminated by a uniform plane wave incident normal to one face of the scatterer,

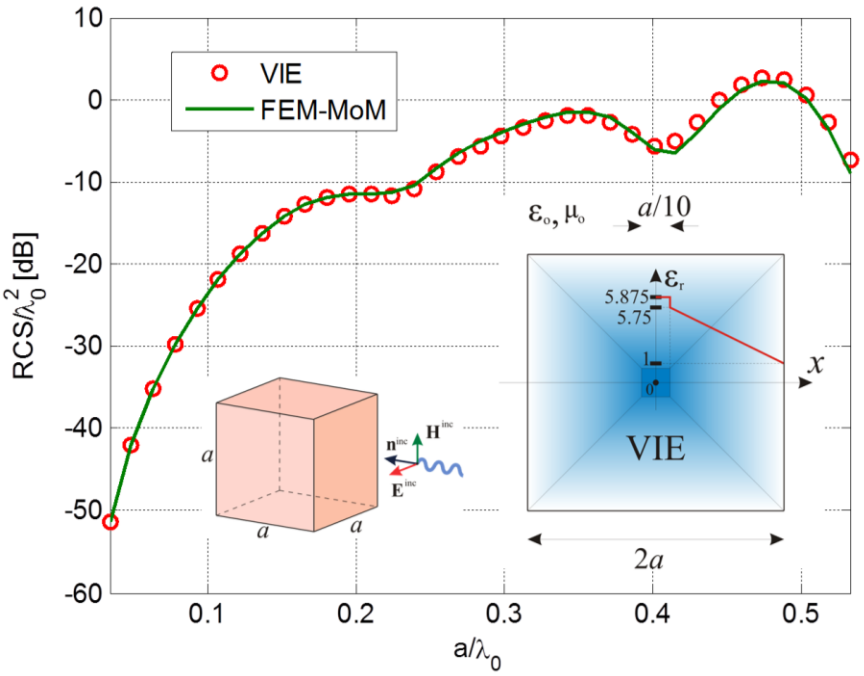

Fig. 14. Normalized monostatic radar cross section (λ_0 is the free-space wavelength) of a continuously inhomogeneous cubical scatterer computed by the continuous-MoM-VIE and continuous-FEM-MoM.

as shown in Fig. 14. To represent this permittivity variation using the expansions in (23), the cube is modeled by 7 trilinear hexahedral finite elements of the first geometrical order. Namely, one small cube-like hexahedral, $a/10$ in length, is situated at the cube center and surrounded by 6 "cushion"-like hexahedra between the central cube and the scatterer surface. The field/current approximation orders are $N_u = N_v = N_w = 6$ for all "cushions", resulting in a total of $N_{\text{unkn}}^{\text{VIE}} = 1{,}552$ unknowns (FEM required $N_{\text{unkn}}^{\text{FEM}} = 2{,}560$ unknowns). Validation of the

continuously inhomogeneous cubical VIE model, using large curved hexahedral elements with continuously changing ε_r, is carried out in comparison with solutions obtained by higher order FEM-MoM [41], [46]. Fig. 14 illustrates a monostatic radar cross section (RCS) of the cube, normalized to λ_0^2, as a function of a/λ_0, λ_0 being the free-space wavelength.

2.3.2 Continuously Inhomogeneous Curved Structure

As an example, illustrating the efficiency of the proposed method in modeling of continuously inhomogeneous structures, we consider a lossless spherical dielectric ($\mu_r = 1$) scatterer, of radius $a = 10\,\text{cm}$, situated in free space and illuminated by a uniform plane wave of frequency $f = 1.5\,\text{GHz}$, impinging from $\theta_{\text{inc}} = 0°$ and $\phi_{\text{inc}} = 0°$ direction. Relative permittivity of the sphere $\varepsilon_r(r) = 6 - \dfrac{5r}{a}$, as depicted in the inset of Fig. 15, is a linear function of a radial coordinate r with an origin at the center of the sphere. The sphere is modeled by 7 curvilinear hexahedral elements of the second geometrical order ($K_u = K_v = K_w = 2$). In specific, the central sphere-like hexahedron of radius $a/20$ and 6 "cushion"-like hexahedra between the central sphere and the scatterer surface. The field/current approximation for all elements are $N_u = N_v = N_w = 6$, resulting in total $N_{\text{unkn}}^{\text{tot}} = 5076$ unknowns.

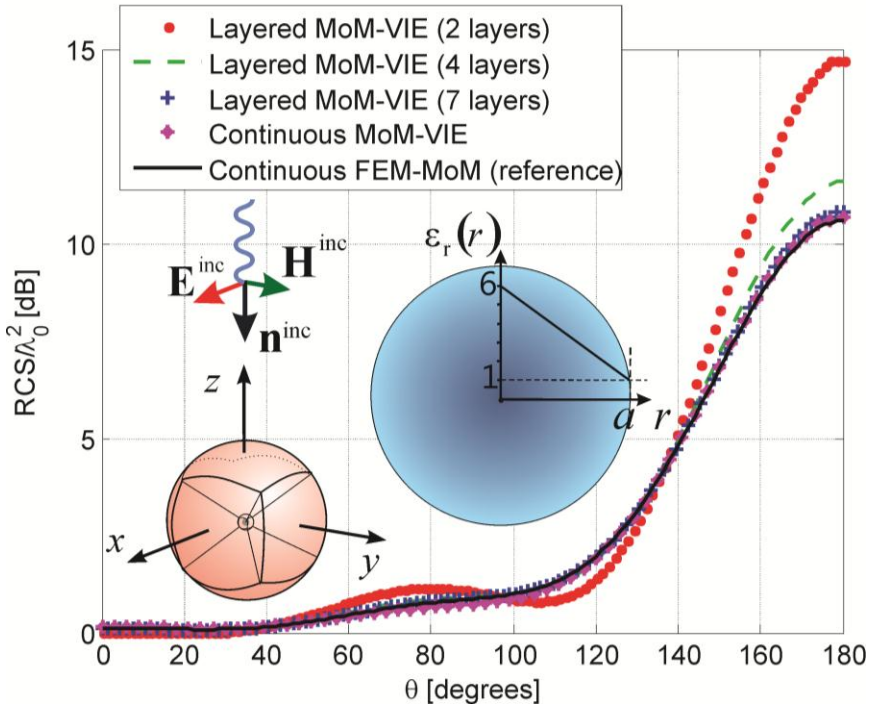

Fig. 15. Normalized bistatic RCS results of the inhomogeneous dielectric spherical scatterer, excited by a uniform plane wave ($\theta_{inc}=90°, \phi_{inc}=0°$), in the $\phi=0°$ cut, obtained by the proposed continuous-MoM-VIE model, by the three piecewise-constant MoM-VIE models and reference continuous-FEM-MoM solution [41].

Validation and efficiency of the continuously inhomogeneous MoM-VIE model, is carried out in comparison with MoM-VIE simulations of piecewise homogeneous approximate models of the structure and a continuous-FEM-MoM as a reference solution. Three different piecewise homogeneous models are constructed for the comparison, where the inhomogeneous "cushion"-like elements are replaced by $N_L = 2, 4, \text{and } 7$ layers of thin homogeneous "cushions" of $K_u = K_v = K_w = 2$ geometrical and $N_u = N_v = N_w = 4$ current approximation orders. Fig. 15 shows the normalized to λ_0^2 bistatic radar cross section (RCS) of the sphere, λ_0 being the free-space wavelength, of the scatterer in a characteristic plane ($\phi = 0°$). It can be observed that with

increasing of N_{L}, solution obtained by piecewise homogeneous modeling converges to the results of the continuously inhomogeneous MoM-VIE analysis, as well as that the continuous-MoM-VIE solution accurately matches reference continuous-FEM-MoM [41] solution. In addition, the continuous MoM-VIE approach demonstrates advantages in both computational time and number of unknowns in comparison with the most precise piecewise-homogeneous $N_{\mathrm{L}} = 7$ layered MoM-VIE model, see Table III.

Table III. Computational Time and Number of Unknowns Comparison for Continuous MoM-VIE Sphere Model and its Piecewise-constant Approximations.

	Number of unknowns	Time [sec]
Continuous	5076	1521
Layered $N_{\mathrm{L}} = 2$	2784	315
Layered $N_{\mathrm{L}} = 4$	5280	1120
Layered $N_{\mathrm{L}} = 7$	9024	3307

2.3.3 Realistic Model: Egg-shaped Hail

The third example is illustrating real-life application of the method. We consider an egg-shaped melting hailstone with a linear radial variation of the relative permittivity from $\varepsilon_{\mathrm{r}} = 20.71 - \mathrm{j}5.23$ (wet hail) at the surface to $\varepsilon_{\mathrm{r}} = 3.14 - \mathrm{j}0.004$ (dry hail) [68] at the center of the object, as depicted in the inset of Fig. 16. Similarly to the first example, the hailstone is modeled by only seven curvilinear hexahedral VIE elements with $K_u = K_v = K_w = 2$ and $N_u = N_v = N_w = 6$, resulting in a total of $N_{\mathrm{unkn}}^{\mathrm{VIE}} = 5076$ unknowns and $T^{\mathrm{VIE}} = 2674$ seconds of computational time per frequency. Validation of the higher order MoM-VIE model is carried out in comparison with solutions obtained by the higher order FEM-MoM [41], with the same continuously inhomogeneous large curved hexahedral FEM elements, but with completely

different field equations and numerical procedure. The FEM simulation required $N_{\text{unkn}}^{\text{FEM}} = 5646$ number of unknowns and $T^{\text{FEM}} = 6956$ seconds of computational time. Shown in Fig. 16 is the normalized monostatic RCS of the hailstone for the wave incident from the negative z direction, computed in frequency range from 1 G no Hz to 10 GHz, where we observe an excellent agreement of the two numerical methods.

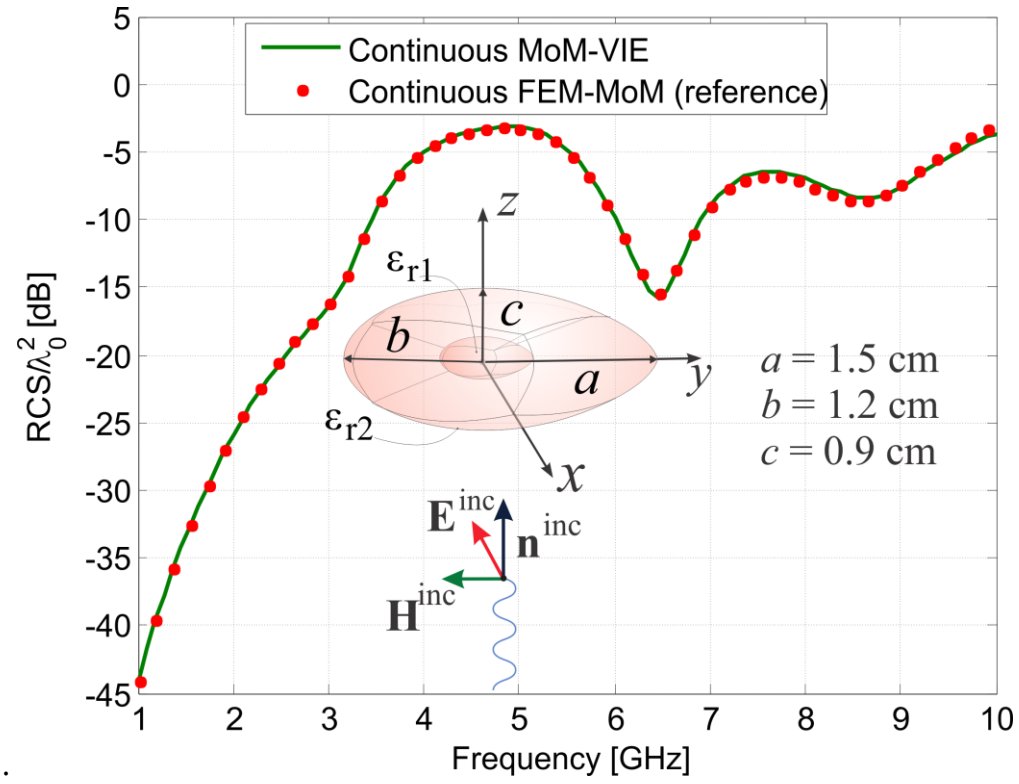

.

Fig. 16. Normalized monostatic radar cross section of an egg-shaped continuously inhomogeneous melting hailstone model (shown in the inset) computed by the continuous-MoM-VIE and continuous-FEM-MoM [41].

2.3.4 Luneburg Lens

As the last example, consider a Luneburg lens 5λ in radius, which is a dielectric sphere with permittivity varying radially from 2, at its center, to 1, at its surface, as $\varepsilon_r(r) = 2 - \left(\frac{r}{R}\right)^2$, where R is the radius of the lens. The lens is illuminated by the plane wave propagating against *z*-direction and polarized as it is shown in the Fig. 17. The lens is modeled by 112 inhomogeneous curvilinear hexahedral VIE elements with $K_u = K_v = K_w = 2$ and $N_u = N_v = N_w = 4$, resulting in a total of $N_{\text{unkn}}^{\text{VIE}} = 22{,}272$ unknowns and $T^{\text{VIE}} = 46{,}392$ seconds of computational time. Note that, due to the symmetric nature of the structure, only one fourth of the lens was modeled.

Validation of the higher order MoM-VIE model is carried out by demonstration of the lens effect and comparison of near field results with ones obtained by commercial EM software HFSS. The results for the normalized real part of the *y*-component of electric field vector in the plane passing through the lens along the propagation direction of the plane wave is shown in the Fig. 17. The result obtained in both simulations clearly demonstrate the focusing effect of the lens, while cross-validating each other (acknowledging the slight differences in the color coding used in the software). In addition, the proposed continuous MoM-VIE technique demonstrates computational efficiency in comparison with HFSS simulation, which required 175,040 homogeneous tetrahedra, $N_{\text{unkn}}^{\text{HFSS}} = 1{,}123{,}306$ unknowns and $T^{\text{HFSS}} = 152{,}674$ seconds of computational time, which is approximately 3.3 times slower than MoM-VIE computations.

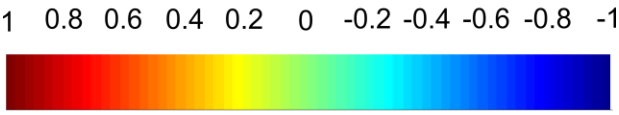

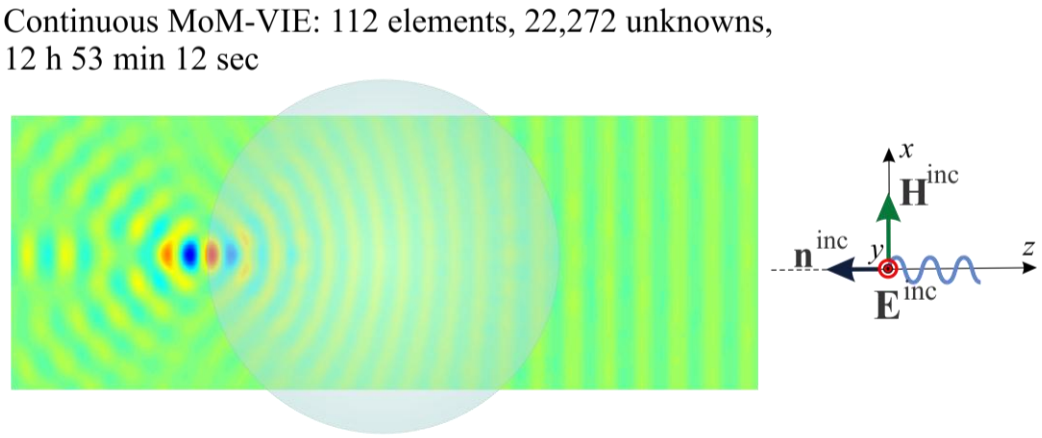

(a)

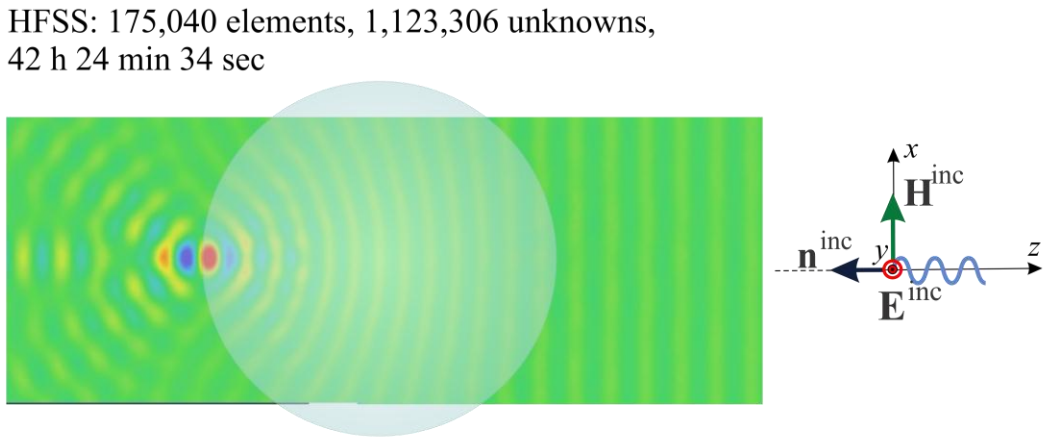

(b)

Fig. 17. Normalized real part of the *y*-component of the electric field *Ey* inside and outside of the Luneburg lens calculated by VIE-inhomogeneous (a) approach and HFSS (b) commercial software.

2.4 Summary

This section presented an application of a double-higher order VIE technique for the calculation of scattering from continuously inhomogeneous dielectric bodies. Special Lagrange-type generalized curved parametric hexahedra with variations of medium parameters were utilized for geometrical subdivision. This is the first implementation of continuously inhomogeneous tessellation elements in a double-higher VIE approach, which allow a permittivity throughout the element to be a function of spatial coordinates, $\varepsilon(\mathbf{r})$. The general expression for the VIE-MoM matrix element calculation was derived, while taking into account permittivity variation.

The method is verified by comparisons with a higher-order FEM technique [41][46] and the commercial EM software HFSS. The examples have demonstrated higher efficiency, and a considerable reduction in the number of unknowns when compared with both piecewise homogeneous VIE and general continuously inhomogeneous FEM techniques. The efficiency of the continuously inhomogeneous VIE analysis should be even more pronounced when compared with low-order VIE solutions. It should be noted that, in general, implementation of permittivity as a function of the position in each geometrical element becomes efficient when electrically large elements are utilized. Therefore, double-higher order discretization is more practical for application purposes.

3 GENERALIZED VOLUME/SURFACE INTEGRAL EQUATION METHOD OF MOMENTS TECHNIQUE

3.1 Introduction

As was previously mentioned, one of the most general approaches to the analysis of metallic and dielectric structures is the surface integral equation (SIE) approach [2],[17]. In this method, both electric and magnetic surface currents are introduced over boundary surfaces between homogeneous parts of the structure. Furthermore the surface integral equations, based on boundary conditions for both electric and magnetic field intensity vectors, are solved with current densities as unknowns. The main advantage of this method is its resilience in the modeling of high-contrast media and the ability to avoid discretizing the interior of the boundary surface (using volumetric elements), which can be very large. On the other hand, the SIE method is very inconvenient for dealing with inhomogeneous objects. In contrast VIE, which was described in sections 1 and 2, is a natural choice for simulating inhomogeneous dielectric objects. However, for high-contrast media it leads to larger computational errors and subsequently increases the number of unknowns [38]. Therefore, hybridization of these two techniques will result in an extremely efficient method, generalized volume-surface integral equation (VSIE), which takes advantage of the strengths of both approaches. The proposed technique results in an efficient solution for inhomogineities within high-contrast medium, while also creating the base for a diakoptic approach, similar to pure SIE-diakoptics [57]-[64], which will be discussed in detail in section 4.

3.2 Generalized Volume-Surface Integral Equation Formulation

In the generalized VSIE analysis, the electromagnetic system is subdivided into subsystems by virtue of the surface equivalence principle [1]. For the clarity of explanation, we consider a single domain v of permittivity ε_2 and permeability μ_2, bounded by a closed surface S, as depicted in Fig. 18(a), so two subsystems, v and its exterior (with medium parameters ε_1 and μ_1). According to this principle, the electric and magnetic fields $\mathbf{E}$ and $\mathbf{H}$ everywhere can be uniquely evaluated by knowing electric and magnetic tangential fields $\mathbf{E}_S$ and $\mathbf{H}_S$ at S.

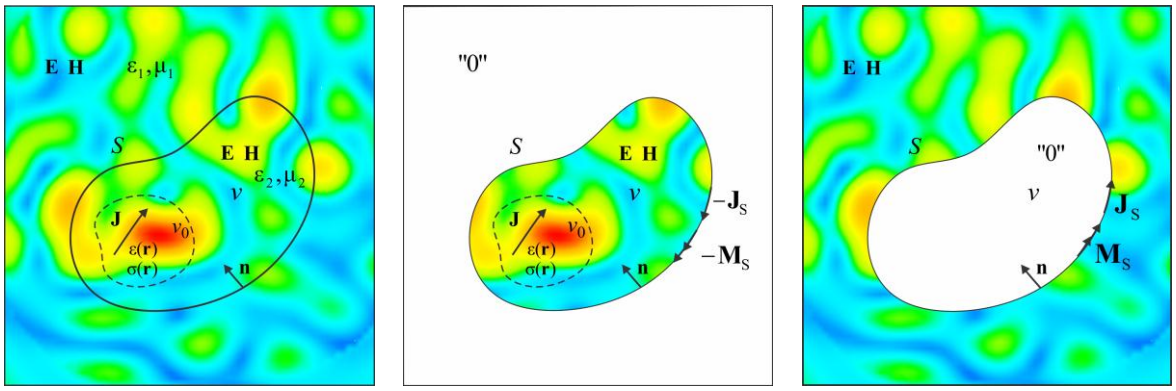

(a) (b) (c)

Fig. 18. Illustration of the surface and volume equivalence principles, as the theoretical foundation of the generalized VSIE approach to electromagnetic analysis: (a) original electromagnetic system, split into two parts (subsystems) by a closed surface S (diakoptic surface), on which equivalent surface currents are placed in order to radiate the actual fields, (b) equivalent interior problem, which includes an inhomogeneous dielectric body taken into account by the radiation of equivalent volume currents, and (c) equivalent exterior problem (with original fields outside and zero field inside S).

Without the loss of generality, let us assume that interior impressed volume electric currents of density $\mathbf{J}$ exist only in a domain v_0, which is a part of v. For example, these currents can represent an actual volume current distribution of a dielectric body located inside v. The fields

$\mathbf{E}$ and $\mathbf{H}$ can be obtained as being radiated by fictitious equivalent surface electric and magnetic currents whose densities are given by $\mathbf{J}_S = -\mathbf{n} \times \mathbf{H}_S$ and $\mathbf{M}_S = \mathbf{n} \times \mathbf{E}_S$, where $\mathbf{n}$ stands for a normal unit vector on S, directed toward the interior region, as shown in Fig. 18 (a). As a result of subtraction of the equivalent currents and their fields from the original problem, the fields $\mathbf{E}$ and $\mathbf{H}$ in v remain unchanged, while the fields in the exterior region are annihilated, Fig. 18 (b). The surface equivalence principle for the exterior region is established in the analogous way, Fig. 18(c).

Assume now that the domain v_0 in Fig. 18 (a) actually represents an arbitrarily shaped inhomogeneous dielectric body, with the permittivity ε and conductivity σ of the dielectric material being known functions of position, while the permeability at all points is μ_0. According to the volume equivalence principle [1], the dielectric inhomogeneity can be taken into account by the radiation of volumetric electric currents of density $\mathbf{J}$, which we can consider as the impressed sources when applying the surface equivalence principle, in Fig. 18. The constitutive (material) relationship for the total electric field at each point of the domain v_0 and boundary conditions for tangential components of total electric and magnetic field vectors on the surface S yield

$$\mathbf{E}(\mathbf{J}_S, \varepsilon_1, \mu_1)\big|_{\tan} + \mathbf{E}(\mathbf{J}_S, \varepsilon_2, \mu_2)\big|_{\tan} + \mathbf{E}(\mathbf{M}_S, \varepsilon_1, \mu_1)\big|_{\tan} + \mathbf{E}(\mathbf{M}_S, \varepsilon_2, \mu_2)\big|_{\tan} - \mathbf{E}(\mathbf{D}, \varepsilon_2, \mu_2)\big|_{\tan} = -\mathbf{E}_{\text{inc}}\big|_{\tan} \tag{26a}$$

$$\mathbf{H}(\mathbf{J}_S, \varepsilon_1, \mu_1)\big|_{\tan} + \mathbf{H}(\mathbf{J}_S, \varepsilon_2, \mu_2)\big|_{\tan} + \mathbf{H}(\mathbf{M}_S, \varepsilon_1, \mu_1)\big|_{\tan} + \mathbf{H}(\mathbf{M}_S, \varepsilon_2, \mu_2)\big|_{\tan} - \mathbf{H}(\mathbf{D}, \varepsilon_2, \mu_2)\big|_{\tan} = -\mathbf{H}_{\text{inc}}\big|_{\tan} \tag{26b}$$

$$\mathbf{E}(\mathbf{J}_S, \varepsilon_2, \mu_2) + \mathbf{E}(\mathbf{M}_S, \varepsilon_2, \mu_2) - \mathbf{E}(\mathbf{D}, \varepsilon_2, \mu_2) + \frac{\mathbf{D}}{\varepsilon_e} = 0 \tag{26c}$$

where $\mathbf{D}$ is the equivalent electric displacement vector and $\varepsilon_e = \varepsilon - \mathrm{j}\frac{\sigma}{\omega}$, is the equivalent complex permittivity of the material at that point, while $\mathbf{E}_{\mathrm{inc}}$ is an excitation electric field resulting from arbitrarily positioned sources outside of v. The vectors $\mathbf{J}$ and $\mathbf{D}$ are related to each other as $\mathbf{J} = \mathrm{j}\omega C\mathbf{D}$, $C = \frac{\varepsilon_e - \varepsilon_2}{\varepsilon_e} = \frac{\Delta\varepsilon - 1}{\Delta\varepsilon}$ is its dielectric contrast.

The scattered electric field from the boundary surface in the region of the complex permittivity ε and complex permeability μ is expressed in terms of the electric and magnetic current densities as follows:

$$\mathbf{E}(\mathbf{J}_S, \varepsilon, \mu) = -\mathrm{j}\omega\mathbf{A} - \nabla\varphi \qquad \mathbf{E}(\mathbf{M}_S, \varepsilon, \mu) = -\frac{1}{\varepsilon}\nabla \times \mathbf{F} \tag{27}$$

while the scattered magnetic field is obtained by

$$\mathbf{H}(\mathbf{M}_S, \varepsilon, \mu) = -\mathrm{j}\omega\mathbf{F} - \nabla U \qquad \mathbf{H}(\mathbf{J}_S, \varepsilon, \mu) = \frac{1}{\mu}\nabla \times \mathbf{A} \tag{28}$$

Scattered electric and magnetic fields due to the inhomogeneity within the medium are calculated as follows:

$$\mathbf{E}(\mathbf{D}, \varepsilon, \mu) = -\mathrm{j}\omega\mathbf{A}_v - \nabla\Phi \qquad \mathbf{H}(\mathbf{D}, \varepsilon, \mu) = \frac{1}{\mu}\nabla \times \mathbf{A}_v \tag{29}$$

$$\mathbf{A} = \mu\int_S \mathbf{J}_S g \mathrm{d}S \qquad \varphi = \frac{\mathrm{j}}{\omega\varepsilon}\int_S \nabla_S \cdot \mathbf{J}_S g \mathrm{d}S \tag{30}$$

$$\mathbf{F} = \varepsilon\int_S \mathbf{M}_S g \mathrm{d}S \qquad U = \frac{\mathrm{j}}{\omega\mu}\int_S \nabla_S \cdot \mathbf{M}_S g \mathrm{d}S \tag{31}$$

$$\mathbf{A}_v = \mu\int_V \mathrm{j}\omega C\mathbf{D} g \mathrm{d}V \qquad \Phi = \frac{\mathrm{j}}{\omega\varepsilon}\left[\int_V \nabla \cdot (\mathrm{j}\omega C\mathbf{D}) g \mathrm{d}V + \int_{S_d} \mathbf{n} \cdot (\mathrm{j}\omega C\mathbf{D}) g \mathrm{d}S\right] \tag{32}$$

In the above expressions $\mathbf{A}$, $\mathbf{F}$ and $\mathbf{A}_v$ are the magnetic and electric vector potentials, and φ, U and Φ are electric and magnetic scalar potentials, respectively. g represents the Green's function in (5) for the unbounded medium of parameters ε and μ.

Taking into account the integral expressions for the fields **E** and **H** in (27-29), (26) represents a set of coupled electric/magnetic field integral equations for $\mathbf{J}_S$, $\mathbf{M}_S$ and **D** as unknowns, which can be discretized and solved using the Method of Moments (MoM).

3.3 Generalized Galerkin Impedances for Double-Higher-Order Volume and Surface Elements

Assume that surfaces (metallic and dielectric) and inhomogeneous dielectric volumes in the system are approximated by a number of arbitrary surface and volume elements. Let us approximate the surface electric and magnetic current density vectors $\mathbf{J}_S$, $\mathbf{M}_S$ and equivalent electric displacement vector $\mathbf{D}$, over every element in the model by convenient set of basis functions with unknown complex current-distribution coefficients. In order to determine these coefficients, the EFIE/MFIE system in (26) is tested by means of the Galerkin method, i.e., using the same functions used for current expansion. The nine types of generalized Galerkin impedances (the system matrix elements) corresponding to the nine combinations of electric-, magnetic-current and electric displacement vector testing functions $\mathbf{J}_{Sm}$, $\mathbf{M}_{Sm}$ and $\mathbf{D}_m$ defined on the *m*-th surface element (S_m) or inside *m*-th volume element (V_m) and basis functions $\mathbf{J}_{Sn}$, $\mathbf{M}_{Sn}$ and $\mathbf{D}_n$ defined for the *n*-th element in the model are obtained by following testing procedure. Testing (26a) with $\mathbf{J}_{Sm}$ yelds

$$\int_{S_m} \mathbf{J}_{Sm} \cdot \mathbf{E}(\mathbf{J}_{Sn}, \varepsilon_1, \mu_1)\, dS_m + \int_{S_m} \mathbf{J}_{Sm} \cdot \mathbf{E}(\mathbf{J}_{Sn}, \varepsilon_2, \mu_2)\, dS_m +$$
$$\int_{S_m} \mathbf{J}_{Sm} \cdot \mathbf{E}(\mathbf{M}_{Sn}, \varepsilon_1, \mu_1)\, dS_m + \int_{S_m} \mathbf{J}_{Sm} \cdot \mathbf{E}(\mathbf{M}_{Sn}, \varepsilon_2, \mu_2)\, dS_m \qquad (33)$$
$$- \int_{S_m} \mathbf{J}_{Sm} \cdot \mathbf{E}(\mathbf{D}_n, \varepsilon_2, \mu_2)\, dS_m = -\int_{S_m} \mathbf{J}_{Sm} \cdot \mathbf{E}_{\text{inc}}\, dS_m$$

Testing (26b) with $\mathbf{M}_{Sm}$ yelds

$$\int_{S_m} \mathbf{M}_{Sm} \cdot \mathbf{H}(\mathbf{J}_{Sn}, \varepsilon_1, \mu_1)\, dS_m + \int_{S_m} \mathbf{M}_{Sm} \cdot \mathbf{H}(\mathbf{J}_{Sn}, \varepsilon_2, \mu_2)\, dS_m +$$
$$\int_{S_m} \mathbf{M}_{Sm} \cdot \mathbf{H}(\mathbf{M}_{Sn}, \varepsilon_1, \mu_1)\, dS_m + \int_{S_m} \mathbf{M}_{Sm} \cdot \mathbf{H}(\mathbf{M}_{Sn}, \varepsilon_2, \mu_2)\, dS_m \qquad (34)$$
$$- \int_{S_m} \mathbf{M}_{Sm} \cdot \mathbf{H}(\mathbf{D}_n, \varepsilon_2, \mu_2)\, dS_m = -\int_{S_m} \mathbf{M}_{Sm} \cdot \mathbf{H}_{\text{inc}}\, dS_m$$

And finally testing (26c) with $\mathbf{D}_m$ yelds

$$\int_{V_m} \mathbf{D}_m \cdot \mathbf{E}(\mathbf{J}_{Sn}, \varepsilon_2, \mu_2)\, dV_m + \int_{V_m} \mathbf{D}_m \cdot \mathbf{E}(\mathbf{M}_{Sn}, \varepsilon_2, \mu_2)\, dV_m -$$
$$\int_{V_m} \mathbf{D}_m \cdot \mathbf{E}(\mathbf{D}_n, \varepsilon_2, \mu_2)\, dV_m + \int_{V_m} \mathbf{D}_m \cdot \frac{\mathbf{D}_n}{\varepsilon_e}\, dV_m = 0 \qquad (35)$$

,

which results in a system of linear equations represented in matrix form as follows:

$$\begin{bmatrix} Z_{\mathbf{J}_S\mathbf{J}_S} & Z_{\mathbf{J}_S\mathbf{M}_S} & Z_{\mathbf{J}_S\mathbf{D}} \\ Z_{\mathbf{M}_S\mathbf{J}_S} & Z_{\mathbf{M}_S\mathbf{M}_S} & Z_{\mathbf{M}_S\mathbf{D}} \\ Z_{\mathbf{D}\mathbf{J}_S} & Z_{\mathbf{D}\mathbf{M}_S} & Z_{\mathbf{D}\mathbf{D}} \end{bmatrix} \begin{bmatrix} \mathbf{J}_S \\ \mathbf{M}_S \\ \mathbf{D} \end{bmatrix} = \begin{bmatrix} V_{\mathbf{E}} \\ V_{\mathbf{H}} \\ 0 \end{bmatrix} \qquad (36)$$

In the above $Z_{\mathbf{J}_S\mathbf{J}_S}$, $Z_{\mathbf{J}_S\mathbf{M}_S}$, $Z_{\mathbf{M}_S\mathbf{J}_S}$, $Z_{\mathbf{M}_S\mathbf{M}_S}$ are terms being calculated by pure SIE [17] and $Z_{\mathbf{DD}}$ by pure VIE (section 1) codes, while the other four terms are results of a hybrid VIE/SIE or generalized VSIE. These terms are calculated as follows:

$$Z_{\mathbf{J}_S\mathbf{D}} = -\int_{S_m} \mathbf{J}_{Sm} \cdot \mathbf{E}\left(\mathbf{D}_n, \varepsilon_2, \mu_2\right) \mathrm{d}S_m = -\omega^2 \mu_2 \int_{S_m} \mathbf{J}_{Sm} \cdot \int_{V_n} C_n \mathbf{D}_n g \mathrm{d}V_n \, \mathrm{d}S_m +$$
$$\frac{1}{\varepsilon_2} \int_{S_m} \nabla \cdot \mathbf{J}_{Sm} \int_{V_n} \nabla \cdot \left(C_n \mathbf{D}_n\right) g \mathrm{d}V_n \, \mathrm{d}S_m + \frac{1}{\varepsilon_2} \int_{S_m} \nabla \cdot \mathbf{J}_{Sm} \int_{S_n} C_n \mathbf{D}_n \cdot \mathbf{n} g \, \mathrm{d}S_n \mathrm{d}S_m \tag{37}$$

$$Z_{\mathbf{M}_S\mathbf{D}} = -\int_{S_m} \mathbf{M}_{Sm} \cdot \mathbf{H}\left(\mathbf{D}_n, \varepsilon_2, \mu_2\right) \mathrm{d}S_m = -\mathrm{j}\omega \int_{S_m} \mathbf{M}_{Sm} \cdot \nabla \times \int_{V_n} C_n \mathbf{D}_n g \, \mathrm{d}V_n \mathrm{d}S_m =$$
$$-\mathrm{j}\omega \int_{S_m V_n} \left(\mathbf{D}_n \times \mathbf{M}_{Sm}\right) \cdot \nabla g C_n \, \mathrm{d}V_n \mathrm{d}S_m \tag{38}$$

$$Z_{\mathbf{D}\mathbf{J}_S} = \int_{V_m} \mathbf{D}_m \cdot \mathbf{E}\left(\mathbf{J}_{Sn}, \varepsilon_2, \mu_2\right) \mathrm{d}V_m = -\mathrm{j}\omega \mu_2 \int_{V_m} \mathbf{D}_m \cdot \int_{S_n} \mathbf{J}_{Sn} g \, \mathrm{d}S_n \mathrm{d}V_m -$$
$$\frac{\mathrm{j}}{\omega \varepsilon_2} \int_{S_m} \mathbf{D}_m \int_{S_n} \nabla_S \cdot \mathbf{J}_{Sn} g \, \mathrm{d}S_n \mathrm{d}S_m + \frac{\mathrm{j}}{\omega \varepsilon_2} \int_{V_m} \nabla \cdot \mathbf{D}_m \int_{S_n} \nabla_S \cdot \mathbf{J}_{Sn} g \, \mathrm{d}S_n \mathrm{d}V_m \tag{39}$$

$$Z_{\mathbf{D}\mathbf{M}_S} = \int_{V_m} \mathbf{D}_m \cdot \mathbf{E}\left(\mathbf{M}_{Sn}, \varepsilon_2, \mu_2\right) \mathrm{d}V_m = -\int_{V_m} \mathbf{D}_m \cdot \nabla \times \int_{S_n} \mathbf{M}_{Sn} g \, \mathrm{d}S_n \mathrm{d}V_m$$
$$= -\int_{V_m S_n} \left(\mathbf{M}_{Sn} \times \mathbf{D}_m\right) \cdot \nabla g \, \mathrm{d}S_n \mathrm{d}V_m \tag{40}$$

Because PEC plates with an electric current distribution are already implemented in the developed VSIE method presented in section 1, integrals of the type $Z_{\mathbf{J}_S\mathbf{D}}$ and $Z_{\mathbf{D}\mathbf{J}_S}$ can be calculated using the existing code. In order to calculate the terms $Z_{\mathbf{M}_S\mathbf{D}}$ and $Z_{\mathbf{D}\mathbf{M}_S}$, the integrals involving the gradient of the Green's function have to be evaluated. The expression for the gradient of Green's function for $\mathbf{r}'$ and $\mathbf{r}$ being a source and field point, respectively, is

$$\nabla g = \frac{1 + \mathrm{j}\beta R}{4\pi R^3} e^{-\mathrm{j}\beta R}\left[\mathbf{r}' - \mathbf{r}\right] = G\left[\mathbf{r}' - \mathbf{r}\right] \qquad \beta = \omega\sqrt{\varepsilon_2 \mu_2} \tag{41}$$

To illustrate the procedure for computing impedances in (38), (40), analogously to section 1.4, only the *u*-components of the basis and testing functions are considered. Furthermore, without loss of generality, we consider the functions in the following simplified form

$$\mathbf{f}^{\mathrm{VIE}} = \mathbf{f}_{upst} = \frac{u^p v^s w^t}{\mathfrak{I}} \frac{\partial \mathbf{r}}{\partial u} \qquad \mathbf{f}^{\mathrm{SIE}} = \mathbf{f}_{ups} = \frac{u^p v^s}{\mathfrak{I}} \frac{\partial \mathbf{r}}{\partial u} \tag{42}$$

The generalized Galerkin impedances corresponding to the complete divergence-conforming basis functions in (11) and in [17] can be obtained as a linear combination of those corresponding to the simplified, three- and two-dimensional power functions in (42). Therefore,

$$\mathbf{D}_\xi = \mathbf{D}_{u_\xi} = u_\xi^{p_\xi} v_\xi^{s_\xi} w_\xi^{t_\xi} \sum_{i_\xi=1}^{N_\xi} \sum_{j_\xi=0}^{N_\xi} \sum_{k_\xi=0}^{N_\xi} i_\xi u_\xi^{i_\xi - 1} v_\xi^{j_\xi} w_\xi^{k_\xi} \mathbf{r}_{i_\xi j_\xi k_\xi} \tag{45}$$

$$\mathbf{M}_{\mathrm{S}\eta} = \mathbf{M}_{u_\eta} = u_\eta^{p_\eta} v_\eta^{s_\eta} \sum_{i_\eta=1}^{N_\eta} \sum_{j_\eta=0}^{N_\eta} i_\eta u_\eta^{i_\eta - 1} v_\eta^{j_\eta} \mathbf{r}_{i_\eta j_\eta} \tag{46}$$

$$\mathbf{r}_\xi = \sum_{i_\xi=1}^{N_\xi} \sum_{j_\xi=0}^{N_\xi} \sum_{k_\xi=0}^{N_\xi} u_\xi^{i_\xi} v_\xi^{j_\xi} w_\xi^{k_\xi} \mathbf{r}_{i_\xi j_\xi k_\xi} \qquad \mathbf{r}_\eta = \sum_{i_\eta=1}^{N_\eta} \sum_{j_\eta=0}^{N_\eta} u_\eta^{i_\eta} v_\eta^{j_\eta} \mathbf{r}_{i_\eta j_\eta} \tag{47}$$

where ξ and η can be *m* or *n*, depending on which matrix element is being calculated (*m* is always an index of a testing function, *n* – for the basis). Therefore, the matrix elements of (38) can be written as follows

$$\begin{aligned}
&Z_{\mathbf{M}_{\mathrm{S}}\mathbf{D}} = -\mathrm{j}\omega \int_{S_m} \int_{V_n} \left(\mathbf{D}_n \times \mathbf{M}_{\mathrm{S}m}\right) \cdot \nabla g C_n \mathrm{d}V \mathrm{d}S = \\
&-\mathrm{j}\omega \int_{S_m} \int_{V_n} \left(u_n^{p_n} v_n^{s_n} w_n^{t_n} \sum_{i_n=1}^{N_n} \sum_{j_n=0}^{N_n} \sum_{k_n=0}^{N_n} i_n u_n^{i_n - 1} v_n^{j_n} w_n^{k_n} \mathbf{r}_{i_n j_n k_n} \times u_m^{p_m} v_m^{s_m} \sum_{i_m=1}^{N_m} \sum_{j_m=0}^{N_m} i_m u_m^{i_m - 1} v_m^{j_m} \mathbf{r}_{i_m j_m} \right) \cdot \\
&\left[\sum_{i'_n=1}^{N_n} \sum_{j'_n=0}^{N_n} \sum_{k'_n=0}^{N_n} u_n^{i'_n} v_n^{j'_n} w_n^{k'_n} \mathbf{r}_{i'_n j'_n k'_n} - \sum_{i'_m=1}^{N_m} \sum_{j'_m=0}^{N_m} u_m^{i'_m} v_m^{j'_m} \mathbf{r}_{i'_m j'_m} \right] G C_n \mathrm{d}u_n \mathrm{d}v_n \mathrm{d}w_n \mathrm{d}u_m \mathrm{d}v_m = \\
&= -\mathrm{j}\omega \sum_{i_n=1}^{N_n} \sum_{j_n=0}^{N_n} \sum_{k_n=0}^{N_n} \sum_{i_m=1}^{N_m} \sum_{j_m=0}^{N_m} \sum_{i'_n=0}^{N_n} \sum_{j'_n=0}^{N_n} \sum_{k'_n=0}^{N_n} i_n i_m \left(\mathbf{r}_{i_n j_n k_n} \times \mathbf{r}_{i_m j_m}\right) \cdot \mathbf{r}_{i'_n j'_n k'_n} \cdot
\end{aligned} \tag{48}$$

$$\int\limits_{S_m} u_m^{p_m+i_m-1} v_m^{s_m+j_m} \int\limits_{V_n} u_n^{p_n+i_n+i'_n-1} v_n^{s_n+j_n+j'_n} w_n^{t_n+k_n+k'_n} GC_n \mathrm{d}u_n \mathrm{d}v_n \mathrm{d}w_n \mathrm{d}u_m \mathrm{d}v_m +$$

$$\mathrm{j}\omega \sum_{i_n=1}^{N_n} \sum_{j_n=0}^{N_n} \sum_{k_n=0}^{N_n} \sum_{i_m=1}^{N_m} \sum_{j_m=0}^{N_m} \sum_{i'_m=0}^{N_m} \sum_{j'_m=0}^{N_m} i_n i_m \left(\mathbf{r}_{i_n j_n k_n} \times \mathbf{r}_{i_m j_m} \right) \cdot \mathbf{r}_{i'_m j'_m} \cdot$$

$$\int\limits_{S_m} u_m^{p_m+i_m+i'_m-1} v_m^{s_m+j_m+j'_m} \int\limits_{V_n} u_n^{p_n+i_n-1} v_n^{s_n+j_n} w_n^{t_n+k_n} GC_n \mathrm{d}u_n \mathrm{d}v_n \mathrm{d}w_n \mathrm{d}u_m \mathrm{d}v_m$$

Analogous to $Z_{\mathbf{M}_\mathrm{S}\mathbf{D}}$ the following expression for each $Z_{\mathbf{D}\mathbf{M}_\mathrm{s}}$ matrix element is obtained

$$Z_{\mathbf{D}\mathbf{M}_\mathrm{S}} = -\int\limits_{V_m} \int\limits_{S_n} \left(\mathbf{M}_{\mathrm{S}n} \times \mathbf{D}_m \right) \cdot \nabla g \mathrm{d}S \mathrm{d}V =$$

$$-\int\limits_{V_m} \int\limits_{S_n} \left(u_n^{p_n} v_n^{s_n} \sum_{i_n=1}^{N_n} \sum_{j_n=0}^{N_n} i_n u_n^{i_n-1} v_n^{j_n} \mathbf{r}_{i_n j_n} \times u_m^{p_m} v_m^{s_m} w_m^{t_m} \sum_{i_m=1}^{N_m} \sum_{j_m=0}^{N_m} \sum_{k_m=0}^{N_m} i_m u_m^{i_m-1} v_m^{j_m} w_m^{k_m} \mathbf{r}_{i_m j_m k_m} \right) \cdot$$

$$\left[\sum_{i'_n=1}^{N_n} \sum_{j'_n=0}^{N_n} u_n^{i'_n} v_n^{j'_n} \mathbf{r}_{i'_n j'_n} - \sum_{i'_m=0}^{N_m} \sum_{j'_m=0}^{N_m} \sum_{k'_m=0}^{N_m} u_m^{i'_m} v_m^{j'_m} w_m^{k'_m} \mathbf{r}_{i'_m j'_m k'_m} \right] G \mathrm{d}u_n \mathrm{d}v_n \mathrm{d}u_m \mathrm{d}v_m \mathrm{d}w_m =$$

$$-\sum_{i_n=1}^{N_n} \sum_{j_n=0}^{N_n} \sum_{i_m=1}^{N_m} \sum_{j_m=0}^{N_m} \sum_{k_m=0}^{N_m} \sum_{i'_n=0}^{N_n} \sum_{j'_n=0}^{N_n} i_n i_m \left(\mathbf{r}_{i_n j_n} \times \mathbf{r}_{i_m j_m k_m} \right) \cdot \mathbf{r}_{i'_n j'_n} \cdot \qquad (49)$$

$$\int\limits_{V_m} u_m^{p_m+i_m-1} v_m^{s_m+j_m} w_m^{t_m+k_m} \int\limits_{S_n} u_n^{p_n+i_n+i'_n-1} v_n^{s_n+j_n+j'_n} G \mathrm{d}u_n \mathrm{d}v_n \mathrm{d}u_m \mathrm{d}v_m \mathrm{d}w_m +$$

$$\sum_{i_n=1}^{N_n} \sum_{j_n=0}^{N_n} \sum_{i_m=1}^{N_m} \sum_{j_m=0}^{N_m} \sum_{k_m=0}^{N_m} \sum_{i'_m=0}^{N_m} \sum_{j'_m=0}^{N_m} \sum_{k'_m=0}^{N_m} i_n i_m \left(\mathbf{r}_{i_n j_n} \times \mathbf{r}_{i_m j_m k_m} \right) \cdot \mathbf{r}_{i'_m j'_m k'_m} \cdot$$

$$\int\limits_{V_m} u_m^{p_m+i_m+i'_m-1} v_m^{s_m+j_m+j'_m} w_m^{t_m+k_m+k'_m} \int\limits_{S_n} u_n^{p_n+i_n-1} v_n^{s_n+j_n} G \mathrm{d}u_n \mathrm{d}v_n \mathrm{d}u_m \mathrm{d}v_m \mathrm{d}w_m$$

The above derivations were performed without employing metallic surfaces. However the technique presented here does not lose its generality, because PEC surfaces are represented the same way as equivalent dielectric surfaces, except for the magnetic current distribution $\mathbf{M}_\mathrm{S} = 0$.

3.4 Numerical Results and Discussion

3.4.1 Spherical Inclusion Embedded in Sphere

As an example of the generalized VSIE application, consider the scattering of a *z*-directed plane wave from a dielectric sphere of radius $r = 0.1\lambda_0$ and permittivity $\varepsilon_r = 20$, embedded in a sphere of radius $r = 0.5\lambda_0$ and permittivity $\varepsilon_r = 10$ (λ_0 is a free-space wavelength) [38]. This object can be treated as a homogeneous sphere of permittivity $\varepsilon_r = 10$ and the spherical inhomogeneity inside it of perturbation factor $\Delta\varepsilon = 2$.

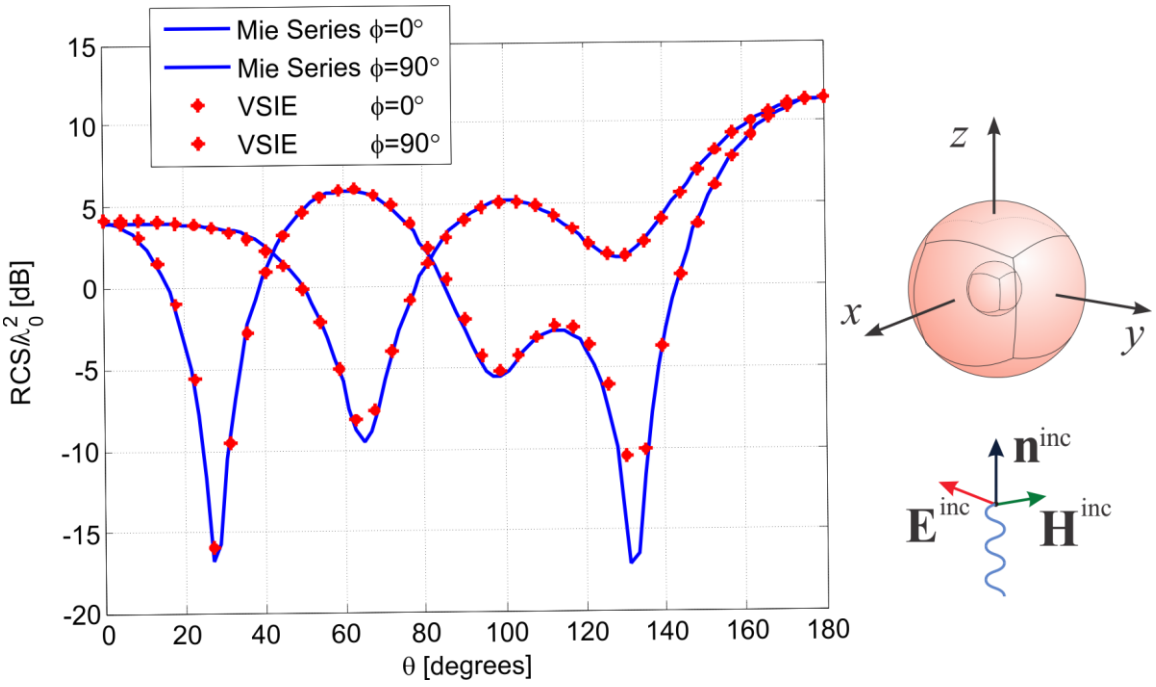

Fig. 19. Scattering from the dielectric sphere with spherical inclusion

The embedded sphere was modeled by one hexahedral element of the second order with an order of equivalent electric displacement vector approximation of $N_u = N_v = N_w = 3$, while the outer layer is constructed by 24 second order quadrilaterals with current approximations

$N_u = N_v = 5$, resulting in a total of $N^{\text{VSIE}} = 2508$ unknowns. In Fig. 19 the results for the radar cross-section (RCS) of the sphere in two different planes, calculated by generalized VSIE approach, is compared to an analytical solution in the form of Mie's series.

3.4.2 Smoothly Varying Inhomogeneity

In the second example, we consider the scattering from a dielectric sphere of radius $a = \lambda/3$ having a material profile that varies radially as $\varepsilon_r(r) = 10 - 15r$ where r is defined in wavelengths (similar to example in [38]). To demonstrate the VSIE's capability to model smoothly varying material profiles, we select a fictitious background medium of $\varepsilon_b = 5$, for which $\varepsilon_\Delta = 2 - 3r$. The continuously inhomogeneous sphere was modeled by 7 hexahedral elements of the second order (similar to example in section 2.3.2) with an order of equivalent electric displacement vector approximation of $N_u = N_v = N_w = 4$, while the surface layer is constructed by 6 second order quadrilaterals with current approximations $N_u = N_v = 6$, resulting in a total of $N^{\text{VSIE}} = 2448$ unknowns and $T^{\text{VSIE}} = 394$ seconds of computational time. In Fig. 20 the results for the radar cross-section (RCS) of the sphere in two different planes, calculated by generalized VSIE approach, are validated by the piecewise-homogeneous VIE model constructed of 7 concentric spheres of constant permittivity. Pure VIE solution required $N^{\text{VIE}} = 7776$ unknowns and $T^{\text{VIE}} = 2391$ seconds of computational time.

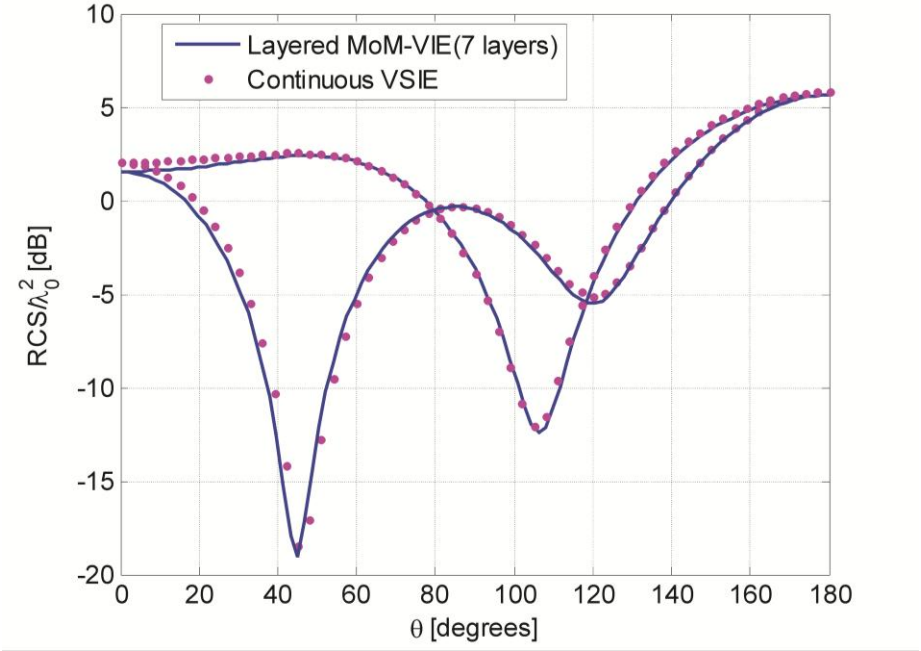

Fig. 20. Scattering from the continuously inhomogeneous sphere

3.5 Summary

An efficient higher-order approach was developed for analysis of high contrast dielectric scatterers possessing inhomogeneity within the volume. As it is well known, the volume integral equation method (VIE) is not very efficient to analyze high-contrast dielectric medium, due to the requirement of very fine volumetric discretization of the structure. However, surface integral equation has been shown to be quite efficient in this sense, while suffering from the difficulties of modeling inhomogeneous dielectric objects. This section presented a subdivision of the entire system by SIE into domains of different constant permittivity, employing corresponding Green's functions for each domain, all while modeling the inhomogeneity within each of them with VIE. The inhomogeneity within each domain was defined in terms of the perturbation factor in relation to the domain permittivity (background permittivity).

4 VOLUME/SURFACE INTEGRAL EQUATION BASED DIAKOPTIC DOMAIN DECOMPOSITION METHOD FOR 3-D ELECTROMAGNETIC SCATTERING ANALYSIS

4.1 Introduction

This section of the thesis proposes the diakoptic approach to electromagnetic modeling and computation [57]-[64] as one possible strategy aimed at extending the practical applicability of both SIE-MoM and VIE-MoM methods over their intrinsic numerical limits and considerably enhancing their efficiency in real-world simulations. The diakoptics provides a general and efficient way to break an electrically large and complex electromagnetic problem into smaller and simpler ones, i.e., to split the original electromagnetic system into a number of non-overlapping subsystems of arbitrary shapes. Then each one of the subsystems can be analyzed independently. The solution of the original problem can then be found as a linear combination of solutions of component problems, using the explicit linear relations between coefficients in expansions of equivalent electric and magnetic surface currents (or other sources) on boundary surfaces of the subsystems. For the best overall efficiency and accuracy of numerical solutions to problems that contain subdomains of a different "nature" (some homogeneous with metallic parts, some considerably inhomogeneous, with different types of excitations, etc.), some diakoptic subsystems are analyzed by the SIE-MoM [2], [17] and some via the VIE-MoM [30]-[33] methods respectively. With the diakoptic approach, drastic enhancements of computation efficiency, measured in computing time, are possible for large and complex problems as compared to conventional MoM-VIE and MoM-SIE approaches, that implement the same type of discretization.

The first diakoptic approach for electromagnetic systems in application to circuit theory was formulated half a century ago by Gabriel Kron [50], for which reason the same name has been adopted. The term "diakoptics" comes from Greek words " διαα" (dia), which means "in-between," and "κόπτω" (kopto), meaning "cut" or "split," so diakoptics stands for "cutting in between". The similarity of the proposed approach with the original diakoptic approach applied to circuit theory is that parts of the original problem are represented by linear relations in matrix form. However, our diakoptic analysis is based on the surface and volume equivalence principles and operates with coefficients of expansions of surface/volumetric electric and surface magnetic currents.

4.2 Theoretical Background

Consider a dielectric object of permittivity ε_e, situated in free space and exited by an incident field. According to the surface equivalence principle, the entire system can be broken into subdomains as in section 3, each representing one of the dielectric regions in the system and $\varepsilon_1 = \varepsilon_2 = \varepsilon_0$, $\mu_1 = \mu_2 = \mu_0$. The scattered electric and magnetic fields, **E** and **H**, in each subdomain can be expressed in terms of the equivalent surface electric and magnetic currents, of density $\mathbf{J}_e$ and $\mathbf{M}_e$, placed on the boundary surface between subdomains (diakoptic surface), and volumetric current distribution **J** within the object. The boundary conditions for the tangential components of the total electric and magnetic field vectors on the surface, as in (26), and the appropriate testing procedure result in a system of matrix equations similar to (36):

$$
\begin{array}{c}
 \\
N_{\mathrm{e}} \\
N \\
N_{\mathrm{e}}
\end{array}
\begin{array}{c}
\begin{array}{ccccc} N_{\mathrm{e}} & N & N_{\mathrm{e}} & 1 & 1 \\ \leftrightarrow & \leftrightarrow & \leftrightarrow & \leftrightarrow & \leftrightarrow \end{array} \\
\updownarrow \begin{bmatrix} \mathbf{Z}_1 & \mathbf{Z}_2 & \mathbf{Z}_3 \\ \mathbf{Z}_4 & \mathbf{Z}_5 & \mathbf{Z}_6 \\ \mathbf{Z}_7 & \mathbf{Z}_8 & \mathbf{Z}_9 \end{bmatrix} \begin{bmatrix} \mathbf{j}_{\mathrm{e}} \\ \mathbf{d} \\ \mathbf{m}_{\mathrm{e}} \end{bmatrix} = \begin{bmatrix} \mathbf{v}_1 \\ \mathbf{v}_2 \\ \mathbf{v}_3 \end{bmatrix}
\end{array}
\tag{50}
$$

where $[\mathbf{j}_{\mathrm{e}}]$, $[\mathbf{m}_{\mathrm{e}}]$, and $[\mathbf{d}]$ are column-matrices of unknown coefficients for the approximation of $\mathbf{J}_{\mathrm{e}}$, $\mathbf{M}_{\mathrm{e}}$, and $\mathbf{D} = \mathrm{j}\omega C\mathbf{J}$, respectively, and $[\mathbf{v}_k]$, $k = 1,2,3$, constitute the excitation column-matrix. The first N_{e} equations (matrix rows) in (50) are obtained by discretizing the electric-field boundary condition (26a), while the remaining $N_{\mathrm{e}} + N$ equations (rows) correspond to the magnetic-field boundary condition discretization (26b) and the constitutive relation for the inhomogeomeous dielectric domain (26c).

A combined field integral equation (CFIE) formulation for the diakoptic surface can be obtained by multiplying the first N_{e} equations in (50) by α, and the last N_{e} equations by β. Summing the new equations and moving all the terms associated with $[\mathbf{m}_{\mathrm{e}}]$ to the right-hand side of the matrix equation results in

$$
\begin{bmatrix} \alpha\mathbf{Z}_1 + \beta\mathbf{Z}_7 & \alpha\mathbf{Z}_2 + \beta\mathbf{Z}_8 \\ \mathbf{Z}_4 & \mathbf{Z}_5 \end{bmatrix} \begin{bmatrix} \mathbf{j}_{\mathrm{e}} \\ \mathbf{d} \end{bmatrix} = -\begin{bmatrix} \alpha\mathbf{Z}_3 + \beta\mathbf{Z}_9 \\ \mathbf{Z}_6 \end{bmatrix} [\mathbf{m}_{\mathrm{e}}] + \begin{bmatrix} \alpha\mathbf{v}_1 + \beta\mathbf{v}_3 \\ \mathbf{v}_2 \end{bmatrix} \tag{51}
$$

The CFIE formulation was used because it does not introduce numerical instabilities at resonant frequencies of the diakoptic surface. Note that the matrix equation (50) cannot be solved without further information about the electromagnetic field outside the diakoptic subsystem. However, the mutual relations between $[\mathbf{j}_{\mathrm{e}}]$, $[\mathbf{m}_{\mathrm{e}}]$, and $[\mathbf{d}]$ given in (51), are valid for any field outside the subsystem.

Inverting the system matrix in (51), the following matrix linear relation results in

$$\begin{bmatrix}\mathbf{j}_{\mathrm{e}}\\ \mathbf{d}\end{bmatrix}=\begin{bmatrix}\mathbf{Y}\\ \mathbf{C}\end{bmatrix}\left[\mathbf{m}_{\mathrm{e}}\right]+\begin{bmatrix}\mathbf{j}_{\mathrm{e}0}\\ \mathbf{d}_0\end{bmatrix}, \tag{52}$$

where

$$\begin{bmatrix}\mathbf{Y}\\ \mathbf{C}\end{bmatrix}=-\begin{bmatrix}\alpha\mathbf{Z}_1+\beta\mathbf{Z}_7 & \alpha\mathbf{Z}_2+\beta\mathbf{Z}_8\\ \mathbf{Z}_4 & \mathbf{Z}_5\end{bmatrix}^{-1}\times\begin{bmatrix}\alpha\mathbf{Z}_3+\beta\mathbf{Z}_9\\ \mathbf{Z}_6\end{bmatrix}, \tag{53}$$

$$\begin{bmatrix}\mathbf{j}_{\mathrm{e}0}\\ \mathbf{d}_0\end{bmatrix}=\begin{bmatrix}\alpha\mathbf{Z}_1+\beta\mathbf{Z}_7 & \alpha\mathbf{Z}_2+\beta\mathbf{Z}_8\\ \mathbf{Z}_4 & \mathbf{Z}_5\end{bmatrix}^{-1}\times\begin{bmatrix}\alpha\mathbf{v}_1+\beta\mathbf{v}_3\\ \mathbf{v}_2\end{bmatrix}. \tag{54}$$

Therefore, based on (52), for each subdomain is obtained a set of linear relations between diakoptic current coefficients in each subdomain in the following matrix form:

$$\left[\mathbf{j}_{ei}\right]=\left[\mathbf{Y}_i\right]\left[\mathbf{m}_{ei}\right]+\left[\mathbf{j}_{ei}\right]_0 \quad i=1,2 \tag{55}$$

where $\left[\mathbf{Y}_i\right]$ is the diakoptic $N_{\mathrm{e}}\times N_{\mathrm{e}}$ matrix of the subsystem and $\left[\mathbf{j}_{ei}\right]_0$ is the $N_{\mathrm{e}}\times 1$ column-matrix containing coefficients of $\mathbf{J}_{\mathrm{e}}$, which represent the excitation in the subsystem. In order to numerically calculate these matrices, consider the coefficients $\left[\mathbf{m}_{\mathrm{e}}\right]$ as excitation and coefficients $\left[\mathbf{j}_{\mathrm{e}}\right]$ as the response – in a linear subsystem. In particular, the matrix $\left[\mathbf{Y}_i\right]$ is obtained by assuming that all the excitations in the subsystem are turned off and the subsystem is excited with one unity-valued coefficient of $\left[\mathbf{m}_{ei}\right]$.

In order to obtain the solution of the original electromagnetic problem, one needs to relate the diakoptic coefficients of equivalent electric and magnetic surface currents on boundaries between individual subsystems. At a diakoptic surface between adjacent subsystems, there are

$$\left[\mathbf{j}_{\mathrm{e}1}\right]=\left[\mathbf{j}_{\mathrm{e}2}\right]=\left[\mathbf{j}_{\mathrm{e}}\right] \text{ and } \left[\mathbf{m}_{\mathrm{e}1}\right]=\left[\mathbf{m}_{\mathrm{e}2}\right]=\left[\mathbf{m}_{\mathrm{e}}\right] \tag{56}$$

where equivalent sources are with opposite signs (based on the equivalence theorem), and the directions of normal unit vectors are opposite for the two (neighboring) subsystems. Combining (55) and (56), the following diakoptic matrix system is obtained:

$$([\mathbf{Y}_1]-[\mathbf{Y}_2])[\mathbf{m}_e] = -[\mathbf{j}_{e1}]_0 + [\mathbf{j}_{e2}]_0 \tag{57}$$

the solution of which is $[\mathbf{m}_e]$. Analogously to (55), linear relations can be established between $[\mathbf{j}_e]$ and $[\mathbf{d}]$ coefficients as

$$[\mathbf{d}_i] = [\mathrm{C}_i][\mathbf{m}_{ei}] + [\mathbf{j}_{ei}]_0 \; i = 1,2 \tag{58}$$

Once $[\mathbf{m}_e]$ is found, $[\mathbf{j}_e]$ and $[\mathbf{d}]$ can be calculated in a straightforward fashion, based on (55) and (58).

4.3 Numerical Results and Discussion

4.3.1 Array of Homogeneous Dielectric Cubical Scatterers

As the first example of the application and validation of the VIE-SIE-diakoptics approach, consider an 8×8 array of homogeneous lossless dielectric cubes of edge lengths $a = \lambda_0/6$, with λ_0 being the free-space wavelength, and relative permittivity $\varepsilon_r = 2.25$, excited by a uniform plane wave from the direction defined by $\theta_{inc} = 90°$ and $\phi_{inc} = 0^\circ$, as shown in Fig. 21. The surface-to-surface distance between neighboring cubes is $d = \lambda_0/6$, in both *x*- and *y*-directions. Each cubical diakoptic subsystem is modeled by a single VIE element with orders $K_u = K_v = K_w = 1$ and $N_u = N_v = N_w = 3$, with a diakoptic cubical surface constructed from six SIE patches with $K_u = K_v = 1$ and $N_u = N_v = 2$.

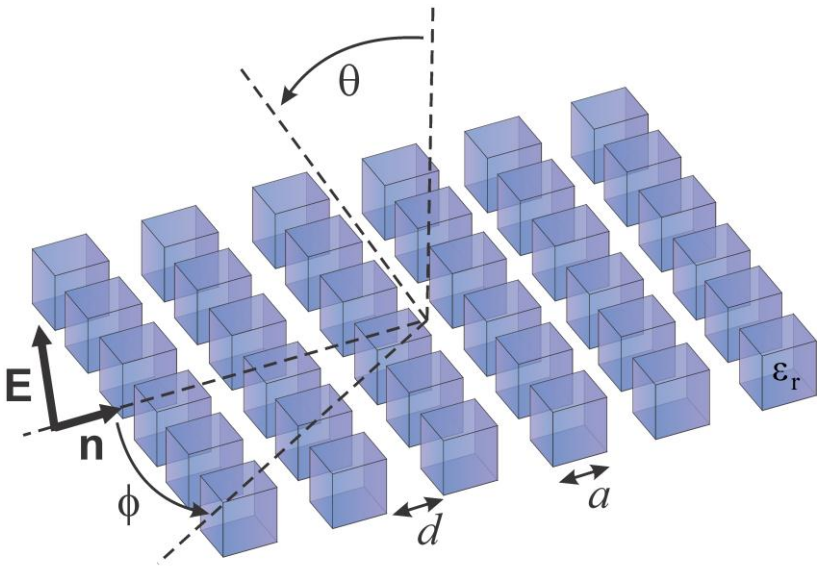

Fig. 21. Array of homogeneous dielectric cubical scatterers excited by a uniform plane wave ($\theta_{inc} = 90°, \phi_{inc} = 0°$)

The number of VIE unknowns per subsystem is $N_V = 756$ and the total number of diakoptic unknowns (sum of unknowns on all diakoptic surfaces) is $2N_S = 6{,}144$, which results in a total of $N_{tot}^{Dia} = 6{,}900$ unknowns and $T_{tot}^{Dia} = 155\,s$ of computation time for the analysis. All computations presented in this paper are carried out without parallelization or using symmetry on an Intel® Core™2 Quad CPU Q95550 at 2.83 GHz, with 8 GB RAM, under 64-bit Windows 7 operating system.

Fig. 22 shows the normalized bistatic radar cross section (RCS) of the array in a characteristic plane ($\phi = 0°$).We compare the diakoptic results with the solution obtained by the pure MoM-VIE method, which requires $N_{tot}^{VIE} = 6{,}912$ unknowns and $T_{tot}^{VIE} = 1{,}135\,s$ of computation time, and observe an excellent agreement of the two sets of results. In this example, the advantage of the diakoptic approach is not so much in the reduction of the number of

unknowns, but of the computation time (about 7.3 times). Moreover, the RAM memory consumption is $M_{\text{tot}}^{\text{Dia}} = 160\,\text{MB}$ for the VIE-SIE-diakoptic method (note that in the diakoptic approach, the largest matrix equation that has to be solved is of the size N_{S}) and $M_{\text{tot}}^{\text{VIE}} = 764\,\text{MB}$ for the MoM-VIE method. As additional validation, shown in Fig. 22 is an excellent agreement of the diakoptic solution with the RCS computed using the pure MoM-SIE method, which takes $N_{\text{tot}}^{\text{SIE}} = 6{,}144$ unknowns, $T_{\text{tot}}^{\text{SIE}} = 413\,\text{s}$ of computation time, and $M_{\text{tot}}^{\text{SIE}} = 604\,\text{MB}$ of RAM memory.

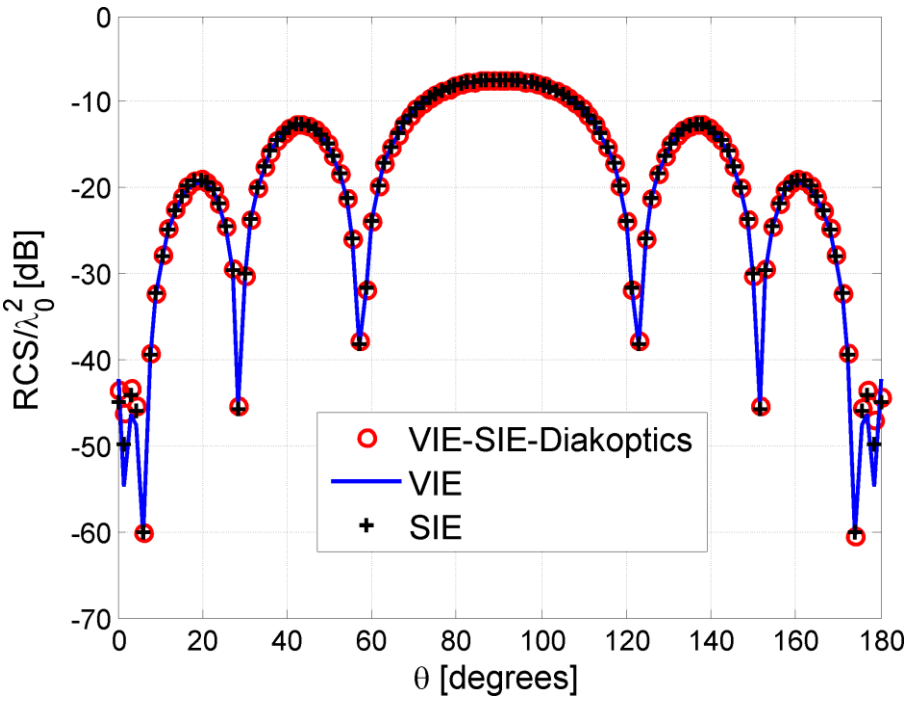

Fig. 22. Normalized bistatic radar cross section (RCS) of the array in the $\phi = 0^\circ$ cut, computed by the proposed VIE-SIE-diakoptic method, by the pure MoM-VIE technique and the pure MoM-SIE technique.

4.3.2 Array of Homogeneous Dielectric Spherical Scatterers

As an example of curved structures, we replace the cubical scatterers in Fig. 22 by spherical ones, as portrayed in Fig. 23, where $a = \lambda_0 / 2.31$ (sphere diameter), $d = \lambda_0 / 4.29$, $\varepsilon_r = 4$, $\theta_{inc} = 90°$, and $\phi_{inc} = 0^\circ$.

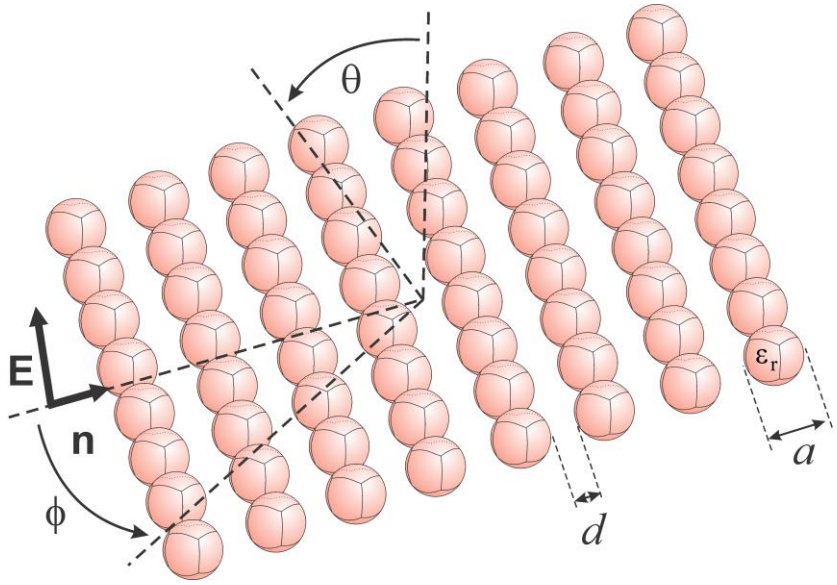

Fig. 23. Array of homogeneous dielectric spherical scatterers excited by a uniform plane wave ($\theta_{inc} = 90°, \phi_{inc} = 0^\circ$).

Each diakoptic subsystem, in spite of curvature, is again modeled by a single generalized hexahedral VIE element with $K_u = K_v = K_w = 2$ and $N_u = N_v = N_w = 4$, enclosed by a diakoptic surface composed of six generalized quadrilateral SIE patches with $K_u = K_v = 2$ and $N_u = N_v = 2$, so the numbers of unknowns are $N_V = 240$, $2N_S = 6{,}144$, and $N_{tot}^{Dia} = 6{,}384$, computation time is $T_{tot}^{Dia} = 242$ s, and RAM memory consumption is $M_{tot}^{Dia} = 152$ MB.

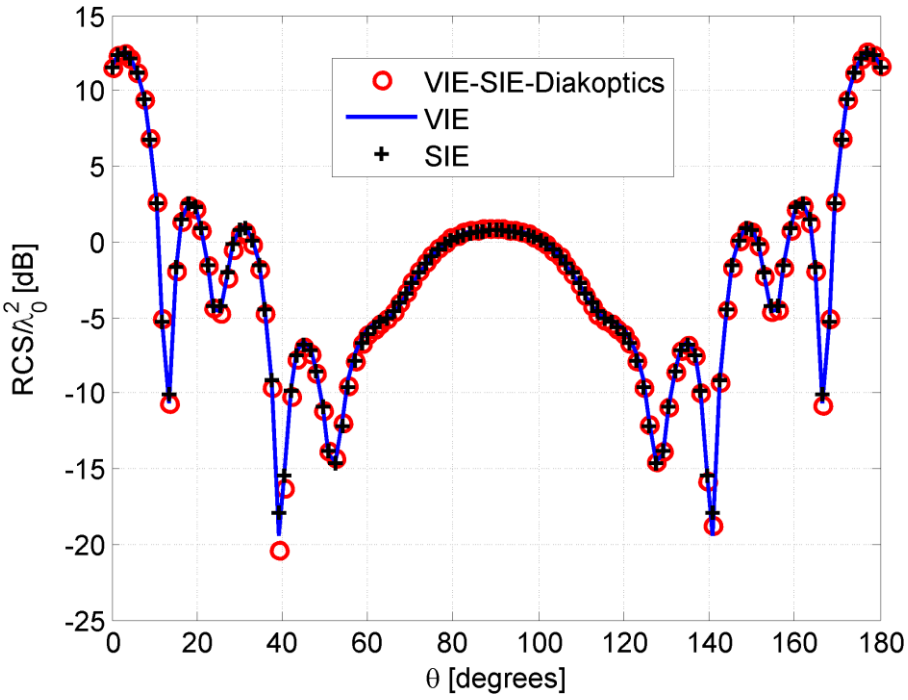

Fig. 24. Normalized bistatic RCS results in the $\phi = 90^{\circ}$ cut, obtained by the VIE-SIE-diakoptic, pure MoM-VIE, and pure MoM-SIE methods.

The agreement of the RCS results with both the pure MoM-VIE ($N_{\text{tot}}^{\text{VIE}} = 15{,}360$, $T_{\text{tot}}^{\text{VIE}} = 4{,}811\,\text{s}$, $M_{\text{tot}}^{\text{VIE}} = 3.7\,\text{GB}$) and MoM-SIE solutions is, as can be observed from Fig. 24, again excellent, and the computation time and memory consumption are considerably in favor of the diakoptic method (reduction by 20 times in computation time and by 24 times in memory consumption when compared to the MoM-VIE method).

4.3.3 Array of Continuously Inhomogeneous Spherical Scatterers

As an example of inhomogeneous structures, that are also curved, we next consider a 4×4 array of continuously inhomogeneous dielectric spherical scatterers of diameters $a=\lambda_0/1.5$, shown in Fig. 25. All sphere-to-sphere distances are $d=\lambda_0/3$ and $\theta_{\text{inc}}=0°$ and $\phi_{\text{inc}}=0^{\circ}$ for the impinging uniform plane wave. The inhomogeneity consists of a linear radial variation of the relative permittivity from $\varepsilon_r=1$ at the surface to $\varepsilon_r=6$ at the center of the spheres, as depicted in the inset of Fig. 26.

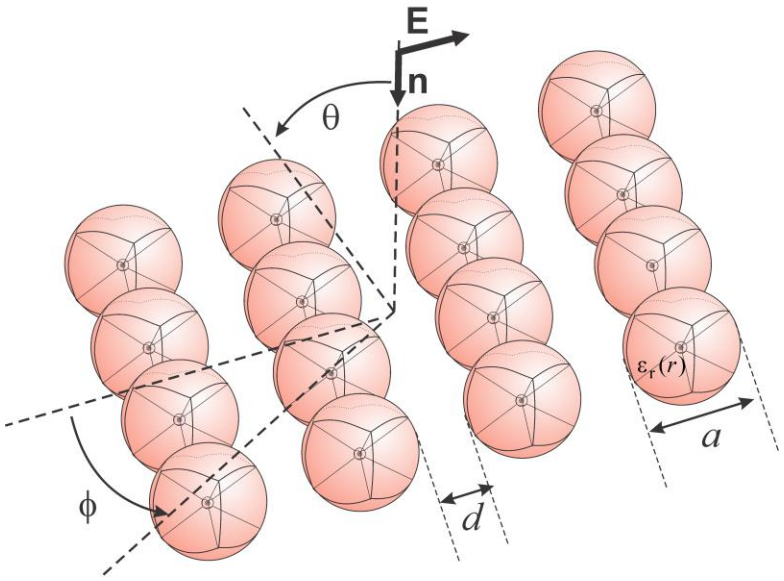

Fig. 25. Array of continuously inhomogeneous dielectric spherical scatterers

Each scatterer is modeled by seven curvilinear hexahedral VIE elements (with $K_u=K_v=K_w=2$), one element (with $N_u=N_v=N_w=2$) approximating the central sphere (of diameter $a/20$) and six continuously inhomogeneous cushion-like elements (with $N_u=N_v=N_w=3$) attached to the corresponding sides of the central element, which can be seen in Fig. 25. The diakoptic surface enclosing each subsystem consists of six SIE patches with

$K_u = K_v = 2$ and $N_u = N_v = 4$. The resulting numbers of unknowns are $N_{\mathrm{V}} = 630$ (per subsystem), $2N_{\mathrm{S}} = 6{,}144$ (total), and $N_{\mathrm{tot}}^{\mathrm{Dia}} = 6{,}774$, and the total computation time is $T_{\mathrm{tot}}^{\mathrm{Dia}} = 795\,\mathrm{s}$.

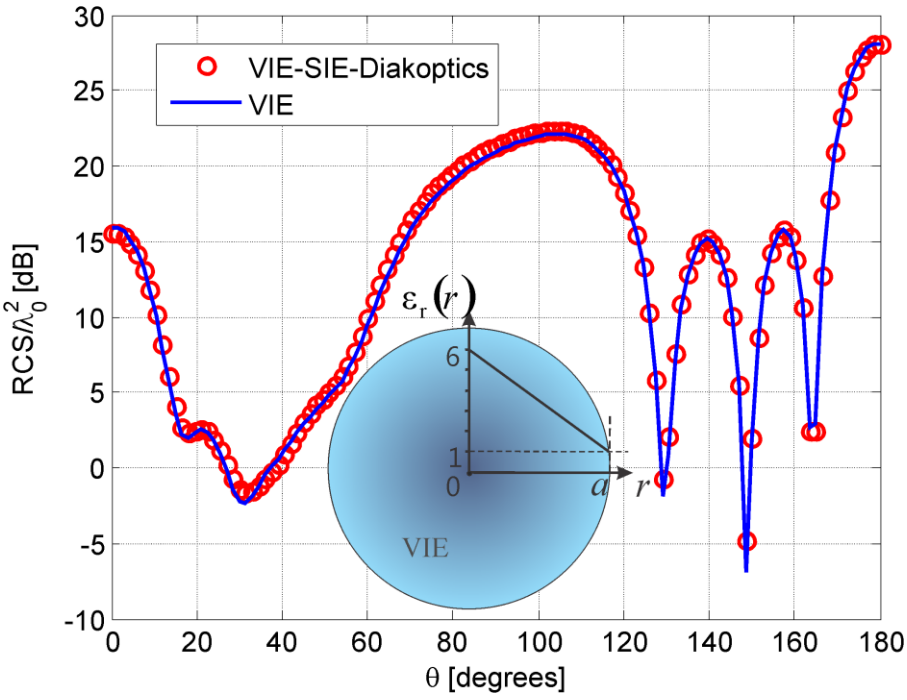

Fig. 26. Bistatic RCS results in the $\phi = 90^{\circ}$ cut obtained by the VIE-SIE-diakoptic and pure MoM-VIE methods.

In Fig. 26, an excellent agreement of the RCS results obtained by the diakoptic method and those using the pure MoM-VIE method, with $N_{\mathrm{tot}}^{\mathrm{VIE}} = 10{,}080$ and $T_{\mathrm{tot}}^{\mathrm{VIE}} = 29{,}820\,\mathrm{s}$, is observed. In this case, the acceleration is even more dramatic (about 37 times) than in previous examples, because the MoM-VIE computation of matrix entries for a subsystem involving several inhomogeneous hexahedra is considerably more time consuming than for subsystems with a

single homogeneous element. The required RAM memory for the VIE-SIE-diakoptic and MoM-VIE solutions is $M_{\text{tot}}^{\text{Dia}} = 157\ \text{MB}$ and $M_{\text{tot}}^{\text{VIE}} = 1.6\ \text{GB}$, respectively.

4.3.4 Diakoptic Decomposition of a Large Dielectric Slab

As an example of a single solid object decomposed into diakoptic subsystems, consider scattering from a dielectric slab with relative permittivity $\varepsilon_r = 2.25$ and dimensions $6\lambda_d \times 6\lambda_d \times 2\lambda_d$, with λ_d standing for the wavelength in the dielectric. The plane wave excitation is as in the previous examples ($\theta_{\text{inc}} = 90°$, $\phi_{\text{inc}} = 0°$).

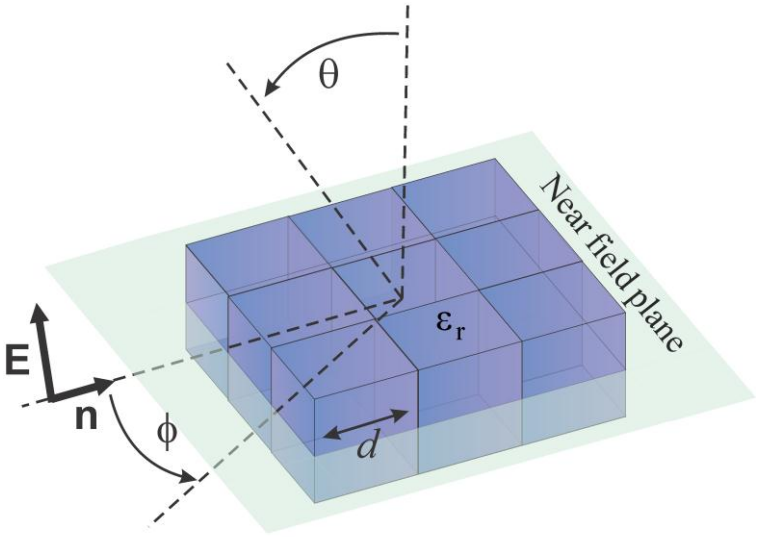

Fig. 27. Large dielectric slab decomposesd into nine diakoptic subsystems

The slab is decomposed into nine cubical diakoptic subsystems of edge lengths $d = 2\lambda_d$, as shown in Fig. 27, and each subsystem is modeled by a single VIE element, with $K_u = K_v = K_w = 1$ and current-expansion orders varied as $N_u = N_v = N_w = N = 4$, 6, 8 and 9

(corresponding numbers of VIE unknowns $N_{\mathrm{V}} = 240$, 756, 1,728 and 2,430 per subsystem), and is enclosed by a six-patch diakoptic surface, with $K_u = K_v = 1$ and $N_u = N_v = 6$ (total of $2N_{\mathrm{S}} = 7{,}776$ diakoptic unknowns).

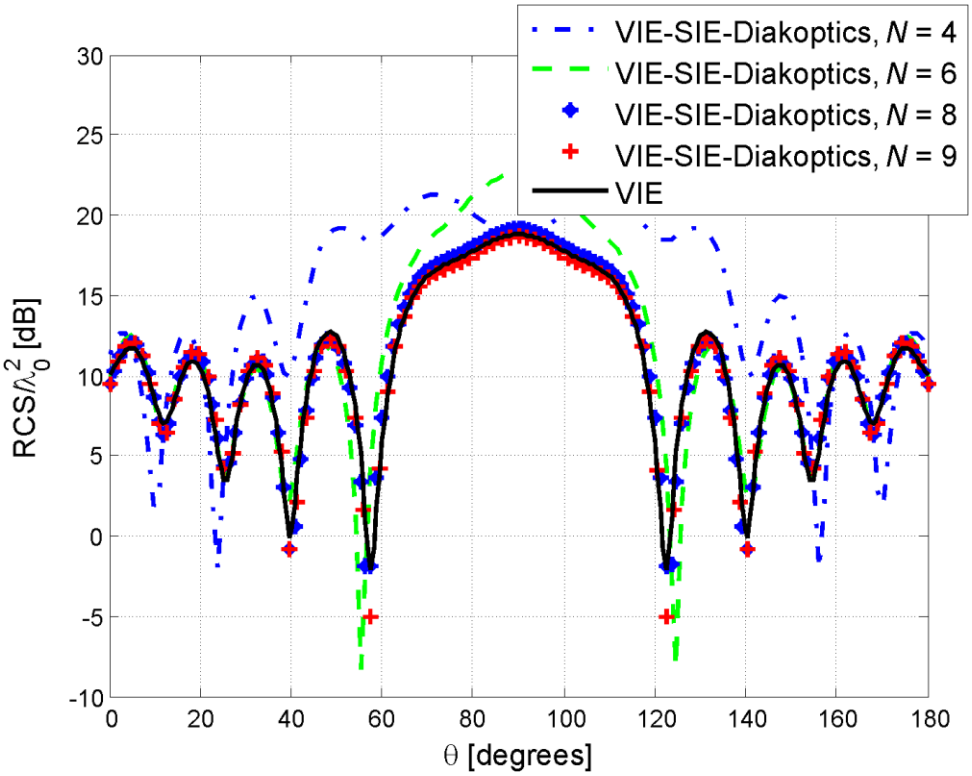

Fig. 28. Convergence analysis of the VIE-SIE-diakoptic solution for the normalized bistatic RCS ($\phi = 0^\circ$ cut) of the slab with increasing MoM-VIE polynomial current-approximation orders $N_u = N_v = N_w = N$ and comparison with results obtained using the pure MoM-VIE method.

In Fig. 28, we observe a convergence of the VIE-SIE-diakoptic RCS results for the dielectric slab with increasing orders of VIE basis functions (*p*-refinement), as well as an excellent agreement of the ninth-order diakoptic solution ($N_{\mathrm{tot}}^{\mathrm{Dia}} = 10{,}206$, $T_{\mathrm{tot}}^{\mathrm{Dia}} = 740\,\mathrm{s}$, $M_{\mathrm{tot}}^{\mathrm{Dia}} = 336\,\mathrm{MB}$) with the results obtained by the pure MoM-VIE method with

$N_u = N_v = N_w = 9$ ($N_{\text{tot}}^{\text{VIE}} = 21{,}870$, $T_{\text{tot}}^{\text{VIE}} = 7{,}620\,\text{s}$, $M_{\text{tot}}^{\text{VIE}} = 7.7\,\text{GB}$ of RAM). Hence the diakoptic method is 10.3 times faster and 23 times less expensive at memory consumption than the pure MoM approach in this case. For additional validation of the proposed diakoptic method, Fig. 29 shows the near (internal or external) total electric field computed in the plane indicated in Fig. 27.

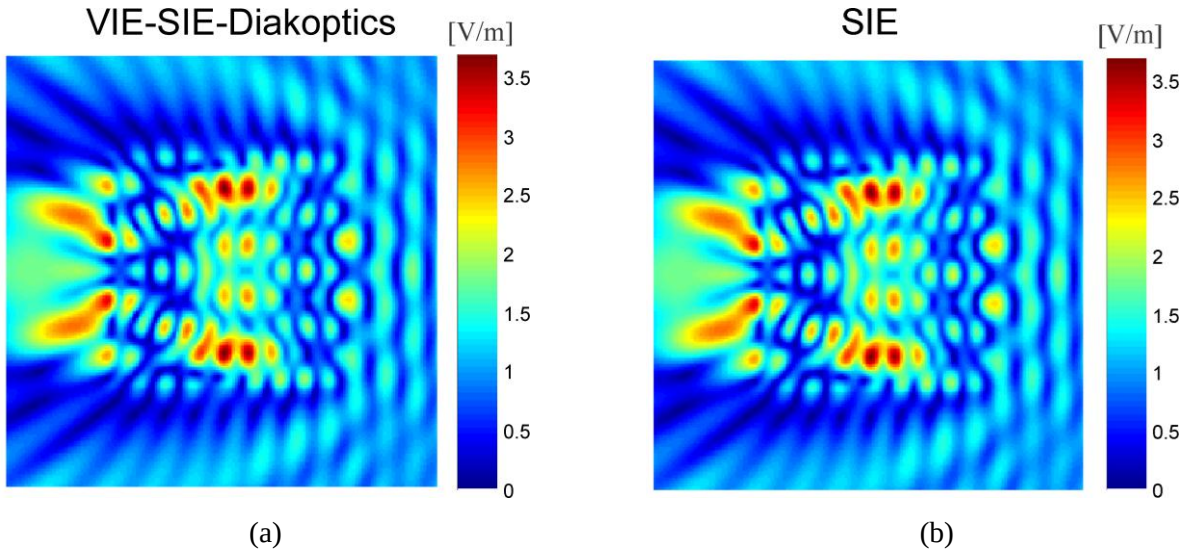

(a) (b)

Fig. 29. Magnitude of the near total electric field inside and around the dielectric slab scatterer computed in the plane indicated in Fig. 27, where the size of the near-field computation area is $11\lambda_{\text{d}} \times 11\lambda_{\text{d}}$, and it cuts through the middle of the vertical dimension of the slab: comparison of (a) VIE-SIE-diakoptic results and (b) pure MoM-SIE reference solution.

The VIE-SIE-diakoptic results are compared with a fully *hp*-refined SIE solution ($N_{\text{tot}}^{\text{SIE}} = 11{,}648$, $T_{\text{tot}}^{\text{SIE}} = 2880\,\text{s}$, and $M_{\text{tot}}^{\text{SIE}} = 2.17\,\text{GB}$), and an excellent agreement of the two sets of results is observed.

4.3.5 Diakoptic Decomposition of a Human Phantom

Finally, as an example of a complex objects decomposed into completely different subsystems, consider scattering from a human phantom. The phantom is excited by the plane wave propagating along *x*-direction ($\theta_{\text{inc}} = 90°$, $\phi_{\text{inc}} = 0^{\circ}$) at the frequency 900 MHz. The human phantom is decomposed into four diakoptic subsystems as shown in the inset of Fig. 30. Subsystems are modeled by 1436, 1310, 1050 and 985 VIE hexahedra and 1124, 1114, 1018 and 976 SIE quadrilaterals respectively (total of $2N_{\text{S}} = 16{,}928$ diakoptic unknowns). Initial triangular mesh was provided by NEVA Electromagnetics [15] and was re-meshed in ICEM CFD 15.0.

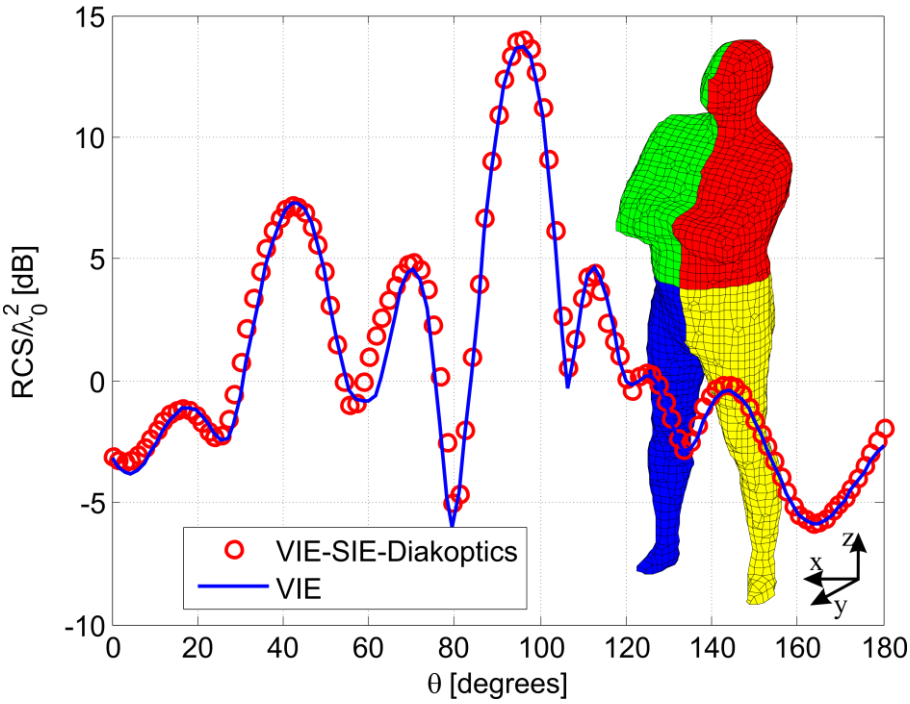

Fig. 30. A human phantom decomposed into four diakoptic subsystems. Comparison of the VIE-SIE-diakoptic solution for the normalized bistatic RCS ($\phi = 0°$ cut) of the human phantom with results obtained using the pure MoM-VIE method.

In Fig. 30, we observe a good agreement of the VIE-SIE-diakoptic RCS results for the human phantom ($N_{\text{tot}}^{\text{Dia}} = 32{,}940$, $T_{\text{tot}}^{\text{Dia}} = 19{,}097\,\text{s}$, $M_{\text{tot}}^{\text{Dia}} = 2.25\,\text{GB}$) with the solution obtained by the pure MoM-VIE method ($N_{\text{tot}}^{\text{VIE}} = 16{,}012$, $T_{\text{tot}}^{\text{VIE}} = 522{,}870\,\text{s}$, $M_{\text{tot}}^{\text{VIE}} = 4.1\,\text{GB}$). Hence the diakoptic method is 27.4 times faster and 1.82 times less expensive at memory consumption than the pure MoM approach in this case. Note, VIE-SIE-diakoptics requires less memory than pure VIE, because of the nature of the diakoptic computation. In addition, memory savings are not very pronounced, because all of the domains are different and require individual computation.

4.4 Summary

This section has proposed a novel diakoptic domain-decomposition method for 3-D electromagnetic analysis based on MoM-VIE-SIE modeling. The method breaks the original structure into a number of non-overlapping closed-region subsystems containing inhomogeneous dielectric materials and an open-region subsystem enclosing all other subsystems. Each subsystem is analyzed in a completely independent manner by applying the double-higher-order large-domain Galerkin MoM-VIE-SIE or MoM-SIE solvers. The solution to the original problem is therefore obtained from linear relations between coefficients in expansions of equivalent electric and magnetic surface currents on diakoptic boundary surfaces and representations of electromagnetic subsystems by diakoptic matrices.

The proposed VIE-SIE-diakoptic method has been demonstrated, evaluated, and discussed in several characteristic scattering examples. Such examples include homogeneous and continuously inhomogeneous dielectric structures, as well as objects with both flat surfaces/sharp edges and pronounced curvature, and far-field/ near-field computations. The results obtained by the diakoptic method have been validated against the solutions using both the pure MoM-VIE

method and the pure MoM-SIE method. Numerical examples have demonstrated that the proposed VIE-SIE-diakoptic method dramatically increases the efficiency of the conventional MoM-VIE approach. When compared to the pure MoM-VIE technique, implementing the same type of discretization (double-higher-order large-domain Galerkin discretization), the diakoptic approach enables accelerations and memory savings of one to two orders of magnitude, while fully preserving the accuracy of the analysis. Note that the acceleration and memory reduction achieved in the presented examples fit well within the theoretically derived performances of the diakoptic approach [63]. Moreover, the more complex the original system (problem) is, the more advantageous is the VIE-SIE-diakoptic analysis over the equivalent conventional (pure MoM-VIE) approach. The research has also demonstrated that the general diakoptic methodology can effectively include VIE-based subsystems and has shown how that can be done. The proposed method is, to the best of our knowledge, the first general DD method based on MoM-VIE or MoM-VIE-SIE modeling in computational electromagnetics.

5 ORTHOGONALIZATION OF BASIS FUNCTIONS

5.1 Introduction

In general, method of moments (MOM) requires fewer unknowns than differential equation techniques. However, due to the nature of the computation of matrix elements, the matrix system is usually dense and ill-conditioned. This results in the complication of utilization of iterative solvers, which are *N* times faster than direct ones, with *N* being the number of unknowns. To overcome this issue in [26] [36] the authors introduce hierarchical Legendre basis functions for volume and volume-surface integral equations, where they show drastic improvement in conditioning of the matrix system. In [45] new maximally-orthogonalized higher order bases are proposed for wires, quadrilaterals and hexahedra, where the efficiency of the new bases is demonstrated for surface integral equation MoM formulation. In this part of the thesis the goal is to investigate different types of bases functions for volume integral equation code and determine which of them result in the lowest matrix conditioning.

5.2 Divergence-Conforming Expansions

In section 1.3 the equivalent electrical displacement vector is expanded in terms of basis functions as follows

$$\mathbf{D} = \sum_{p=0}^{N_u} \sum_{s=0}^{N_v-1} \sum_{t=0}^{N_w-1} \alpha_{upst}\, \mathbf{f}_{upst} + \sum_{p=0}^{N_u-1} \sum_{s=0}^{N_v} \sum_{t=0}^{N_w-1} \alpha_{vpst}\, \mathbf{f}_{vpst} + \sum_{p=0}^{N_u-1} \sum_{s=0}^{N_v-1} \sum_{t=0}^{N_w} \alpha_{wpst}\, \mathbf{f}_{wpst}, \qquad (59)$$

where **f** are divergence-conforming hierarchical-type vector basis functions defined by

$$\mathbf{f}_{upst} = \frac{Q_p(u)\,P_s(v)P_t(w)}{\mathfrak{I}}\,\mathbf{a}_u$$
$$\mathbf{f}_{vpst} = \frac{P_p(u)Q_s(v)P_t(w)}{\mathfrak{I}}\,\mathbf{a}_v \qquad (60)$$
$$\mathbf{f}_{wpst} = \frac{P_p(u)P_s(v)Q_t(w)}{\mathfrak{I}}\,\mathbf{a}_w$$

Originally, in section 1.3 *Q* and *P* expansion functions are defined as

$$Q_p(u) = \begin{cases} 1-u, & p=0 \\ u+1, & p=1 \\ u^p - 1, & p \geq 2, \text{even} \\ u^p - u, & p \geq 3, \text{odd} \end{cases}, \qquad P_k(u) = u^k \quad , \qquad (61)$$

which will be referred as a *classic* set of functions. However, these expansions result in a very ill conditioned matrix equation, which was shown in section 1.5.2. In [26] [36], it was proposed to use Legendre and modified Legendre polynomials which, due to their orthogonality to each other, result in a smaller condition number. In addition, the accuracy of the solution representation does not suffer, because polynomial functions span the same functional space as the simple power functions. In this case *Q* and *P* functions are represented as follows

$$Q_m(u) = \begin{cases} 1-u & m=0 \\ 1+u & m=1 \\ P_m(u) - P_{m-2}(u) & m \geq 2 \end{cases} \quad , \qquad P_k(u) = L_k(u) \qquad (62)$$

where $L_m(u) = \frac{1}{2^m m!}\frac{\mathrm{d}^m}{\mathrm{d}u^m}\left(u^2-1\right)^m$ are Legendre polynomials. The *Q*-functions are usually referred to as *near-orthogonal* basis functions. Further, in [35] the authors claim that the best matrix conditioning was obtained by scaling the basis functions so that the Euclidean norm of each basis function is unity on a square patch of unit side length. These scaling factors are defined as follows:

$$\tilde{C}_m = \begin{cases} \dfrac{\sqrt{3}}{4} & m = 0,1 \\ \dfrac{1}{2}\sqrt{\dfrac{(2m-3)(2m+1)}{2m-1}} & m \geq 2 \end{cases}, \quad C_m = \sqrt{m+\frac{1}{2}} \tag{63}$$

where $\tilde{C}_m$ and C_m are coefficients multiplying *Q*- and *P*-functions respectively.

Since *P*-functions are adopted in the form of Legendre polynomials (62), they are already fully orthogonal with maximum absolute value on the interval [-1, 1] being equal to one, i.e. $|P_k(\pm 1)| = 1$. In the case of *Q*-expansions (62), the zeroth and first order functions are the same as in (61) (in section 1.3 the importance of these first two basis functions for imposing continuity condition of the vector **D** was discussed), which are not orthogonal to the $m \geq 2$ order functions. Therefore, the matrix of the inner product $S_{ij} = \langle Q_i, Q_j \rangle = \int_{-1}^{1} Q_i(u) Q_j(u) \mathrm{d}u$ is not diagonal (Fig. 31 (b)), which would have been an ideal case.

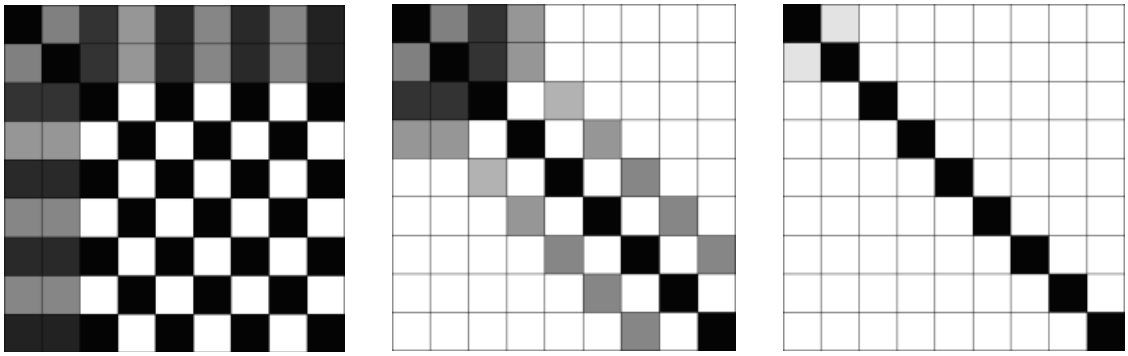

(a) (b) (c)

Fig. 31. Sketch of the inner product matrix: (a) classic, (b) near-orthogonal, and (c) maximally-orthogonal.

This issue can be improved by the construction of polynomials based on a two-step Gram-Schmidt procedure [45], which ensures the maximal orthogonality and divergence-conformity of

the new basis (inner product matrix is show in Fig. 31 (c)). The basic form of the obtained basis functions of orders up to 8 is represented in Table IV.

Table IV. Maximally-Orthogonalized *Q*-funqtions.

K	$Q_k(u)$
2	u^2-1
3	u^3-u
4	$7u^4-8u^2+1$
5	$3u^5-4u^3+u$
6	$33u^6-51u^4+19u^2-1$
7	$\frac{143}{15}u^7-\frac{253}{15}u^5+\frac{25}{3}u^3-u$
8	$143s^8-286u^6+176u^4-34u^2+1$

Table V. Normalization Coefficients for the Maximally-Orthogonalized *Q*-funqtions.

K	Norm to ±1	Euclidean
2	1.000000	0.968246
3	2.598076	2.561738
4	0.777778	0.838525
5	3.620824	4.248161
6	0.645493	0.816397
7	4.352125	5.882766
8	0.563718	0.808509

In order to minimize the condition number, the next step is to find an optimal normalization of the *Q*-functions, i.e. to determine appropriate scaling factors. Two normalization cases are considered. In the first case the functions are normalized by their maximum absolute value. This scaling will be referred as “Norm ±1”, since maximal and minimal values are +1 and -1. In the second case, Euclidean norms of all basis functions are set to unit value, which will be referred

to as “Euclidean”. For the maximally-orhtogonalized *Q*-functions scaling factors are given in the Table V.

5.3 Numerical Results and Discussion

As it was shown in section 1.5.2, the condition number almost does not depend on the geometrical order of element. Therefore, in this section, to accelerate numerical computations only first order geometrical elements are used. As an example consider scattering from a dielectric cube, with edge size $a = 4\lambda_0$ and permittivity $\varepsilon_r = 4.0$. To isolate the effect of increasing the polynomial order, the matrix sizes were kept as close to each other as they can be with the given expansion order. According to [45] the best condition number was obtained for maximally-orthogonal expansions scaled according to the Euclidean norm. Therefore these basis functions were implemented. The results obtained for the condition number are presented in the Table VI.

Table VI. Condition Number for Dielectric Cube in Cases of Classic and Maximally-Orthogonal Expansions

Polynomial order	Element size	Number of unknowns	Condition number	
			Classic	Max-orthogonal
N = 2	0.5λ	13056	1.38E+08	8.06E+07
N = 3	0.8λ	10800	3.11E+10	3.01E+08
N = 4	λ	13056	8.17E+11	2.02E+08
N = 5	1.33λ	10800	7.46E+13	1.12E+08
N = 6	2λ	5616	2.83E+16	9.56E+07
N = 7	2λ	8820	3.71E+16	4.46E+08

As it can be seen from the Table VI the condition number of the matrix generated by expansion of the vector **D** in terms of classic basis functions grows very rapidly with increase of

the expansion order. In the case of maximally-orthogonalized expansion a condition number increases less than the order of magnitude, and even decreases for a small matrix size. Note that similar results were obtained in [45] for MoM-SIE approach.

5.4 Summary

Maximally orthogonalized divergence-conforming higher order basis functions, proposed in [45] for elements in the form of generalized wires, quadrilaterals and hexahedra, were implemented in double-higher-order volume integral equation (MoM-VIE). It was illustrated by the numerical example that the implementation of the above mentioned bases dramatically improves the condition number of the matrix, while spanning the same polynomial space as the classic expansions. Therefore, without loss in accuracy of the field approximation within a hexahedral element, a better condition number of the MoM matrix was obtained.

6 PARALLELIZATION OF THE GENERALIZED VOLUME/SURFACE INTEGRAL EQUATION METHOD OF MOMENTS CODE

6.1 Introduction

Lately, with the growing popularity of numerical methods and their application for industrial and academic purposes, computational problems have become more and more time and memory consuming. Some numerical problems, if being calculated on the simple PC, can take weeks, even months, of computational time. This contradicts the general purpose of numerical methods – fast analysis of the full EM system. Such a problem can be overcome by utilizing the technological advancement in high performance computing (HPC). However, in order to use the full capability of the HPC system, parallelization of the numerical code is required, which results in additional programming work. In this section the already developed MoM-VSIE code is parallelized for ISTeC Cray, which is a supercomputer owned by Colorado State University.

6.2 Parallel Algorithm Implementation into MoM-VSIE Code

As a result of method of moments (MoM) discretization of the volume/surface integro-differential equations a dense system of linear equations is obtained. As a direct matrix solver is used, the system matrix storage requires order of N^2 memory, where N is a number of unknowns. To run computationally and storage expensive simulation the in-core parallelization of the VSIE code for a distributed memory system based on the message passing interface (MPI) basic linear algebra communication subprograms (BLACS) was developed [71]. The Cray supercomputer, used for simulations, contains 52 compute nodes, with a total of 104 AMD Magny Cours 64-bit 1.9-GHz processors (two per node), where each processor has 12 cores. There is a 32-GB RAM

memory available on each node, while the interconnection between the nodes is SeaStar2+ with 2D torus topology. For the in-core parallel solution of matrix equation ScaLAPAK solver, based on LU factorization was used. The solver requires the matrix to be stored in a 2D block-cyclic distribution [72] , as it is shown in the Fig. 32.

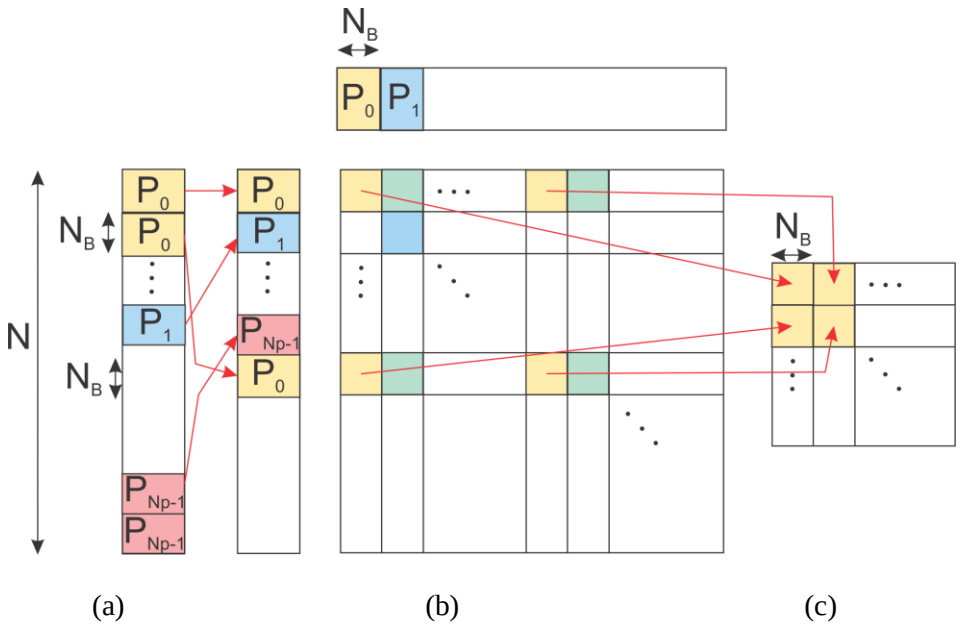

Fig. 32. 2D block-cyclic matrix distribution for N_pxN_p process grid with block dimensions equal to N_BxN_B : (a) being a global unknowns descriptor and its mapping to a 2D block-cyclic distribution descriptor, (b) global system matrix, and (c) local matrix on the zeroth processor [71].

In the parallelization algorithm, the first available MPI processes are mapped into a logical 2D process mesh, so that each process can be addressed by two coordinates. Next, each process allocates the necessary memory for the local part of the matrix and calculates its entries as it is shown in the Fig. 32. Note that the unknowns are directly connected to the geometrical tessellation elements and for certain matrix entries computations it is required to perform integration on two different elements. Therefore, in certain cases a burdensome integration over a geometrical element needs to be repeated by several different processes. The other way to

parallelize the code was to distribute memory according to geometrical elements and then exchange the data to fill out the proper matrix elements. However, numerical experiments have shown that, the recalculation of a geometrical element is less expensive than the internode communication of pre-calculated values.

6.3 Numerical Results and Discussion

6.3.1 Scattering from the Human Brain

To demonstrate the efficiency of the parallel MoM-VIE code, a computation of a human brain model is performed. The brain is modeled by 227 hexahedral ($K_u = K_v = K_w = 2$) VIE elements, as indicated in Fig. 33 (b), with the orders N_u, N_v, and N_w equal to 2, which results in a total of $N_{\text{unkn}}^{\text{VIE}} = 6{,}024$ unknowns. The model was illuminated by the plane wave, impinging

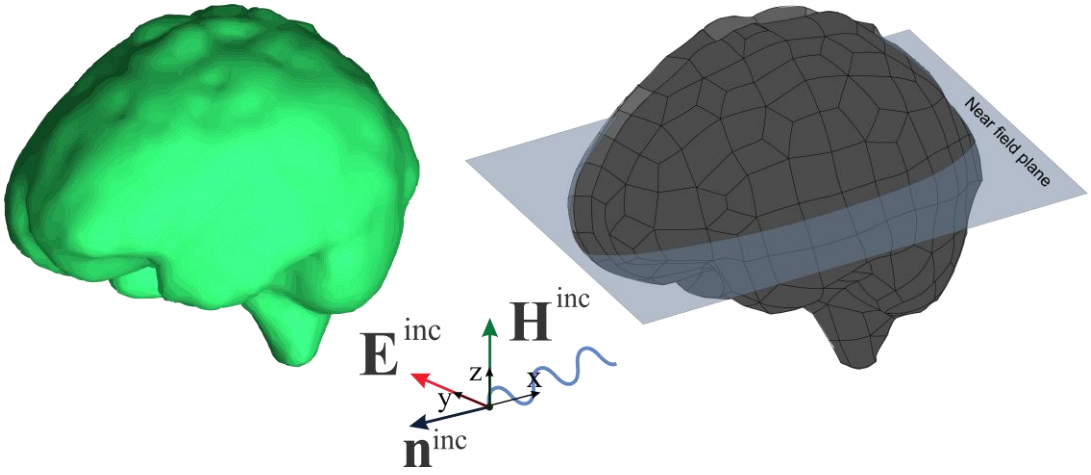

(a) (b)

Fig. 33. Human brain model: (a) A STL surface of the brain provided by NEVA Electromagnetics [15] and (b) re-meshed into curvilinear hexahedra in ICEM CFD 15.0

from -*x* direction at frequency $f = 900\,\mathrm{MHz}$. Shown in Fig. 34 is the simulated near electric field in the plane, passing through the middle of the brain, obtained by the proposed higher order VIE technique. The model was run in sequential and parallel (on 4, 16 and 64 processes) fashion.

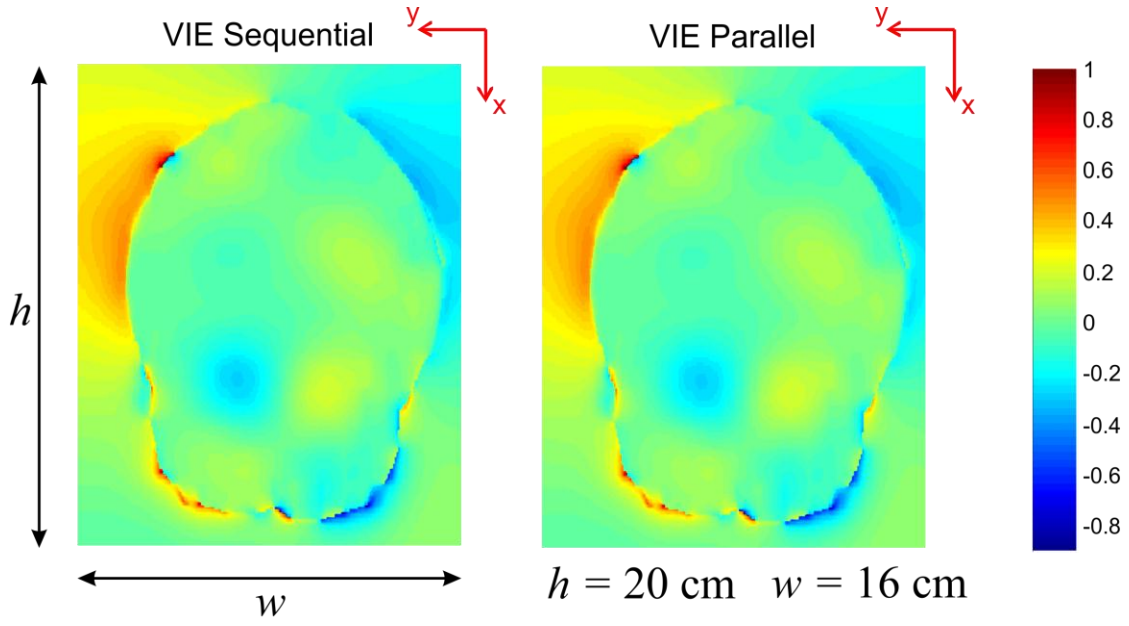

Fig. 34. Normalized near *Ey* component of electric field inside and around the brain model computed in the plane indicated passing through the middle of the brain, (a) MoM-VIE sequential results and (b) MoM-VIE parallel solution.

In Table VII are shown the computational times for sequential and parallel versions (all ran on Cray supercomputer) along with the parallel code efficiency. Note, that parallel code efficiency is calculated as $E_\mathrm{p} = \left((T_\mathrm{s}/T_\mathrm{p})\right)/P$, where T_s and T_p are computational times for sequential and parallel codes respectively, and P is the number of processes. As it can be seen from the Table VII, the efficiency of the code drops very rapidly with an increase in the number of processes. This phenomenon occurs due to the fact that the number of elements being calculated on each process does not decrease proportional to the number of processes, which

heavily depends on geometrical alignment of elements in the model. For example, the ideal number of elements per process for N=2x2 should be 138, but in actual computation it varies from 117 to 145. For this case the number deviates from the expected within the 10% range, which is acceptable. However, in the case of N=8x8 the number of elements per process should be 34, while the real distribution varies between 30 and 64, the upper bound of which is almost twice as big. In order to improve the efficiency of the parallel code further acceleration based on the geometrical model preprocessing and proper element clusterization is required.

Table VII. Computational Times for Sequential and Parallel VIE Computations of the Human Brain Model; Parallel Code Speedup and Efficiency

Number of processes	Computational time	VIE elements per process	Speedup T_s/T_p	Parallel code efficiency E_p
N = 1	3 h 23 min 5 sec	227		
N = 2x2	1 h 19 min 8 sec	117-145	2.5663	0.6416
N = 4x4	35 min 10 sec	60-93	5.7749	0.3609
N = 8x8	17 min 30 sec	30-64	11.6048	0.1813

6.3.2 Luneburg Lens Illuminated by a Corrugated Horn Antenna

To demonstrate the efficiency of the parallel MoM-VSIE approach the composite metallic/dielectric structure is calculated. In order to fully exploit the parallel code performance the piecewise-homogeneous model of Luneburg Lens, presented in section 2.3.4, is illuminated by a corrugated horn antenna. The numerical model consists of 270 homogeneous hexahedral elements of the first geometrical order and forth polynomial orders ($K_u = K_v = K_w = 1$ and $N_u = N_v = N_w = 4$), 124 bilinear quadrilateral patches ($K_u = K_v = 1$ and $N_u = N_v = 3$) and 1 wire ($K_u = 1$ and $N_u = 3$) shown in the Fig. 35, resulting in $N_{\text{unkn}}^{\text{VSIE}} = 55{,}413$ unknowns. Fig. 36

shows the absolute value of a total near electric field calculated in the plane, as indicated in Fig. 35 by the parallel code.

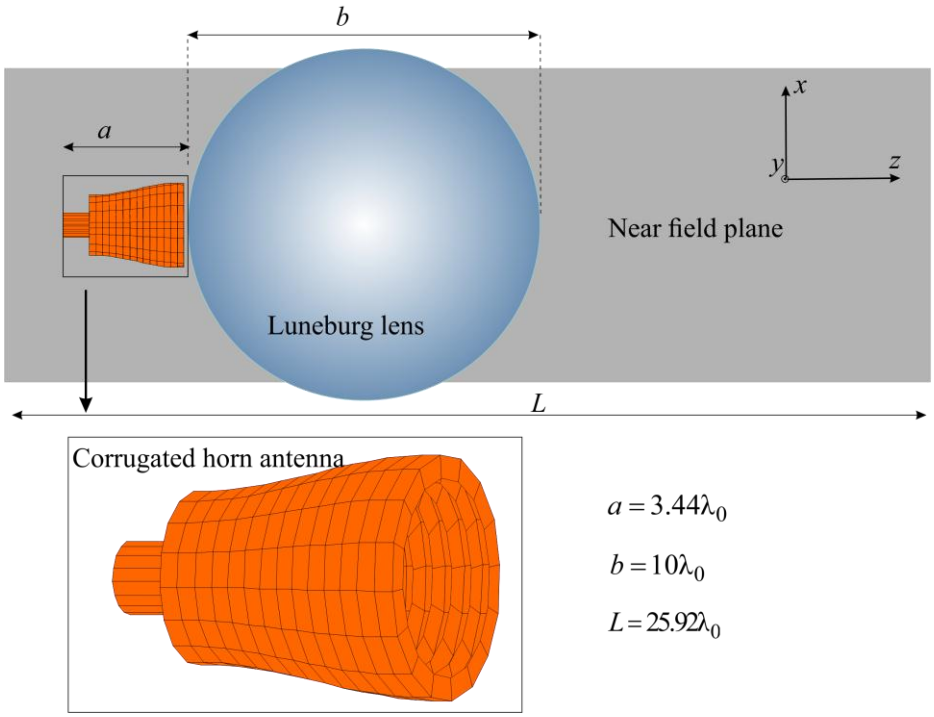

Fig. 35. Luneburg lens illuminated by a corrugated horn antenna

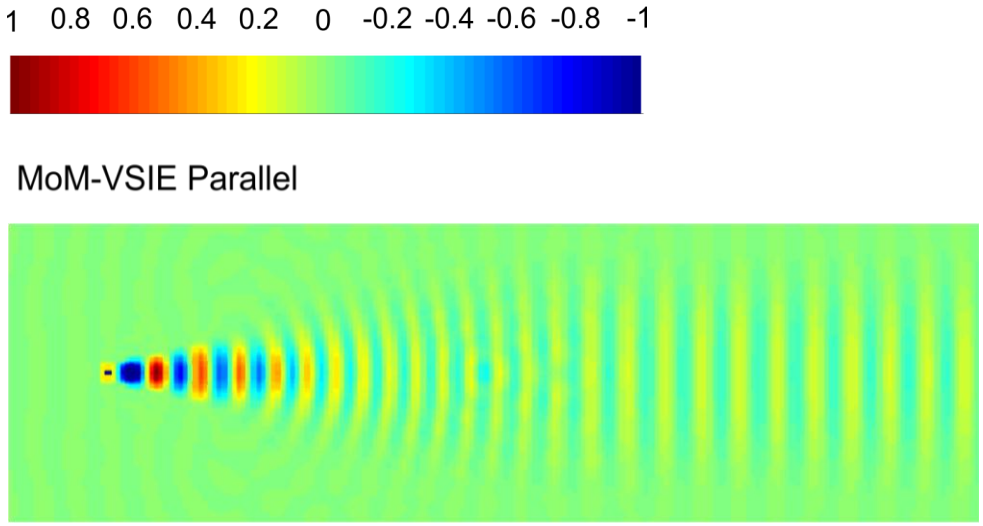

Fig. 36. Normalized near *Ey* component of electric field inside and around the Luneburg lens computed in the plane indicated in Fig. 35, by MoM-VSIE parallel solution.

The computation required usage of a minimum of 10x10 processes. In addition, results were obtained for 12x12 and 16x16 processes. The computational time for all three simulations is presented in the table VIII.

Table VIII. Computational Times for Parallel VSIE Computations of the Luneburg Lens Illuminated by a Corrugate Horn Antenna

Number of processes	Computational time	Number of VIE elements per process	Ideal number of VIE elements per process
N = 10x10	4 h 37 min 54 sec	21-85	30
N = 12x12	5 h 2 min 30 sec	21-82	24
N = 16x16	3 h 48 min 58 sec	11-75	18

Since the simulation of this example requires 49 GB of RAM memory, the sequential computation on one node was impossible to perform. Therefore, to evaluate the codes efficiency, the reduced (not precise) version with $N_u = N_v = N_w = 3$ and $N_{\text{unkn}}^{\text{VSIE}} = 24{,}855$ of the model was run. Table IX presents the computational times for sequential and parallel versions of the code pertaining to the reduced model.

Table IX. Computational Times for Sequential and Parallel VSIE Computations of the Reduced Luneburg Lens Illuminated by a Corrugate Horn Antenna model; Parallel Code Speedup and Efficiency

Number of processes	Computational time	Number of VIE elements per process	Speedup $T_{\text{s}}/T_{\text{p}}$	Parallel code efficiency E_{p}
N = 1	19 h 38 min 41 sec			
N = 2x2	9 h 16 min 8 sec	153-179	2.1194	0.5299
N = 4x4	4 h 28 min 6 sec	78-135	4.3964	0.2748
N = 8x8	2 h 25 min 9 sec	53-99	8.1205	0.1269

Similarly to the example in section 6.3.1 we see a decrease in parallel code efficiency. However, in this case number of VIE elements per process is always greater than optimal (for N=2x2 the expected value being 135, for N=4x4 – 68, and for N=8x8 – 35). The surface horn antenna elements are all calculated by the same process, since the number of unknowns resulting from the SIE part is $N_{\text{unkn}}^{\text{SIE}} = 2{,}229$.

6.4 Summary

In this section of the thesis the MPI based algorithm for parallel MoM-VSIE computations on ISTeC Cray (supercomputer owned by Colorado State University) was implemented. This allowed for the acceleration of computations of larger electromagnetic problems and the overcoming of RAM memory limitations on a regular PC. The accuracy and the efficiency of the parallel code were evaluated for two different examples.

7 CONCLUSIONS AND FUTURE OBJECTIVES

This thesis has proposed a universal double-higher-order method of moments discretization of volume and surface integral equations for analysis of arbitrary electromagnetic structures. In the volume integral equation (VIE), where the scattered field is represented by radiation of volumetric currents and charges, the equation for the total electric field was discretized. As a result, the numerical approximation of the equivalent electric displacement vector was obtained. In the surface integral equation, which is based on the surface equivalence principle, the boundary condition equations for the electric and magnetic fields were numerically solved. In this case, the functions of interest were equivalent electric and magnetic current distributions over interfaces of dielectric profile discontinuity and actual electric currents for PEC structures. The above mentioned equations, being combined in a system for a composite metallic/dielectric structures, were efficiently solved via method of moments and accelerated by a diakoptic approach.

In the first chapter of the thesis a Galerkin-type MoM code, based on both the volume integral equation (VIE) approach for dielectrics and the surface integral equation (SIE) approach for metallic parts, was presented. For the approximation of the geometry, Lagrange-type interpolation generalized hexahedra for volumetric cells and quadrilaterals for surfaces were employed. Within each tessellation element the surface current and equivalent electric displacement vector were expanded in terms of the hierarchical divergence-conforming polynomial vector basis functions. This method, being referred to as a double-higher-order volume/surface integral equation (VSIE) throughout the thesis, has been validated by various numerical and analytical techniques, demonstrating its accuracy and efficiency.

In chapter 2, the VIE part of the VSIE approach was enhanced by the implementation of a continuously inhomogeneous dielectric variation throughout each discretization element. A special Lagrange-type approximation of the dielectric profile was adopted for each curved parametric hexahedron. This implementation allowed for the usage of electrically large elements for modeling of a highly inhomogeneous dielectric object. The developed continuously inhomogeneous VIE analysis, has demonstrated higher efficiency, and a considerable reduction in the number of unknowns in comparison with both piecewise homogeneous VIE and general continuously inhomogeneous techniques.

In chapter 3, the SIE component of the VSIE technique was enhanced so as to allow for the analysis of dielectric structures, which resulted in a generalized VSIE technique. Not only has the newly developed approach demonstrated efficiency in the analysis of high contrast dielectric scatterers possessing inhomogeneity within the volume, but it also provides a base for the implementation of the diakoptic domain-decomposition approach. Said diakoptic technique, presented in chapter 4, is comprised of breaking the original structure into a number of non-overlapping subsystems, analyzing them in a wholly independent manner and combining the obtained results into a solution of the entire system. Since each subsystem is analyzed independently and in a parallel fashion, a substantial acceleration of the computation can be obtained. Moreover, the system division results in a lower requirement for the RAM memory usage. The above mentioned VIE-SIE-diakoptic method has been implemented into the double-higher-order generalized VSIE code, described in chapters 1, 2 and 3. Its performance was evaluated, and discussed in several scattering examples, including both homogeneous and continuously inhomogeneous dielectric structures. Numerical examples have demonstrated that

the developed VIE-SIE-dikoptic method dramatically increases the efficiency of the MoM-VIE approach, while preserving its accuracy.

Further, in chapter 4 the classic divergence-conforming higher order bases were replaced by their equivalent maximally orthogonalized versions. Without any loss in the accuracy of the field approximation within a hexahedral element, new basis functions resulted in a better condition number of the MoM matrix. In chapter 5, a parallel algorithm for the MoM-VSIE computations on ISTeC Cray (the supercomputer owned by Colorado State University) was implemented. This upgrade of the code allowed for the acceleration of the computation of larger electromagnetic problems, while overcoming the RAM memory limitations of a regular PC.

The above developed code presents the opportunity for continued research. Such research might include; modification of the parallelization algorithm to accelerate the computations on ISTeC Cray supercomputer, implementation of the iterative matrix equation solver to fully exploit the efficiency of the maximally orthogonalized basis functions, and exploration of fast algorithms, such as multilevel fast multipole method (MLFMM) for the acceleration of the system matrix computation.

LIST OF JOURNAL PAPERS AND CONFERENCE ASBTRACTS

1. E. Chobanyan, M. M. Ilić, and B. M. Notaroš, "Double-Higher-Order Large-Domain Volume/Surface Integral Equation Method for Analysis of Composite Wire-Plate-Dielectric Antennas and Scatterers", *IEEE Transactions on Antennas and Propagation*, vol. 61, No. 12, pp. 6051-6063, December 2013
2. E. Chobanyan, , D. I. Olćan, M. M. Ilić, and B. M. Notaroš, "Volume Integral Equation Based Diakoptic Domain-Decomposition Method for 3-D Electromagnetic Scattering Analysis", *IEEE Transactions on Antennas and Propagation*, under review
3. E. Chobanyan, M. M. Ilić, and B. M. Notaroš, " Lagrange-type Modeling of Continuous Permittivity Variation in Double-Higher-Order Volume Integral Equation Method", *Radio Science*, Minor Revision, revised paper under review
4. E. Chobanyan, N. J. Šekeljić, A. B. Manić, M. M. Ilić, V. N. Bringi, and B. M. Notaroš, "Efficient and Accurate Computational Electromagnetics Approach to Precipitation Particle Scattering Analysis Based on Higher Order Method of Moments Integral-Equation Modeling", *Journal of Atmospheric and Oceanic Technology*, under review
5. M. Kabir, Md. A. H. Talukder, R. Khazaka, M. A. Dolatsara, E. Chobanyan, A. Smull, S. Roy, and B. M. Notaroš, "Non-Intrusive Pseudo Spectral Approach for Stochastic Macromodeling of EM Systems using Deterministic Full-wave Solvers", *23rd Conference on EPEPS 2014*, 26-29 October, 2014
6. B. M. Notaroš, M. M. Ilić, D. I. Olćan, M. Djordjević, A. B. Manić, and E. Chobanyan, "Hybrid Higher Order Numerical Methods in Electromagnetics", *International Conference on Electromagnetics in Advanced Applications*, 3-9 August, 2014

7. E. Chobanyan, M. M. Ilić, and B. M. Notaroš, "Scattering Analysis Using Generalized Volume-Surface Integral Equation Method of Moments", Submitted for *2014 IEEE Antennas and Propagation Society International Symposium (APSURSI)*, 6-12 July, 2014
8. N. J. Šekeljić, A. B. Manić, E. Chobanyan, M. Thurai, V. N. Bringi, and B. M. Notaroš , "Electromagnetic Scattering by Oscillating Rain Drops of Asymmetric Shapes", Submitted for *2014 IEEE Antennas and Propagation Society International Symposium (APSURSI)*, 6-12 July, 2014
9. A. B. Manić, E. Chobanyan, M. M. Ilić, and B. M. Notaroš, "Parallelization of Double Higher Order FEM and MoM Techniques", Submitted for *2014 IEEE Antennas and Propagation Society International Symposium (APSURSI)*, 6-12 July, 2014
10. E. Chobanyan, N. J. Šekeljić, A. B. Manić, B. M. Notaroš , and M. M. Ilić, "Atmospheric Particle Scattering Computation Using Higher Order MoM-SIE Method", *2013 IEEE Antennas and Propagation Society International Symposium (APSURSI)*, 7-12 July, 2013
11. E. Chobanyan, D. I. Olćan, M. M. Ilić, and B. M. Notaroš, "Combining Diakoptic, VIE-MoM, and SIE-MoM Approaches in Analysis of Dielectric Scatterers", *2013 IEEE Antennas and Propagation Society International Symposium (APSURSI*), 7-12 July, 2013
12. J. Notaros, E. Chobanyan, V. Chandrasekar, and B. M. Notaros, "Accurate and Efficient Full-Wave Electromagnetic Analysis of Scattering from Hailstones," *2013 IEEE Antennas and Propagation Society International Symposium*, July 7-12, 2013
13. E. Chobanyan, M. M. Ilić, and B. M. Notaroš, "Higher Order Volume and Surface Integral Equation Modeling of 3-D Scattering and Radiation Problems", *USNC-URSI National Radio Science Meeting*, January 9-12, 2013

14. E. Chobanyan, J. Notaroš, V. Chandrasekar, and B. M. Notaroš, “Accurate Electromagnetic Modeling of Melting Hail”, *USNC-URSI National Radio Science Meeting*, January 9-12, 2013
15. E. Chobanyan, M. M. Ilić, and B. M. Notaroš, “Efficient higher order volume-integral-equation modeling of dielectric scatterers”, *2012 IEEE Antennas and Propagation Society International Symposium (APSURSI)*, 8-14 July, 2012
16. N. J. Šekeljić, E. Chobanyan, M. M. Ilić, and B. M. Notaroš, “Rules for Adoption of Expansion and Integration Orders in Moment-Method Computation of Electromagnetic Scattering and Radiation”, *USNC-URSI National Radio Science Meeting*, January 4-7, 2012

REFERENCES

[1] R. F. Harrington, *Field Computation by Moment Methods*, IEEE PRESS Series on Electromagnetic Waves, Piscataway, 1993.

[2] B. M. Kolundžija and A. R. Djordjević, *Electromagnetic Modeling of Composite Metallic and Dielectric Structures*, Norwood, MA: Artech House, 2002.

[3] A. F. Peterson, *Mapped Vector Basis Functions for Electromagnetic Integral Equations*, Morgan & Claypool Publishers, 2006.

[4] W. C. Chew, J. M. Jin, E. Michielssen, and J. M. Song, Editors, *Fast and Efficient Algorithms in Computational Electromagnetics*, Norwood, MA: Artech House, 2001.

[5] J. L. Volakis and K. Sertel, *Integral Equation Methods for Electromagnetics*, Raleigh, NC: SciTech Publishing, 2011.

[6] S. M. Rao, T. K. Sarkar, P. Midya, and A. R. Djordjević, "Electromagnetic radiation and scattering from finite conducting and dielectric structures: surface/surface formulation", *IEEE Transactions on Antennas and Propagation*, vol. 39, No. 7, pp. 1034–1037, July 1991.

[7] A. I. Mackenzie, S. M. Rao, and M. E. Baginski, "Method of Moments Solution of Electromagnetic Scattering Problems Involving Arbitrarily-Shaped Conducting/Dielectric Bodies Using Triangular Patches and Pulse Basis Functions," *IEEE Transactions on Antennas and Propagation*, vol. 58, pp. 488-493, December 2009.

[8] D. H. Schaubert, D. R. Wilton, and A. W. Glisson, "A tetrahedral modeling method for electromagnetic scattering by arbitrarily shaped inhomogeneous dielectric bodies," *IEEE Transactions on Antennas and Propagation*, vol. AP-32, pp. 77-85, January 1984.

[9] T. K. Sarkar, E. Arvas and S. Ponnapalli, "Electromagnetic scattering from dielectric bodies," *IEEE Transactions on Antennas and Propagation*, vol. 37, pp. 673-676, May 1989.

[10] B. J. Rubin and S. Daijavad, "Radiation and scattering from structures involving finite-size dielectric regions," *IEEE Transactions on Antennas and Propagation*, vol. 38, pp. 1863-1873, November 1990.

[11] P. Zwamborn and P. M. van den Berg "The three-dimensional weak form of the conjugate gradient FFT method for solving scattering problems," *IEEE Transactions on Microwave Theory and Techniques*, vol. 40, pp.1757-1766, September 1992.

[12] T. K.Sarkar and E. Arvas, "An integral equation approach to the analysis of finite microstrip antennas: volume/surface formulation," *IEEE Transactions on Antennas and Propagation*, vol. 38, pp. 305-312, March 1990.

[13] A. J. Parfitt, D. W. Griffin, and P. H. Cole, "On the modeling of metal strip antennas contiguous with the edge of electrically thick finite size dielectric substrates," *IEEE Transactions on Antennas and Propagation*, vol. 40, pp. 134-140, February 1992.

[14] S. N. Makarov, S. D. Kulkarni, A. G. Marut, and L. C. Kempel "Method of moments solution for a printed patch/slot antenna on a thin finite dielectric substrate using the volume integral equation," *IEEE Transactions on Antennas and Propagation*, vol. 54, pp. 1174-1184, April 2006.

[15] B. M. Notaroš, "Higher order frequency-domain computational electromagnetics," Special Issue on Large and Multiscale Computational Electromagnetics, *IEEE Transactions on Antennas and Propagation*, vol. 56, pp. 2251-2276, August 2008.

[16] G. Kang, J. Song, W. C. Chew, K. C. Donepudi, and J. M. Jin, "A Novel Grid-Robust Higher Order Vector Basis Function for the Method of Moments," *IEEE Transactions on Antennas and Propagation*, vol. 49, pp. 908-915, June 2001.

[17] M. Djordjević and B. M. Notaroš, "Double Higher Order Method of Moments for Surface Integral Equation Modeling of Metallic and Dielectric Antennas and Scatterers," *IEEE Transactions on Antennas and Propagation*, vol. 52, pp. 2118-2129, August 2004.

[18] W. Cai, T. Yu, H. Wang, and Y. Yu, "High-Order Mixed RWG Basis Functions for Electromagnetic Applications," *IEEE Transactions on Microwave Theory and Techniques*, vol. 49, no. 7, pp. 1295-1303, July 2001.

[19] S. Wandzura**, "**Electric-current basis functions for curved surfaces," *Electromagnetics*, vol. 12, no. 1, pp. 77–91, 1992.

[20] B. D. Popović and B. M. Notaroš, "Entire-domain polynomial approximation of volume currents in the analysis of dielectric scatterers," *IEE Proceedings - Microwaves, Antennas and Propagation*, vol. 142, no. 3, pp. 207-212, June 1995.

[21] B. M. Notaroš and B. D. Popović, "General entire-domain method for analysis of dielectric scatterers," *IEE Proceedings - Microwaves, Antennas and Propagation*, vol. 143, no. 6, pp. 498-504, December 1996.

[22] B. M. Notaros and B. D. Popovic, "Optimized entire-domain moment-method analysis of 3D dielectric scatterers," *International Journal of Numerical Modelling: Electronic Networks, Devices and Fields*, vol. 10, pp.177-192, 1997.

[23] B. M. Notaros and B. D. Popovic, "General entire-domain Galerkin method for analysis of wire antennas in the presence of dielectric bodies," *IEE Proceedings - Microwaves, Antennas and Propagation*, vol. 145, No. 1, pp.13-18, February 1998.

[24] P. De Doncker, "A Potential Integral Equations Method for Electromagnetic Scattering by Penetrable Bodies," *IEEE Transactions on Antennas and Propagation*, vol. 49, pp. 1037-1042, July 2001.

[25] K. Sertel and J. L. Volakis, "Method of moments solution of volume integral equations using parametric geometry modeling," *Radio Science*, vol. 37, pp.10-(1-7), January-February 2002.

[26] O. S. Kim, P. Meincke, O. Breinbjerg, and E. Jørgensen, "Method of moments solution of volume integral equations using higher-order hierarchical Legendre basis functions," *Radio Science*, vol. 39, RS5003, pp. 1-7, September 2004.

[27] M. M. Botha, "Solving the volume integral equations of electromagnetic scattering," *Journal of Computational Physics*, vol. 218, pp. 141-158, 2006.

[28] M. M. Botha, "Fully hierarchical divergence-conforming basis functions on tetrahedral cells, with applications," *International Journal for Numerical Methods in Engineering*, vol. 71, pp. 127-148, 2007.

[29] R. D. Graglia and A. F. Peterson, "Hierarchical divergence-conforming Nédélec elements for volumetric cells," *IEEE Transactions on Antennas and Propagation*, vol. 60, no. 11, pp. 5215-5227, November 2012.

[30] B. M. Notaroš and B. D. Popović, "Large-domain integral-equation method for analysis of general 3-D electromagnetic structures," *IEE Proceedings - Microwaves, Antennas and Propagation*, vol. 145, no. 6, pp.491-495, December 1998.

[31] B. M. Notaroš, B. D. Popović, J. P. Weem, R. A. Brown, and Z. Popović, "Efficient large-domain MoM solutions to electrically large practical EM problems," *IEEE Transactions on Microwave Theory and Techniques*, vol. 49, pp.151-159, January 2001.

[32] B. M. Notaroš and B. D. Popović, "Generalized Excitations and Loads for 3D Electromagnetic Analysis with Boundary Elements," invited paper, *International Journal of Engineering Analysis with Boundary Elements, ELSEVIER*, Special Issue on Electromagnetics, vol. 27, pp. 333-343, April 2003.

[33] E. Chobanyan, M.M. Ilic, and B. Notaros,"Double-Higher-Order Large-Domain Volume/Surface Integral Equation Method for Analysis of Composite Wire-Plate-Dielectric Antennas and Scatterers", *IEEE Transactions on Antennas and Propagation*, vol. 61, No. 12, pp. 6051-6063, December 2013.

[34] S. D. Gedney and C. C. Lu, "High-order integral equation solution for scattering by composite materials," *2003 IEEE Antennas and Propagation Society International Symposium Digest*, Columbus, OH, U.S.A., vol. 2, pp.1055-1058, June 22-27, 2003.

[35] E. Jørgensen, J. L. Volakis, P. Meincke, and O. Breinbjerg, "Higher Order Hierarchical Legendre Basis Functions for Electromagnetic Modeling", *IEEE Transactions on Antennas and Propagation,* vol. 52, No. 11, pp. 2985-2995, November 2004.

[36] O. S. Kim, P. Meincke, O. Breinbjerg, and E. Jørgensen, "Solution of volume-surface integral equations using higher-order hierarchical Legendre basis functions," *Radio Science*, vol. 42, RS4023, pp. 1-8, August 2007.

[37] J. L. Volakis, K. Sertel, and B. C. Usner, *Frequency Domain Hybrid Finite Element Methods in Electromagnetics*, Morgan & Claypool Publishers, 2006.

[38] B. C. Usner, J. L. Volakis, K. Sertel, and M. A. Carr, "Generalized Volume-Surface Integral Equation for Modeling Inhomogeneities within High Contrast Composite Structures", *IEEE Transactions on Antennas and Propagation*, vol. 54, No. 1, pp. 68-75, January 2006.

[39] J. Liu, and J. M. Jin, "A novel hybridization of higher order finite element and boundary integral methods for electromagnetic scattering and radiation problems," *IEEE Transactions on Antennas and Propagation*, vol. 49, pp. 1794-1806, December 2001.

[40] M. M. Ilić and B. M. Notaroš, "Higher order hierarchical curved hexahedral vector finite elements for electromagnetic modeling," *IEEE Transactions on Microwave Theory and Techniques*, vol. 51, pp.1026-1033, March 2003.

[41] M. M. Ilic, A. Z. Ilic, and B. M. Notaros, "Continuously Inhomogeneous Higher Order Finite Elements for 3-D Electromagnetic Analysis," *IEEE Transactions on Antennas and Propagations*, vol. 57, No. 9, September 2009, pp. 2798-2803.

[42] R. D. Graglia and A. F. Peterson, "Hierarchical curl-conforming Nédélec elements for quadrilateral and brick Cells," *IEEE Transactions on Antennas and Propagation*, vol. 59, no. 8, pp. 2766-2773, August 2011.

[43] E. M. Klopf, N. J. Sekeljic, M. M. Ilic, and B. M. Notaros, "Optimal modeling parameters for higher order MoM-SIE and FEM-MoM electromagnetic simulations," *IEEE Transactions on Antennas and Propagation*, vol.60, no.6, pp.2790-2801, 2012.

[44] M. Djordjević and B. Notaroš, "Higher-order hierarchical basis functions with improved orthogonality properties for moment-method modeling of metallic and dielectric microwave structures," *Microwave and optical technology letters*, vol. 37, no. 2, pp.83-88, April 2003.

[45] M. M. Kostić and B. M. Kolundžija, "Maximally-orthogonalized higher order bases over generalized wires, quadrilaterals, and hexahedra," accepted for *IEEE Transactions on Antennas and Propagation* (available on IEEE*Xplore*).

[46] M. M. Ilić, M. Djordjević, A. Ž. Ilić, and B. M. Notaroš, "Higher order hybrid FEM-MoM technique for analysis of antennas and scatterers," *IEEE Transactions on Antennas and Propagation*, vol. 57, pp. 1452-1460, May 2009.

[47] R. W. Ziolkowski and M. Tanaka, "FDTD analysis of PBG waveguides, power splitters and switches," *Optical and Quantum Electronics*, vol. 31, pp.843-855, 1999.

[48] A. Bingham, Y. Zhao, and D. Grischkowskya, "THz parallel plate photonic waveguides," *Applied Physics Letters*, vol. 87, 051101, pp.1-3, 2005.

[49] X. Xiaoli, and X. Jiaotong, "FDTD simulation of interstitial antenna for bone cancer microwave hyperthermic therapy", *2004 IEEE Antennas and Propagation Society International Symposium*, June 20-25, Monterey, California, 2004.

[50] G. Kron, *Diakoptics: The Piecewise Solution of Large Scale Systems*, MacDonald, 1963.

[51] C.H. Lai, "Diakoptics, domain decomposition, and parallel computing," *The Computer Journal*, Vol. 37, No. 10, pp. 840-846, 1994.

[52] G. Goubau, N.N. Puri, F.K. Schwering, "Diakoptic theory for multielement antennas," *IEEE Transactions on Antennas and Propagation*, vol. 30, No. 1, pp. 15-26, January 1982.

[53] F.K. Schwering, N.N. Puri, C.M. Butler, “Modified diakoptic theory of antennas,” *IEEE Transactions on Antennas and Propagation*, vol. 34, No. 11, pp. 1273-1281, November 1986.

[54] E. Niver, H.H. Smith, G.M. Whitman, “Frequency characterization of a thin linear antenna using diakoptic antenna theory,” *IEEE Transactions on Antennas and Propagation*, vol. 40, No. 3, pp. 245-250, March 1992.

[55] L.N. Merugu, V.F. Fusco, “Concurrent network diakoptics for electromagnetic field problems,” *IEEE Transactions on Microwave Theory and Techniques*, vol. 41, No. 4, pp. 708-716, April 1993.

[56] S. Ooms, D.D. Zutter, “A new iterative diakoptics-based multilevel moments method for planar circuits,” *IEEE Transactions on Microwave Theory and Techniques*, vol. 46, No. 3, pp. 280-291, March 1998.

[57] D.I. Olcan, I.M. Stevanović, B.M. Kolundžija, J.R. Mosig, A.R. Djordjević, “Diakoptic Surface Integral-Equation Formulation Applied to Large Antenna Arrays,” *Antennas and Propagation Society International Symposium 2008, IEEE*, San Diego, CA, Digital object identifier 978-1-4244-2042-1/08, July 4-12, 2008.

[58] D.I. Olcan, I.M. Stevanović, J.R. Mosig, A.R. Djordjević, "Diakoptic Surface Integral-equation Formulation Applied to Large 2-D Scattering Problems", *Proceedings of EuCAP 2007*, 11-16. Edinburgh, UK, ISBN 9780863418426, November 2007.

[59] D.I. Olcan, “Diakoptic Analysis of Electromagnetic Systems”, *Ph.D. Dissertation*, University of Belgrade, School of Electrical Engineering, Belgrade, Serbia, 2008.

[60] D.I. Olcan, I.M. Stevanović, J.R. Mosig, A.R. Djordjević “A Diakoptic Approach to Analysis of Large 2D Problems” *2006 ACES – The 22nd Annual Review of Progress in Applied Computational Electromagnetics Dig.*, pp. 527-531, Miami, FL, pp. 442-446, March 2006.

[61] D.I. Olcan, I.M. Stevanović, J.R. Mosig, A.R. Djordjević, “Diakoptic Approach to Analysis of Microwave Transmission Lines”, *Proc. of European Microwave Conference*, Manchester UK, pp. 291-294, September 2006. ISBN: 2-9600551-6-0

[62] D.I. Olcan, I.M. Stevanović, B.M. Kolundžija, J.R. Mosig, A.R. Djordjević, "Diakoptic Surface Integral-Equation Formulation Applied to 3-D Scattering Problems," *24th Annual Review of Progress in Applied Computational Electromagnetics (ACES)*, Niagara Falls, Canada, pp. 676-681, March 30 - April 4 2008.

[63] D.I. Olcan, I.M. Stevanović, J.R. Mosig, A.R. Djordjević, "Diakoptic Approach to Analysis of Multiconductor Transmission Lines", *Microwave and Optical Technology Letters*, Vol. 50, No. 4, pp. 931-936, April 2008.

[64] D.I. Olcan, I.M. Stevanović, J.R. Mosig, A.R. Djordjević, "Diakoptic Surface Integral Equation Formulation Applied to 3-D Electrostatic Problems", *Proc. of ACES 2007*, Verona, Italy, pp. 492-498, March 2007.

[65] M. I. Mishchenko, L. D. Travis, and A. A. Lacis, "Scattering,Absorption, and Emission of Light by Small Particles" (Cambridge University Press, 2002)

[66] B. T. Draine and P. J. Flatau, "Discrete-dipole approximation forscattering calculations," *Journal of Optical Society of America (JOSA) A*, vol. 11, pp. 1491−1499, 1994

[67] L. Liao, and R. Meneghini, "Examination of Effective Dielectric Constants of Nonspherical Mixed-Phase Hydrometeors", *Journal of Applied Meteorology and Climatology*, vol. 52, pp. 197-212, January 2013

[68] K. Aydin, S. H. Park, and T. M. Walsh, "Bistatic Dual-Polarization Scattering from Rain and Hail at S- and C-Band Frequencies", *Journal of Atmospheric and Oceanic Technology*, vol. 15, pp. 1110-1121, November 1997

[69] Y. Zhang, A. Huston, M. Mallo, Z. Li, and G. Zhang, "A Scatterometer System for Laboratory Study of Polarimetric Electromagnetic Signatures of Icy Hydrometeors", *IEEE Transaction on Instrumentation and Measurement*, vol. 59, no. 3, pp. 671-681, March 2010

[70] I. Bogaert, and F. P. Andriulli, "Maximally Orthogonal High-Order Basis Functions Have a Well-Conditioned Gram Matrix," *IEEE Transactions on Antennas and Propagation*, vol. 62, No. 8, pp. 4096-4104, August 2014

[71] A. B. Manic, E. Chobanyan, M. M. Ilic, and B. M. Notaros, "Parallelization of Double Higher Order FEM and MoM Techniques", *2014 IEEE Antennas and Propagation Society International Symposium*, July 6-11, Memphis, Tennessee, 2014.

[72] http://www.netlib.orglscalapack/